Impact of Environmental Moisture on the Intensification of Tropical Cyclone in the Bay of Bengal Using WRF-ARW Model

M. Sc. Thesis

BY

SUMON KUMAR DAS

DEPARTMENT OF PHYSICS

KHULNA UNIVERSITY OF ENGINEERING & TECHNOLOGY

KHULNA-9203, BANGLADESH

MARCH 2018

Impact of Environmental Moisture on the Intensification of Tropical Cyclone in the Bay of Bengal Using WRF-ARW Model

M. Sc. Thesis

BY

SUMON KUMAR DAS

ROLL NO: 1655551

SESSION: JULY-2016

A thesis submitted in partial fulfillment of the requirements for the degree of Master of Science in the Department of Physics, Khulna University of Engineering & Technology, Khulna-9203

DEPARTMENT OF PHYSICS

KHULNA UNIVERSITY OF ENGINEERING & TECHNOLOGY

KHULNA-9203, BANGLADESH

March 2018

DECLARATION

This is to certify that the thesis work entitled "***Impact of Environmental Moisture on the Intensification of Tropical Cyclone in the Bay of Bengal using WRF-ARW Model"*** has been carried out by **SUMON KUMAR DAS** in the Department of Physics, Khulna University of Engineering & Technology, Khulna, Bangladesh. The above thesis work or any part of this work has not been submitted anywhere for the award of any degree or diploma.

Signature of Supervisor	Signature of Candidate
(Professor Dr. Md. Mahbub Alam)	(Sumon Kumar Das)

DEDICATED TO
MY BROTHER

Acknowledgements

With my great manner it is a pleasure for me to express my deepest sense of gratitude and indebtedness to my reverend supervisor Dr. Md. Mahbub Alam, Professor, Department of Physics, Khulna University of Engineering & Technology, Khulna, for his kind guidance and supervision and for his constant encouragement throughout the research work. His inspiration and friendly cooperation has accelerated my works.

I am indebted to Professor Dr. Shibendra Shekher Sikder, Head, Department of Physics, Khulna University of Engineering & Technology for his strong support in various ways during the entire period of my study in this department. I express my heartfelt gratitude and thanks to Professor Dr. Md. Abdullah Elias Akhter and Professor Dr. Jolly Sultana Department of Physics, Khulna University of Engineering & Technology. Many thanks for their inspiration and advices from the beginning of my study. I gratefully acknowledge Mr. Md. Kamrul Hasan Reza Associate Professor and Mr. Sujit Kumar Shil, Md. Alamgir Hossain, Mr. Sumon Halder, Assistant Professors and Sumon Deb Nath, Lecturer, Department of Physics, KUET for their cooperation regarding writing the thesis.

My personal thankful greetings are to my good friends and well wishers for their help and cooperation. There are numerous people who could not be mentioned individually but their interesting discussions have prompted much thought on various aspects, I would also like to thank them. I would like to express my heart full thanks to my parents, brothers, sisters and nearest relatives for their inspiration, encouragement and multifaceted supports to carry out this thesis work.

Finally, I want to express my gratitude to almighty of god for his mercy.

Sumon Kumar Das

CONTENTS

List of Figures

List of Table

Nomenclature

AFWA	:	Air force weather agency
AOGCMs	:	Atmospheric-oceanic general circulation models
ARW	:	Advanced Research WRF
BMJ	:	Betts-Miller-Janjic
CAPE	:	Convective available potential energy
CIN	:	Convective inhibition
CNN		cloud condensation nuclei
CP	:	Cumulus Parameterization
EL		equilibrium level
FAA	:	The Federal Aviation Administration
FCL		free convective level
FNL	:	Final Reanalysis
FSL	:	The Forecast Systems Laboratory
Grads	:	Grid Analysis and Display System
IMD	:	India Meteorological Department
ITCZ	:	Inter-tropical convergence zone
KF	:	Kain-Fritch
LFC		level of free convection
MP	:	Microphysics
MRF	:	The Medium Range Forecast
MSLP		Minimum Sea level Pressure
NCAR	:	National Center for Atmospheric Research
NCEP	:	National Center for Environmental Prediction
NOAA		National Oceanic and Atmospheric Administration
NOAA		National oceanic and atmospheric administration
NSSL		National Severe Storms Laboratory
NWP	:	Numerical weather prediction
OLR	:	Outgoing long wave radiation
PBL	:	Planetary Boundary Layer
RH		Relative Humidity
RRTM	:	Rapid radiative transfer model
SAL		Saharan air layer

SCS		severe cyclonic storm
SH		Specific Humidity
SHIPS		Statistical Hurricane Intensity Prediction Scheme
SST	:	Sea surface temperature
TC	:	Tropical Cyclones
UTC	:	Universal Time Co-ordinate
VSCS	:	Very severe cyclonic storm
WD		Wind direction
WDM6		WRF Double-Moment 6-class
WRF		Weather research and forecasting
WS		Wind speed
WSM6	:	WRF Single-moment 6-class
WVMR		Water vapor mixing ratio
YSU	:	Yonsei University Scheme

ABSTRACT

Comprehensive sensitivity analysis on physical parameterization schemes of Advanced Weather Research and Forecasting model (ARW-WRF v3.8.1) has been carried out for the impact of environmental moisture on the intensification of TC Hudhud and TC Mora, which formed in the Bay of Bengal and crossed the eastern coast of India on 12 October 2014 and Bangladesh on 30 May 2017 respectively. The initial and boundary conditions of tropical cyclone (TC) are drawn from the global operational analysis and forecast products of National Center for Environmental Prediction (NCEP-GFS) available for the public at $1°\times1^{o}$ resolution. The model was run by using WSM6-class graupel, Thomson graupel, WDM6-class graupel and NSSL momentum-1 microphysics (MP) schemes coupling with Kain-Fritsch (KF) cumulus parameterization (CP) scheme and four different initial conditions of each cyclone. The model domain consists of 8-24^{o}N and 77-96^{o}E and has 9km horizontal resolution with 19 vertical sigma levels. The model was run for 168, 144, 120 and 96-h using the initial conditions at 0000 UTC of 6, 7, 8 and 9 October 2014 for TC Hudhud and 0000 UTC of 25, 26, 27 and 28May 2017 for TC Mora. We have considered (17-20^{o}N & 85-88^{o}E) and (7-10^{o}N & 92-95^{o}E) positions of TC Hudhud and (20-22^{o}N & 88-92^{o}E) and (8-10^{o}N & 86-90^{o}E) positions of TC Mora as the front and rear positions of TCs respectively to analyze the impact of environmental moisture on the intensification of TC. Track of TCs, Maximum wind speed at 10m level, Minimum Sea level pressure (SLP), Convective available potential energy (CAPE), Convective inhibition (CIN), Relative Humidity (RH), Specific Humidity (SH), Water vapor mixing ratio (WVMR) at 2 meter level, Temperature anomaly, Wind speed (WS) and Wind direction (WD) at different levels have been simulated and analyzed in rear and front positions.

The area average CIN, WVMR, RH, WS, SH, and temperature are found to increase in front and rear position continuously for all MPs before the landfall for all initial conditions. CAPE is found to increase at front position and decrease at rear position with respect to time for all initial conditions. Due to the northeasterly to easterly wind from surface to 200 hPa level during 8-10 October 2014 and southeasterly wind on 11 October at front position the TC Hudhud moved towards eastern coast of India and for southwesterly wind in the upper troposphere during 27-29 May 2017 and westerly wind at all levels on 30 May the TC Mora moved towards Bangladesh coast.

Chapter I
Introduction

1 Introduction

Tropical cyclones (TC) are known to cause enormous damage and destruction in the coastal regions of Bangladesh. Strong winds at the center of the low abundance of moisture and latent heat, which brings the storm to supply the necessary energy. Although TC help to moderate climate by transferring energy from warm equatorial regions to cooler higher latitudes, the combined effects of their extreme wind, precipitation, and storm surge threaten the lives of millions of people who live near the coast. While the forecast of TC tracks and intensification has been significantly improved in the past several decades, the TC intensity forecast is still a great challenge for most operational numerical weather prediction (NWP) centers (DeMaria, 2007). Wu *et al.* (2015) studied on Impact of environmental moisture on TC intensification. This study shows that convection in the environment can have favorable impacts on the storm intensity. Emanuel *et al.* (2003) studied the Environmental Control of TC Intensity. They recommended that all of these factors (potential intensity, storm track, wind shear, upper-ocean thermal structure, bathymetry, and land surface) are shown to influence storm intensity. Environmental moisture has been considered as one of the important factors for TC intensity forecasting. As one of the skillful predictors, the 850 hPa relative humidity (RH) averaged between 200 and 800 km from storm center has been used routinely in the Statistical Hurricane Intensity Prediction Scheme (SHIPS) for hurricane intensity forecasting at the National Hurricane Center (Kaplan et al., 2010).

Hill and Lackmann (2009) studied on Influence of Environmental Humidity on TC Size. They recommended that TC track, intensity, and environmental factors that control TC size. Tao and Zhang (2014) studied on Effect of environmental shear, sea-surface temperature, and ambient moisture on the formation and predictability of TCs: An ensemble-mean perspective. They recommended that, the development of TCs is largely depending on the magnitude of vertical wind shear and diabetic heating, such as the sea-surface temperature and ambient moisture content. Fritz and Wang (2012) made on A Numerical Study of the Impacts of Dry Air on TC Formation: A Development Case and a Non development Case. They recommended that, the upper troposphere is a weak spot of the wave pouch at the early formation stage and that the vertical transport is likely a more direct pathway for dry air to

influence moist convection near the pouch center. Wu and Chen (2012) studied on Sensitivity of TC Precipitation to Atmospheric Moisture Content: Case Study of Bilis. They recommended that the TC precipitation decreased dramatically with the reduction of ambient water vapor content in the atmosphere.

Taraphdar *et al.* (2014) conducted on the role of moist processes in the intrinsic predictability of Indian Ocean cyclones. They recommended that it is demonstrated that moist convection plays a major role in intrinsic error growth that may ultimately limit the intrinsic predictability of the TC. Frank and Ritchie (1998) studied on Effects of Environmental Flow upon TC Structure. They recommended that the pattern of convection in the storm's core is strongly influenced by vertical wind shear and to comparable degree by boundary layer friction.

Emanuel (1985) studied an air-sea interaction theory for TC. He got the hypothesis that TC are developed and maintained against dissipation entirely by self-induced anomalous fluxes of moist enthalpy from the sea surface with virtually no contribution from preexisting convective available potential energy (CAPE). Wang (2008) studied on how outer spiral rain bands affect TC structure and intensity. The numerical results showed that cooling in the outer spiral rain bands maintains both the intensity of a TC and the compactness of its inner core whereas heating in the outer spiral rain bands decreases the intensity but increases the size of a TC. Emanuel *et al.*, (2004) and Kimball, (2006) have suggested that the high environmental moisture may be conducive to TC intensification. Dry air intrusion could lead to a weakening of a TC by inducing asymmetric convective activity and transporting low equivalent potential temperature (θe) air into the sub-cloud layer and storm inflow (e.g., Braun *et al*., 2012; Emanuel, 1989; Ge *et al*., 2013; Kimball, 2006; Tao and Zhang, 2014). However, some studies (e.g., Kimball 2006; Wang, 2009; Ying and Zhang, 2012) showed that substantial moisture may also cause a negative impact on TC strength by facilitating the formation of TC rain bands, which reduces the horizontal pressure gradient of a TC.

In idealized simulations, Hill and Lackmann (2009) varied relative humidity (RH) values in the moist envelope 100 km beyond the TC core and found that larger RH results in the establishment of wider TCs with more prominent outer rain bands. However, in their study, TC intensity was nearly insensitive to environmental RH despite the variation in rain band activity. Composite studies using analyses data sets and satellite observations (Kaplan and DeMaria, 2003; Hendricks *et al*., 2010; Wu *et al*., 2012) have shown that rapid intensification

(RI) of TCs is associated with higher environmental RH in the lower and middle troposphere than non-RI events. Using satellite observations, Shu and Wu (2009) showed that the dry Saharan air layer (SAL) can affect TC intensity in both favorable and unfavorable manners. TCs tend to intensify when dry SAL air is present in the northwest quadrant of TCs. However, TCs tend to weaken when dry air intrudes within 360 km of the TC center in the southwest and southeast quadrants. Substantial azimuthally asymmetry of RH is also found in TCs' environments based on 9 years of satellite observations, with rear quadrants (relative to storm motion) being moister than front quadrants, especially during RI (Wu *et al.,* 2012). Braun *et al*. (2012) showed that dry air located 270 km away from the storm center had little impact on hurricane intensity with no mean flow. Dry air intrusion into the storm vortex, however, suppressed convective activity and increased the asymmetry of convection, leading to a weakening of the storm. While a dry air envelope had no significant impact on hurricane intensity, the storm size was reduced. Vertical shear can significantly enhance the suppression effect of dry air intrusion (Tang and Emanuel, 2012; Ge *et al.*, 2013; Tao and Zhang, 2014). By modifying the diabetic heating rate due to cloud microphysical process, Wang (2009) demonstrated that diabetic cooling in the outer spiral rain bands helped the TC remain intense and compact. Increased latent heat release in the outer spiral rain bands decreased the intensity but increased the TC size. In a sensitivity study of Typhoon Talim (2005), Ying and Zhang (2012) showed that enhanced moisture promoted convection in outer rain bands and resulted in the weakening of the storm while dry air in habited outer rain bands and contributed to a stronger storm with smaller size. The storm was more sensitive to the moisture perturbation residing to the north than to the south due to its shorter travel time into the storm vortex.

Bianco *et al.,* (2011) considered the heat, moisture, and momentum flux contributions from spray within a one-dimensional surface layer model and find enhancements of sensible and latent heat flux at sufficiently high wind speeds. Sobel and Camargo (2005) have found that TCs spread out a wide area at low outgoing long wave radiation (OLR). Pattanaik and Rama Rao (2009) simulated the characteristic of movement on a very severe cyclone Nargis using WRF-ARW model in the Bay of Bengal and have found that the TC move towards the minimum OLR. Evans *et al.*,(2012)build up a relation between sea surface temperature (SST) and OLR by using atmospheric-oceanic general circulation models (AOGCMs). They found that the OLR generally increases with increases SST until a threshold ocean temperature. Choi and Byun (2010) have shown that higher TC passage frequency during the high-Arctic

Oscillation (AO) years have a negative OLR. Choi and Moon (2012) have also observed that the TCs occurred in the western region of negative OLR. The OLR field shows a significant negative anomaly in the region over the North Indian Ocean. Camargo *et al.,* (2007) have found that OLR minima at first TC positions and maxima at the position of maximum intensity. Xu and Wang (2010) conducted many experiments and have shown that the removal of surface entropy fluxes outside the eye wall reduces the CAPE and suppresses the activity of spiral rain bands. Bogner *et al.,* (1999) showed that CAPE value maximum at larger radii and lower near the eye wall. Smith and Montgomery (2012) have found that CAPE values are generally largest on the first day of observation and its decreased day by day. They also established an idea that CAPE varies inversely with CIN.

Colon-Pagan (2009) found that near the center of TC CAPE value is very low in their ARW model simulation. They worked on the Hurricane Jeanne in combination with four microphysics schemes and found that CAPE is associated with conditionally unstable airstreams and around the prominent feeder bands CAPE is very low. Molinari *et al.,*(2009)using the more than 2000 dropsonde sounding by the NOAA Gulfstream-IV aircraft for observing the changing pattern of CAPE and found that the mean CAPE raises from center to outer region. The numerical experiment perform by the Fang *et al.,*(2009) using the non-hydrostatic, axi-symmetric TC model and suggest that cyclone has increasing trend at first and decreasing trend when it is strengthen. Nolan *et al.,*(2007)study on TC using WRF v2.1.2 combination of WSM6 class microphysics and Yonsei University (YSU) scheme which detected temperature effect on CAPE correspond with Coriolis force and showed that CAPE were proportional relation with SST.

The impact of cloud microphysical processes on hurricane intensity and track were investigated by many authors. Pattnaik and Krishnamurti (2007) have shown that the microphysical parameters have minimal impact on the hurricane track forecast and also suggested that robust impact on the structural characteristics of hurricane eye-wall and its intensity. Willoghby *et al.,* (1984) studied the impact of cloud microphysics on TC structure and intensity using 2D axi-symmetric non-hydrostatic model. Their results show that the ice-phase microphysical scheme can produce a lower mean sea level pressure (MSLP) than the case without the ice-phase. Wang (2002) demonstrated that the intensification rate and intensity are not sensitive to the cloud microphysical parameterizations. However, he noted that cloud structures and aerial coverage of and the peak precipitation in the TC were quite sensitive to details of the cloud microphysical parameterization in their TCM3 model.

Davis and Bosart (2002) considered the effects of cumulus parameterization on tropical storm track. They found that the Betts-Miller-Janjic (BMJ) and Grill schemes produced more westward track than Kain-Fritsch (KF) scheme. The KF scheme tended to intensify the storm too rapidly but produced the best track compared with observations. Tao *et al.*, (2003) showed that the dominant microphysical processes were quite different between the convective and stratiform regions and between the mature and decaying stages.

In this research we have been conducted many experiments by using four different (WSM6, Thompson, WDM6 and NSSL 1-Mom) microphysics (MP) schemes in combination with KF cumulus parameterization (CP) schemes considering different initial conditions of TC Mora (2017) and TC Hudhud (2014) those formed in the Bay of Bengal and crossed Bangladesh and the eastern coast of India. We have studied the effect of Convective available potential energy (CAPE), Convective inhibition (CIN), Water vapor mixing ratio at 2 M (WVMR), Relative humidity (RH), Specific Humidity (SH), Minimum Sea level pressure (MSLP), Temperature anomaly, Wind direction (WD), Wind speed (WS), Wind Speed at 10 m level for the intensification on envirmental moisture of TC. The aim of this research is to investigate the effects of above mentioned parameters for intensification on environmental moisture of TCs in the Bay of Bengal. It is also our interest to identify the suitable MP scheme to address the above mentioned parameters.

In the present study, the Weather Research and Forecast (WRF-ARWv3.8.1) model will be used to simulate the impact of environmental moisture on tropical cyclone intensification over the Bay of Bengal. The objective of this research is to investigate the amount of moisture generated and propagated through the model domain or the area of TCs. Is this moisture is related to the intensification of tropical cyclones? Attempt will be made to identify the effect of environmental moisture on tropical cyclones movements and intensification in the Bay of Bengal. The study will enhance the existing knowledge. The life and properties can be saved by accurate forecasting of TC.

Chapter II
Literature Review

2.1 Tropical Cyclone (TC)

Tropical Cyclone is defined as a non-frontal low pressure system of synoptic scale that is developing over warm waters having organized convection and a maximum wind speed of 34 knots (gale force) or greater extending more than half-way around near the centre and persisting for at least six hours. The gale force winds can extend hundreds of kilometers from the cyclone centre. If the sustained winds around the centre reach 118 km/h (gusts in excess 165 km/h), then the system is called a severe TC. These are referred to as hurricanes in Atlantic Ocean and typhoons in Pacific Ocean. The circular eye or centre of a TC is an area characterized by light winds and often by clear skies. Eye diameters are typically 40 km but can range from under 10 km to over 100 km. The eye is surrounded by a dense ring of cloud about 16 km high known as the eye wall which marks the belt of strongest winds and heaviest rainfall. In addition to strong winds and rain, TCs are capable of generating high waves, damaging storm surge, and tornadoes. They typically weaken rapidly over land where they are cut off from their primary energy source. For this reason, coastal regions are particularly vulnerable to damage from a TC as compared to inland regions. Heavy rains, however, can cause significant flooding inland, and storm surges can produce extensive coastal flooding up to 40 kilometers from the coastline. Though their effects on human populations are often devastating, TCs can relieve drought conditions. They also carry heat energy away from the tropics and transport it toward temperate latitudes, which may play an important role in modulating regional and global climate.

2.2 Classification of Tropical Cyclone

Cyclonic disturbances in the North Indian Ocean are classified according to their intensity. The following nomenclature is in use:

i.	Low:	Wind Speed < 31 km/hr.
ii.	Well marked low:	Wind Speed equals to 31 km/hr.
iii.	Depression:	Wind Speed ranges from 32 - 48 km/hr.
iv.	Deep Depression:	Wind Speed ranges from 49 - 62 km/hr.
v.	Cyclonic Storm:	Wind Speed ranges from 63 - 88 km/hr.
vi.	Severe Cyclonic Storm:	Wind Speed ranges from 89 - 117 km/hr.

vii. SCS with a core of hurricane intensity: 118-220 km/hr.

viii. Super Cyclone super cyclone > 220 km/hr.

2.3 Life Cycle of Tropical Cyclones

The life span of TCs with full cyclonic intensity averages at about 6 days from the time they form until the time they enter land or recurve into the Temperate Zone. Some storms last only a few hours; a few as long as two weeks. The evolution of the average storm from birth to death has been divided into four stages (Tarakanov, 1982).

i. **Formative Stage:** Tropical storms form only in near pre-existing weather systems. Deepening can be a slow process, requiring days for the organization of a large area with diffuse winds. It can also produce a well-formed eye within 12 hours. Wind speed usually remains below hurricane force in the formative stage. Unusual fall of pressure over 24 hours by 2 - 3 hPa or more takes place in the center of the vortices concentration.

ii. **Immature Stage:** A large number of formative cyclones die within 24 hours. Others travel long distances as shallow depressions. Wind of cyclonic force forms a tight band around the center. The cloud and rain pattern changes from disorganized squalls to narrow organized bands, spiraling inward. Only a small area is as yet involved, though there may be a large outer envelope. The eye is usually visible but ragged and irregular in shape.

iii. **Mature Stage:** The force of cyclonic winds may blow within a 30 - 50 km radius during immature stage. This radius can increase to over 300 km in mature storms. On an average the mature stage occupies the longest part of the cycle and most often lasts several days. The eye is prominent and circular and the cloud pattern is almost circular and smooth. The surface pressure at the center is no longer falling and the maximum wind speeds no longer increasing. At this stage, heating from convective clouds furnishes the largest amount of energy for cyclone maintenance. Pressure gradient is largest at the surface. Wind speed range is between 128 - 322 km/hr.

iv. **Terminal Stage:** Nearly, all cyclones weaken substantially upon entering land, because they lose the energy source furnished by the underlying ocean surface. The decay is especially rapid where the land is mountainous. Movement of a cyclone over land cuts off the surface energy source and increased the surface friction, especially when the land is mountainous. Some cyclones die out over sea and this event can be

related to their moving over a cold ocean current or being invaded by a surface cold air mass behind a cold front or by a cold center at high levels moving over their top.

2.4 Environmental moisture on the intensification of TC

2.4.1 Front

When air masses having very different temperature and humidity properties come together, they do not mix readily but maintain a boundary surface of discontinuity for some time, the warmer lighter air being forced aloft over the colder air mass that stays below. When a TC is moving from its origin to land, then the forepart is considered as front. To examine the impact of the environmental moisture on the intensification of TC we have considered a region inside the model domain that's front position of each cyclone and it situated along the track of cyclone. The regions are (17-20^{o}N & 85-88^{o}E) for TC Hudhud and (17-20^{o}N & 85-88^{o}E) for TC Mora.

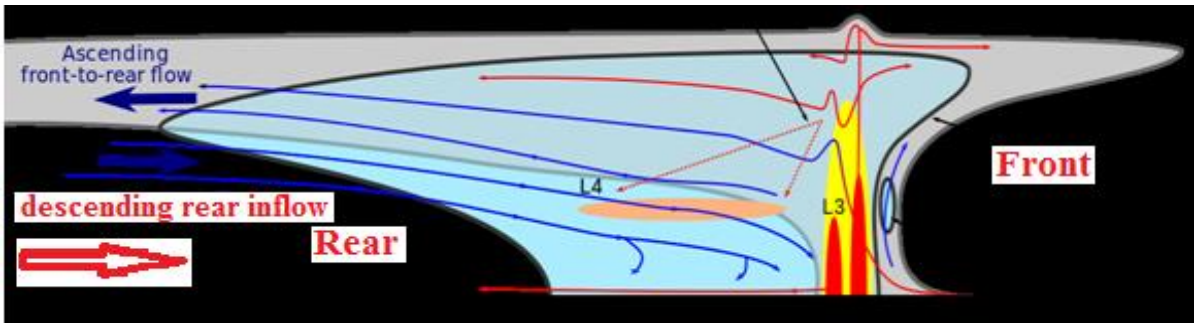

Figure 2.1: Conceptual air flow in a squall line with the Rear-inflow and front to rear flow of a TC.

2.4.2 Rear

Cyclones are born in the hot, humid summer environment. As the sun warms the oceans, evaporation and conduction transfer heat to the atmosphere so rapidly that air and water temperatures differ by a very small amount. The water vapor generated by such evaporation is the fuel that drives a TC, because as the vapor condenses into clouds and precipitation it pumps enormous amounts of heat into the cyclone. Another ingredient that must be present for formation is the Coriolis force or spin. The Coriolis Effect is the force caused by the earth's rotation that deflects a moving body to the right in the Northern Hemisphere and to the left in the Southern Hemisphere. From its origins place it moves toward land.

2.4.3 Relative Humidity (RH)

Relative Humidity is the most commonly used measurements of moisture content in the air. The RH is the amount of water vapor (moisture) in the air compared to the maximum amount that the air could hold at a given temperature. The relative humidity is:

$$f = \frac{\omega}{\omega_s} \times 100 = \frac{\rho_w}{\rho_{ws}} \times 100 = \frac{q}{q_s} \times 100 = \frac{e}{e_s} \times 100$$

If the amount of water vapor in the air increases, the RH increases, and if the amount of water vapor in the air decreases, the RH decreases. If the RH is 100%, the air is saturated. If the RH is 50%, the air contains half the water vapor required for it to be saturated. However, RH is dependent on air temperature, too. If the water vapor content remains the same and the temperature drops, the RH increases. If the water vapor content remains the same and the temperature rises, the RH decreases. This is because colder air doesn't require as much moisture to become saturated as warmer air. Warm air can hold more water vapor than cool air, so a particular amount of water vapor will yield a lower RH in warm air than it does in cool air.

If you watch the weather in the summer, you'll notice that the RH is actually higher in the morning than in the afternoon. This is because the cooler morning air is closer to saturation than the hot afternoon air, even with the same amount of water vapor. Surprisingly, there is no significant difference in daily average RH between summer and winter. Since warm air is less dense than cold air, there is more room for water vapor in warm summer air as compared with cold winter air**.** At a given vapor pressure (or mixing ratio), RH with respect to ice is higher than that with respect to water. Water is known by different names in different states. If the maximum amount of water vapor has been reached and more water is introduced into the air, an equal amount of water must transform back to liquid or solid form through condensation. At this point, the air is said to be saturated with water, and the RH is 100%. On the other end of the scale, when there is no water vapor in the air, the RH is 0% whatever the temperature. In other words, RH always lies between 0 and 100%. As mentioned, the ability of air to hold water vapor is strongly dependent on temperature. This means that RH is also strongly temperature dependent.

2.4.4 Specific Humidity (SH)

The specific humidity is defined as the weight of water vapor contained in a unit weight of air (dry air plus water vapor), expressed in grams per gram or grams per kilogram or kilograms per kilogram. It is also the ratio of the pressure of water vapor to the rest of the pressure of the air besides the water vapor. Sometimes it is referred to as the humidity ratio. The best way to think of SH is just the partial pressure of water vapor only in the air to the total combined pressure of all the other fluid particles in the air. Therefore, it's the ratio of water vapor to everything else combined in the air.

The factors which affect SH are the partial pressure of water vapor, P_W, and the total pressure of the water vapor/air mixture, P. The greater the partial pressure of water vapor, the greater the SH. The lesser the partial pressure, the smaller the humidity. Note that the partial pressure of water vapor cannot be a greater value than the total pressure of the water vapor/air mixture. Being that the total pressure comprises both partial water vapor and the pressure of all other particles in the air, the total pressure must always be greater than the partial pressure.

Partial and total pressures, P_W and P, are computed in hPa. However, if we want to change these and use different units, the answer will still work out as the same, as long as you use equal unit measurement for both pressures. Specific humidity is defined as

$$q = 0.622\frac{e}{p} \text{ gm per gm (Approximately)}$$

Where,

$$e = 6.11 * \exp\left((17.2694 * (T - 273.16))/(T - 35.86)\right)$$

So,

$$q = 0.622\frac{6.11 * \exp\left((17.2694 * (T - 273.16))/(T - 35.86)\right)}{P}$$

2.4.5 Temperature Anomaly

The temperature anomaly means a departure from a reference value or long-term average. A positive anomaly indicates that the observed temperature was warmer than the reference value, while a negative anomaly indicates that the observed temperature was cooler than the reference value. When researching global climate changes and temperature data, temperature anomaly is observed in this case. That is the difference between the long-term average

temperature (sometimes called a reference value) and the temperature that is actually occurring. In other words, the long-term average temperature is one that would be expected; the anomaly is the difference between what you would expect and what is happening.

2.4.6 Sea Level Pressure (SLP)

The SLP is the atmospheric pressure at sea level at a given location. When observed at a reporting station that is not at sea level (nearly all station), it is a correction of the station pressure to sea level. This correction takes into account the standard variation of pressure with height on the pressure. The temperature used in the sea level correction is a twelve hour mean, eliminating diurnal effect. The mean sea level pressure (MSLP) is the atmospheric pressure at sea level. This is the atmospheric pressure normally given in weather reports on radio, television, and newspapers or on the Internet. When barometers in the home are set to match the local weather reports, they measure pressure adjusted to sea level, not the actual local atmospheric pressure. The altimeter setting in aviation is an atmospheric pressure adjustment. Average SLP is 1013.25 hPa (101.325 kPa; 29.921 in Hg; 760.00 mmHg). In aviation weather reports (METAR), QNH is transmitted around the world in millibars or hectopascals (1 hectopascal = 1 millibar), except in the United States (US), Canada, and Colombia where it is reported in inches (to two decimal places) of mercury. US and Canada also report SLP, which is adjusted to sea level by a different method, in the remarks section, not in the internationally transmitted part of the code, in hectorpascals or millibars. However, in Canada's public weather reports, sea level pressure is instead reported in kilopascals. In the US weather code remarks, three digits are all that are transmitted; decimal points and the one or two most significant digits are omitted: 1013.2 hPa (101.32 kPa) is transmitted as 132; 1000.0 hPa (100.00 kPa) is transmitted as 000; 998.7 hPa is transmitted as 987; etc. The highest SLP on Earth occurs in Siberia, where the Siberian High often attains a SLP above 1050 hPa (105 kPa; 31 in Hg), with record highs close to 1085 hPa (108.5 kPa; 32.0 in Hg). The lowest measurable SLP is found at the centers of TCs and tornadoes, with a record low of 870 hPa.

2.4.7 Water Vapor Mixing Ratio (WVMR)

Mixing ratio $(\omega)$is the amount of water vapor that is in the air. ω is the grams of vapor per kg of dry air. ω is an absolute measure of the amount of water vapor in the air. The mixing ratio is defined as the weight of water vapor contained in mixture with a unit weight of dry air,

expressed in grams per gram or gram per kilogram. It differs from specific humidity only in that it is related to dry air instead of to the total of dry air plus water vapor.

$$\omega = \frac{\rho_w}{\rho_d} = \frac{m_w}{m_d}$$

Since there are so few molecules of water vapor in a volume of air, as compared to N_2 and O_2, the value of the mixing ratio is similar to the specific humidity. Changing the temperature of the air parcel does not affect the parcels mixing ratio.

2.4.8 Wind Speed

Wind speed, or wind flow velocity is a fundamental atmospheric quantity. Wind speed is caused by air moving from high pressure to low pressure, usually due to changes in temperature. Wind speed affects weather forecasting, aircraft and maritime operations, construction projects, growth and metabolism rate of many plant species, and countless other implications. Wind speed is now commonly measured with an anemometer but can also be classified using the older Beaufort scale which is based on people's observation of specifically defined wind effects.

In meteorology, winds are often referred to according to their strength, and the direction from which the wind is blowing. Short bursts of high speed wind are termed gusts. Strong winds of intermediate duration (around one minute) are termed squalls. Long-duration winds have various names associated with their average strength, such as breeze, gale, storm, and hurricane. Wind occurs on a range of scales, from thunderstorm flows lasting tens of minutes, to local breezes generated by heating of land surfaces and lasting a few hours, to global winds resulting from the difference in absorption of solar energy between the climate zones on Earth. The two main causes of large-scale atmospheric circulation are the differential heating between the equator and the poles, and the rotation of the planet (Coriolis Effect). Within the tropics, thermal low circulations over terrain and high plateaus can drive monsoon circulations. In coastal areas the sea breeze/land breeze cycle can define local winds; in areas that have variable terrain, mountain and valley breezes can dominate local winds.

In most of the world, the standard height above the surrounding vegetation for measuring open wind speed is ten meters (33 feet); in the United States, it is measured 20 feet above the surrounding vegetation (20-ft wind speed). Multiply 20-foot wind speed by 1.15 to estimate

10 m wind speed, alternately, divide 10-meter wind speed by 1.15 to estimate 20-foot wind speed (Turner and Lawson 1978).

2.4.9 Convective Available Potential Energy (CAPE)

Convective available potential energy (CAPE), sometimes, simply, available potential energy (APE) is the amount of energy of a parcel of air would have if lifted a certain distance vertically through the atmosphere. CAPE is effectively the positive buoyancy of an air parcel and is an indicator of atmospheric instability, which makes it very valuable in predicting severe weather. It is a form of fluid instability found in thermally stratified atmospheres in which a colder fluid overlies a warmer one. When an air mass is unstable, the element of the air mass that is displaced upwards is accelerated by the pressure difference between the displaced air and the ambient air at the higher altitude to which it was displaced. This usually creates vertically developed clouds from convection, due to the rising motion, which can eventually lead to thunderstorms. It could also be created in other phenomenon, such as a cold front. Even if the air is cooler on the surface, there is still warmer air in the mid-levels that can rise into the upper-levels. However, if there is not enough water vapor present, there is no ability for condensation, thus storms, clouds, and rain will not form.

CAPE exists within the conditionally unstable layer of the troposphere, the free convective level (FCL), where an ascending air parcel is warmer than the ambient air. CAPE is measured in joules per kilogram of air (J/kg). Any value greater than 0 J/kg indicates instability and the possibility of thunderstorms. CAPE is calculated by integrating vertically the local buoyancy of a parcel from the level of free convection (LFC) to the equilibrium level (EL):

$$CAPE = \int_{EL}^{LFC} \left(\frac{T_v - T_{ve}}{T_{ve}} \right) g dz \qquad (1)$$

Where T_v the virtual temperature of the parcel is T_{ve} is the virtual temperature of the environment and g is the gravitational acceleration. On a sounding diagram, CAPE is the positive area above the LFC, the area between the parcel's virtual temperature line and the environmental virtual temperature line where the ascending parcel is warmer than the environment. When a parcel is unstable, it will continue to move vertically, in either direction dependent on whether it receives upward or downward forcing, until it reaches a stable layer. There are multiple types of CAPE, downdraft CAPE (DCAPE), estimates the potential strength of rain and evaporative cooled downdrafts. Other examples are surface based CAPE

(SBCAPE), mixed layer or mean layer CAPE (MLCAPE), most unstable or maximum usable CAPE (MUCAPE), and normalized CAPE (NCAPE).

On the other hand, if adiabatic decrease or increase in density is greater than in the ambient fluid, the upwards or downwards displacement will be met with an additional force in the same direction exerted by the ambient fluid. In these circumstances, small deviations from the initial state will become amplified. This condition is referred to as convective instability. Convective instability is also termed static instability, because the instability does not depend on the existing motion of the air; this contrasts with dynamic instability where instability is dependent on the motion of air and its associated effects such as dynamic lifting.

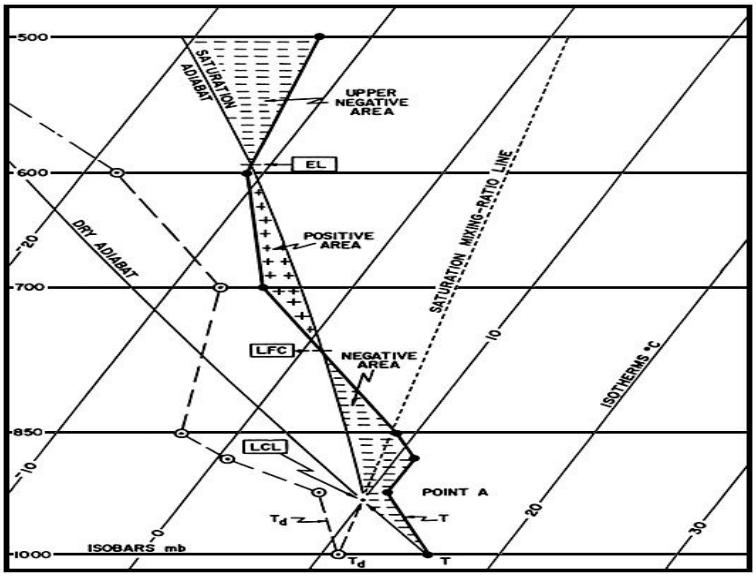

Figure 2.2: A Skew-T diagram with important features labeled

The amount of and shape of the positive area modulates the speed of updrafts, extreme CAPE can result in explosive thunderstorm development; such rapid development usually occurs when CAPE stored by a capping inversion is released when the "lid" is broken by heating or mechanical lift. The amount of CAPE also modulates how low-level vortices is entrained and then stretched in the updraft, with importance to storm do genesis. The most important CAPE for tornadoes is within the lowest 1 to 3 km, whilst deep layer CAPE and the width of CAPE at mid-levels are important for super cells. Tornado outbreaks tend to occur within high CAPE environments. Large CAPE is required for the production of very large hail, owing to updraft strength, although a rotating updraft may be stronger with less CAPE. Large CAPE also promotes lightning activity.

CAPE for different stability regimes are given as follows :(Molinari *et al.* 2009*)*

CAPE < 1000 J/Kg	:	Instability is weak
CAPE > 1000 < 2500 J/Kg	:	Moderately unstable
CAPE > 2500 J/Kg	:	Extremely unstable

2.4.10 Convective Inhibition (CIN)

Convective Inhibition (CIN) is a numerical measure in meteorology that indicates the amount of energy that will prevent an air parcel from rising from the surface to the level of free convection. It is the amount of energy required to overcome the negatively buoyant energy. For the most case, when CIN exists, it covers a layer from the ground to the LFC. The negatively buoyant energy exerted on an air parcel is a result of the air parcel being cooler (denser) than the air which surrounds it, which causes the air parcel to accelerate downward. The layer of air dominated by CIN is warmer and more stable than the layers above or below it.

The situation in which convective inhibition is measured is when layers of warmer air are above a particular region of air. The effect of having warm air above a cooler air parcel is to prevent the cooler air parcel from rising into the atmosphere. This creates a stable region of air. Convective inhibition indicates the amount of energy that will be required to force the cooler packet of air to rise. This energy comes from fronts, heating, moistening, or mesoscale convergence boundaries such as outflow and sea breeze boundaries. Typically, an area with a high convection inhibition number is considered stable and has very little likelihood of developing a thunderstorm. Conceptually, it is the opposite of CAPE. CIN hinders updrafts necessary to produce convective weather, such as thunderstorms. Although, when large amounts of CIN are reduced by heating and moistening during a convective storm, the storm will be more severe than in the case when no CIN was present. (*Colby and Frank 1984)*

CIN is calculated by measurements recorded electronically by a rawinsonde which measure weather parameters, such as air temperature and pressure. A single value for CIN is calculated from balloon ascent by using the equation:

$$CIN = \int_{Z_{bottom}}^{Z_{top}} \left(\frac{T_{v,parcel} - T_{v,env}}{T_{v,env}} \right) g dz \qquad (2)$$

The Z_{bottom} and Z_{top} limits of integration in the equation represent the bottom and top

altitudes of a single CIN layer, is the virtual temperature of the specific parcel and is the virtual temperature of the environment. In many cases, the Z_{bottom} value is the ground and the Z_{top} value is the LFC. CIN is expressed as a negative energy value. CIN values greater than 200 J/kg are sufficient enough to prevent convection the atmosphere. In fact, CIN is sometimes referred to as negative buoyant energy. It is a good indicator of general stability, and convection tends to be less vigorous with higher values.

CIN	< 100	Potential Instability.
CIN	100 to 200	Marginally stable.
CIN	200 to 300	Moderately stable.
CIN	>400	Very stable.

2.5 Weather Research & Forecasting (WRF) Model

The Weather Research and Forecasting (WRF) Model is a next-generation mesoscale numerical weather prediction (NWP) system designed to serve both atmospheric research and operational forecasting needs. It features two dynamical cores, a data assimilation system, and a software architecture facilitating parallel computation and system extensibility. The model serves a wide range of meteorological applications across scales from tens of meters to thousands of kilometers. The effort to develop WRF began in the latter part of the 1990's and was a collaborative partnership principally among the National Center for Atmospheric Research (NCAR), the National Oceanic and Atmospheric Administration (NOAA) represented by the National Centers for Environmental Prediction (NCEP) and the Forecast Systems Laboratory (FSL) the Air Force Weather Agency (AFWA), the Naval Research Laboratory, the University of Oklahoma, and the Federal Aviation Administration (FAA).

The WRF model is an atmospheric simulation system which is designed for both operational and research use. WRF is currently in operational use at the NOAA national weather service as well as at the air force weather agency and meteorological services worldwide. Getting weather predictions in time using latest advances in atmospheric sciences is a challenge even on the fastest super computers. Timely weather predictions are particularly useful for severe weather events when lives and property are at risk. Microphysics is a crucial but computationally intensive part of WRF. WRF offers two dynamical solvers for its computation of the atmospheric governing equations, and the variants of the model are known as WRF-ARW and WRF-NMM. The Advanced Research WRF (ARW) is supported to the community by the NCAR Mesoscale and Microscale Meteorology Division. The WRF-NMM solver variant was based on the Eta Model, and later Non hydrostatic Mesoscale

Model, developed at NCEP. The WRF-NMM is supported to the community by the Developmental Test bed Center.

2.5.1 Microphysics Schemes in WRF-ARW Model

Microphysics includes explicitly resolved water vapor, cloud and precipitation processes. The model is general enough to accommodate any number of mass mixing-ratio variables, and other quantities such as number concentrations. Four-dimensional arrays with three spatial indices and one species index are used to carry such scalars. Memory, i.e., the size of the fourth dimension in these arrays, is allocated depending on the needs of the scheme chosen, and advection of the species also applies to all those required by the microphysics option. In the current version of the ARW, microphysics is carried out at the end of the time-step as an adjustment process, and so does not provide tendencies. The rationale for this is that condensation adjustment should be at the end of the time-step to guarantee that the final saturation balance is accurate for the updated temperature and moisture. However, it is also important to have the latent heating forcing for potential temperature during the dynamical sub-steps and this is done by saving the microphysical heating as an approximation for the next time-step as described.

2.5.1.1 WRF Single-Moment 6-class Scheme (WSM6)

The WRF-single-moment-6-class (WSM6) microphysics scheme has been one of the options of microphysical process in the WRF model. This scheme predicts the mixing ratios for water vapor, cloud water, cloud ice, snow, rain, and graupel. We attempt to improve such existing deficiencies in the WSM6 scheme by incorporating the prediction of number concentrations for warm rain species. A new method for representing mixed-phase particle fall speeds for the snow and graupel by assigning a single fall speed to both that is weighted by the mixing ratios, and applying that fall speed to both sedimentation and accumulation processes is introduced of the three WSM schemes, the WSM6 scheme is the most suitable for cloud-resolving grids, considering the efficiency and theoretical backgrounds (Hong *et al.*, 2006). The WSM6 scheme has been developed by adding additional process related to graupel to the WSM6 scheme (Hong and Lim, 2006).

2.5.1.2 Thompson *et al.,* Scheme

A bulk microphysical parameterization (BMP) developed for use with WRF or other mesoscale models. The snow size distribution depends on both ice water content and

temperature and is represented as a sum of exponential and gamma distributions. Furthermore, snow assumes a non-spherical shape with a bulk density that varies inversely with diameter as found in observations. A new scheme with ice, snow and graupel processes suitable for high-resolution simulations. This adds rain number concentration and updates the scheme from the one in Version 3.0 New Thompson et al. scheme in V3.1. Replacement of Thompson *et al.,* (2007) scheme that was option 8 in V3.0 6-class microphysics with graupel, ice and rain number concentrations also predicted.

2.5.1.3 WRF Double-Moment 6-class (WDM6) Scheme

The WRF double-moment 6-class (WDM6) microphysics scheme implements a double-moment bulk micro physical parameterization of clouds and precipitation and is applicable in mesoscale and general circulation models. The WDM6 scheme enables the investigation of the aerosol effects on cloud properties and precipitation processes with the prognostic variables of cloud condensation nuclei (CCN), cloud water and rain number concentrations. WDM6 extends the WRF single-moment 6-class microphysics scheme (WSM6) by incorporating the number concentrations for cloud and rainwater along with a prognostic variable of CCN number concentration. Moreover, it predicts the mixing ratios of six water species (water vapor, cloud droplets, cloud ice, snow, rain, and graupel), similar to WSM6. Prognostic water substance variables include water vapor, clouds, rain, ice, snow, and graupel for both the WDM6 and WSM6 schemes. Additionally, the prognostic number concentrations of cloud and rain waters, together with the CCN, are considered in the WDM6 scheme. The number concentrations of ice species such as graupel, snow, and ice are diagnosed following the ice-phase microphysics of Hong *et al.* (2004).

2.5.1.4 NSSL-1 Microphysics Scheme

The NSSL-1 scheme is a moment one developed at the National Severe Storms Laboratory which is very similar to Gilmore *et al.* (2004). It predicts the mass mixing ratio and number concentration for six hydrometeor species: cloud droplets, rain drops, ice crystals, snow, graupel and hail *(*Mansell *et al.,* 2010*).* A unique feature is the additional prediction of average graupel particle density, which allows graupel to span the range from frozen drops to low-density graupel. Hail is produced only by wet growth of graupel to try to represent true hail rather than merely high-density ice. An option allows prediction of cloud condensation nuclei (CCN) concentration (intended for idealized simulations). The scheme also features adaptive sedimentation to allow some size sorting but prevent spurious large particles (and

radar reflectivity values) that can arise from one-moment microphysics, particularly for the larger precipitation categories (graupel and hail).These have been added to WRF recently (V3.4+) and it has very little experience with us and additional name list options available for it. Size distribution shape parameters and a number of other options can be set in the code.

2.5.2 Cumulus Parameterization Schemes

These schemes are responsible for the sub-grid-scale effects of convective and/or shallow clouds. The schemes are intended to represent vertical fluxes due to unresolved updrafts and downdrafts and compensating motion outside the clouds. They operate only on individual columns where the scheme is triggered and provide vertical heating and moistening profiles. Some schemes provide cloud and precipitation field tendencies in the column, and future schemes may provide momentum tendencies due to convective transport of momentum. The schemes all provide the convective component of surface rainfall. Cumulus parameterizations are theoretically only valid for coarser grid sizes, (e.g., greater than 10 km), where they necessary to properly release latent heat on a realistic time scale in the convective columns. Where the assumptions about the convective eddies being entirely sub-grid-scale break down for finer grid sizes, sometimes these schemes have been found to be helpful in triggering convection in 5-10 km grid applications. Generally they should not be used when the model can resolve the convective eddies itself. These schemes are responsible for the sub-grid-scale effects of convective and shallow clouds. The schemes are intended to represent vertical fluxes due to unresolved updrafts and downdrafts and compensating motion outside the clouds.

2.5.2.1 Kain - Fritsch (KF) Scheme

In the KF scheme the condensates in the updraft are converted into precipitation when their amount exceeds threshold value. In this scheme, the convection consumes the convective available potential energy in a certain time scale. The KF scheme also includes the shallow convection other than deep convection. The shallow convection creates non-perceptible condensates and the shallowness of the convection is determined by a vertical extent of the cloud layer that is known by a function of temperature at LCL of rising air parcel. The KF scheme was derived from the Fritsch–Chappell, and its fundamental framework and closure assumptions are described by Fritsch and Chappell (1980). KF (1990) modified the updraft model in the scheme and later introduced numerous other changes, so that it eventually became distinctly different from the Fritsch–Chappell scheme. It was distinguished from its

parent algorithm by referring to the more elaborate code as the KF scheme, beginning in the early 1990s. This is also deep and shallow convection sub-grid scheme using a mass flux approach with downdrafts and CAPE removal time scale. Updraft generates condensate and dump condensate into environment downdraft evaporates condensate at a rate that depends on RH and depth of downdraft leftover condensate accumulates at surface as precipitation.

2.5.3 Planetary Boundary Layer (PBL)

The PBL is the layer in the lower part of the troposphere with thickness ranging from a few hundred meters to a few kilometers within which the effects of the Earth's surface are felt by the atmosphere. The PBL processes represent a consequence of interaction between the lowest layer of air and the underlying surface. The interactions can significant impact on the dynamics of the upper air flows. The influences of the small-scale eddy on large scale atmospheric circulations may be included in the model equations. Accurate depiction of meteorological conditions, especially within the PBL, is important for air pollution modeling, and PBL parameterization schemes play a critical role in simulating the boundary layer. It is a very important portion of the atmosphere to correctly model to provide accurate forecasts, e.g., air pollution forecasts (Deardorff, 1972; Pleim, 2007). As important as the PBL is, it has one basic property whose accurate and realistic prediction is paramount to its correct modeling: its height. After all, the height of the top of the PBL defines its upper boundary. This is critical since PBL parameterizations schemes in WRF-ARW models need to know the extent through which to mix properties such as heavy rainfall, relative humidity, outgoing long wave flux, downward long wave flux.

PBL schemes were developed to help resolve the turbulent fluxes of heat, moisture, and momentum in the boundary layer. Another important issue is the interaction between the atmosphere and the surface. The PBL schemes handle the latent and sensible heat fluxes into the atmosphere, the frictional effects with the surface and the strong sub–grid–scale mixing which takes place in the lower levels due to these processes.

2.5.3.1 Yonsei University (YSU) Scheme

The Yonsei University (YSU) PBL is the next generation of the Medium Range Forecast (MRF), Non local-K scheme with explicit entrainment layer and parabolic K profile in unstable mixed layer. The YSU scheme is a bulk scheme that expresses non-local mixing by convective large eddies. Non-local mixing is achieved by adding a non-local gradient

adjustment term to the local gradient. At the top of the PBL, the YSU scheme uses explicit treatment of the entrainment layer, which is proportional to the surface layer flux (Shin and Hong, 2011; Hong *et al.*, 2006).

2.5.4 Map Projection

Commonly, a map projection is a systematic transformation of the latitudes and longitudes of locations on the surface of a sphere or an ellipsoid into locations on a plane. Map projections are necessary for creating maps. All map projections distort the surface in some fashion. Depending on the purpose of the map, some distortions are acceptable and others are not; therefore, different map projections exist in order to preserve some properties of the sphere-like body at the expense of other properties. There is no limit to the number of possible map projections. More generally, the surfaces of planetary bodies can be mapped even if they are too irregular to be modeled well with a sphere or ellipsoid. Even more generally, projections are the subject of several pure mathematical fields, including differential geometry and projective geometry. However, map projection refers specifically to a cartographic projection (Snyder, 1989).

2.5.4.1 Mercator projection

The Mercator projection is a cylindrical map projection presented by the Flemish geographer and cartographer Gerardus Mercator in 1569. It became the standard map projection for nautical purposes because of its ability to represent lines of constant course, known as rhumb lines loxodromes, as straight segments which conserve the angles with the meridians. While the linear scale is equal in all directions around any point, thus preserving the angles and the shapes of small objects, the Mercator projection distorts the size and shape of large objects, as the scale increases from the Equator to the poles, where it becomes infinite. Although the Mercator projection is still used commonly for navigation, due to its unique properties, cartographers agree that it is not suited to general reference world maps due to its distortion of land area. Mercator himself used the equal-area sinusoidal projection to show relative areas. As a result of these criticisms, modern atlases no longer use the Mercator projection for world maps or for areas distant from the equator, preferring other cylindrical projection or forms of equal-area projection. The Mercator projection is still commonly used for areas near the equator, however, where distortion is minimal.

2.5.5 Arakawa Staggered C-grids

The Arakawa grid system depicts different ways to represent and compute orthogonal physical quantities on rectangular grids used for Earth system models for meteorology and oceanography. For example, the Weather Research and Forecasting Model use the Arakawa Staggered C-Grid in its atmospheric calculations when using the ARW core. The staggered Arakawa C-grid further separates evaluation of vector quantities compared to the Arakawa B-grid. E.g., instead of evaluating both east-west (u) and north-south (v) velocity components at the grid center, one might evaluate the u components at the centers of the left and right grid faces, and the v components at the centers of the upper and lower grid faces (Arakawa and Lamb1977)

2.5.6 Shortwave Radiation

Shortwave radiation is radiant energy with wavelengths in the visible, ultraviolet, and near-infrared spectra. There is no standard cut-off for the near-infrared range; therefore, the shortwave radiation range is also variously defined. It may be broadly defined to include all radiation with a wavelength between 0.1 and 5.0μm or narrowly defined so as to include only radiation between 0.2μm and 3.0μm. There is little radiation flux to the Earth's surface below 0.2μm or above 3.0μm, although photon flux remains significant as far as 6.0μm, compared to shorter wavelength fluxes.

2.5.7 Outgoing Long Wave Radiation (OLR)

Outgoing long wave radiation (OLR) is the emission to space of terrestrial radiation from the top of the earth's atmosphere. In physical terms it is strongly controlled by three main meteorological variables, namely the temperature of the earth and the atmosphere above it, the presence of water vapor in that atmosphere (which strongly absorbs infrared radiation attenuating the terrestrial signal) and the presence of clouds (which may completely block all outgoing infrared radiation from the surface). Thus, global maps of OLR averages and anomalies reveal information on the temperature, humidity and cloudiness of the atmosphere. The equation of outgoing long wave radiation can be written as,

$$L^{\uparrow} = \varepsilon_S \sigma T_S^4 \text{ (W m}^{-2)} \quad (11)$$

Where ε_S is the emissivity of the surface in the long wave wavelength region, σ is the Stephan-Boltzmann constant $=\left(5.67\times10^{-8}\right)$ and T_s the absolute surface temperature. For most surface types ε_S is close to 1. Note that if $\varepsilon_S<1$ a part of the incoming long wave radiation is reflected by the surface. Equation (1) now reads as:

$$L^{\uparrow}=\varepsilon_S\sigma T_S^4+\left(1-\varepsilon_S\right)L^{\uparrow}\ (\text{W m}^{-2}) \qquad (12)$$

Where $L^{\downarrow}$ is the incoming long wave radiation. So OLR is a critical component of the Earth's energy budget that represents the total radiation going to space emitted by the atmosphere. Earth's radiation balance is quite closely achieved since the OLR very nearly equals the shortwave absorbed radiation received at high energy from the sun. Thus, the Earth's average temperature is very nearly stable. The OLR is affected by clouds and dust in the atmosphere, which tend to reduce it to below clear sky values. The minimum in OLR, or the longwave emitted flux near the equator is due to the high cloud tops associated with the inter-tropical convergence zone (ITCZ), a region of persistent thunderstorms. This minimum migrates about the equator as seen in the monthly mean maps, and is also seen as a maximum in albedo.

2.5.8 Downward long wave radiation flux

Long wave radiation flux is an important part of the surface heat budget, is generally represented by $\varepsilon\sigma T_r^4$, where ε is the surface emissivity, σ is the Stefan–Boltzmann constant, and T_r is the measured radiometric temperature. *EσTr4* differs from hemispheric emission because the measured radiometric temperature is anisotropic for an uneven surface. The flux difference between $\varepsilon\sigma T_r^4$ and directly measured flux was up to 8% of the directly measured flux, which could be greater than the typical error in measurement of turbulent heat flux over a building canopy. The flux difference increased as the temperature variation within the urban street canyon increased, and also with increasing difference between the incident solar radiation of the building walls and street canyon floors (pavement, roads, ground surface). Theoretical calculations indicate that the flux difference is due to the structure of the building canopy and the temperature difference between the walls and canopy floors. A numerical model of a building canopy heat budget shows that the flux difference increases as the street canyon aspect ratio increases.

Chapter-3
Model Description and Methodology

The Weather Research and Forecast (WRF-ARW Version 3.8.1) model consists of fully compressible non-hydrostatic equations and different prognostic variables is utilized in the present study. The model vertical coordinate is terrain following hydrostatic pressure and the horizontal grid is Arakawa C-grid staggering. Third-order Runge-Kutta time integration is used in the model. The model description and methodology are given below:

3.1 Model Description

The model is configured in single domain, 9 km horizontal grid spacing with 291×317 grids in the west-east and north-south directions and 19 vertical levels. The four different microphysics used for sensitivity study are WSM 6-class, Thompson, WDM6 and NSSL mom-1 schemes for explicit moisture processes. WSM6 and Thompson MP schemes contain prognostic equations for cloud water, rainwater, cloud ice, snow, and graupel mixing ratio.WDM6 scheme predicts the mixing ratios of six water species (water vapor, cloud droplets, cloud ice, snow, rain, and graupel), similar to WSM6. Prognostic water substance variables include water vapor, clouds, rain, ice, snow, and graupel for both the WDM6 and WSM6 schemes. NSSL mom-1 scheme contain prognostic equation for the larger precipitation categories for graupel and hail.

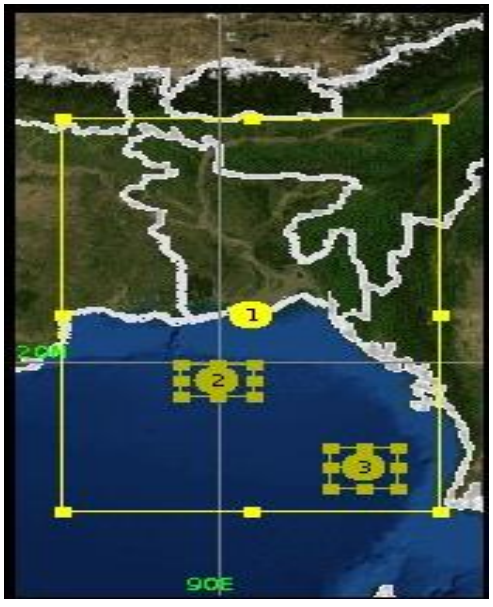

Figure 3.1: The WRF–ARW domain set up for the study.

To examine the impact of moisture of TC we have used those schemes for the simulation of TC Hudhud and TC Mora. The cumulus parameterization (CP) scheme has been used in WRF model is Kain-Fritsch (KF). The detail of the model and domain configuration is given in Table 3.1:

Table 3.1: WRF Model and Domain Configurations

Dynamics	Non-hydrostatic
Number of domain	1
Horizontal grid distance	9 km
Integration time step	45 s
Number of grid points	X-direction 291 points, Y-direction 317 points
Map projection	Mercator
Horizontal grid distribution	Arakawa C-grid
Nesting	One way
Vertical co-ordinate	Terrain-following hydrostatic-pressure co-ordinate (19 sigma levels up to 100 hPa)
Time integration	3rd order Runge-Kutta
Spatial differencing scheme	6th order centered differencing
Initial conditions	Three-dimensional real-data (FNL: 1°× 1°)
Lateral boundary conditions	Specified options for real-data
Top boundary conditions	Gravity wave absorbing
Bottom boundary conditions	Physical or free-slip
Diffusion and Damping	Simple Diffusion
Microphysics	1) WSM6 (2) Thompson (3) WDM6 (4) NSSL mom-1 scheme.
Radiation scheme	Dudhiafor short wave radiation/ RRTM long wave Mlawer *et al.*,(1997)
Surface layer	Monin– Obukhov similarity theory scheme
Land surface parameterization	5 Layer Thermal diffusion scheme (Ek *et al.*, 2003)
Cumulus parameterization schemes	Kain-Fritsch scheme (KF),
PBL parameterization	Yonsei University Scheme (YSU) scheme

3.2 Data and Methodology

Final Reanalysis (FNL) data (1^o x1^o) collected from National Centre for Environment Prediction (NCEP) is used as initial and lateral boundary conditions (LBCs) which is updated at six hours interval i.e. the model is initialized with 0000, 0600, 1200 and 1800 UTC initial field of corresponding date. The NCEP FNL data is interpolated to the model horizontal and vertical grids and the model was integrated for 168, 144, 120 and 96-h period for Hudhud and Mora.

8 experiments have been conducted in each case by using different microphysics schemes (e.g., WSM6-class graupel scheme, Thompson graupel, WDM6 scheme and NSSL mom-1) in combinations with Kain-Fritsch (KF) CP scheme with different initial conditions. In this regard, the initial conditions of 0000 UTC of 6, 7, 8 and 9 October 2014 have been considered for TC Hudhud and 25, 26, 27 and 28 May 2017 for TC Mora. The different periods for different cyclones were characterized by the formation of TC until dissipation.

Table 2: Observed information of simulated TC in the Bay of Bengal

Name of TC	Place of landfall	Date of Formation	Date and Time of landfall UTC	Minimum SLP, hPa	Maximum Sustained Wind Speed, km/h
Hudhud	Visakhapatnam, India	7 October	0630 and 0730 UTC of 12 October 2014	950	260
Mora	Chittagong, Bangladesh	30 May	0400 UTC and 0500 UTC of 30 May 2017	978	111

The model simulated MSLP, maximum wind at 10 m level, track, Convective available potential energy (CAPE), Convective inhibition (CIN), Water vapor mixing ratio (WVMR), Temperature anomaly, Relative Humidity (RH), Specific Humidity (SH), Wind Speed (WS), Wind Direction (WD) have been analyzed. Simulated track and intensity have also been compared with the IMD observed results. We have considered two different regions inside the model domain into two regions are Front (22-26^{o}N & 87-93^{o}E), Rear (18-22^{o}N & 81-85^{o}E) for Hudhud and Front (14-18^{o}N & 78-84^{o}E) and Rear (12-22^{o}N & 85-94^{o}E) for Mora

We have calculated the impact of environmental moisture on the intensification of TC in different regions by using the software Grid Analysis and Display Systems (GrADS).The Grid

Analysis and Display System (GrADS) is an interactive desktop tool that is used for easy access, manipulation, and visualization of earth science data. GrADS have two data models for handling gridded and station data. GrADS supports many data file formats, including binary (stream or sequential), GRIB (version 1 and 2), Net CDF, HDF (version 4 and 5), and BUFR (for station data). GrADS have been implemented worldwide on a variety of commonly used operating systems. GrADS use a 5-Dimensional data environment: the four conventional dimensions (longitude, latitude, vertical level, and time) plus an optional 5th dimension for grids that is generally implemented but designed to be used for ensembles. Data sets are placed within the 5-D space by use of a data descriptor file. GrADS handles grids that are regular, non-linearly spaced, Gaussian, or of variable resolution. Data from different data sets may be graphically overlaid, with correct spatial and time registration. Operations are executed interactively by entering FORTRAN-like expressions at the command line. A rich set of built-in functions are provided, but users may also add their own functions as external routines written in any programming language. Data may be displayed using a variety of graphical techniques: line and bar graphs, scatter plots, smoothed contours, shaded contours, streamlines, wind vectors, grid boxes, shaded grid boxes, and station model plots. Graphics may be output in PostScript or image formats. GrADS provides geo physically intuitive defaults, but the user has the option to control all aspects of graphics output. After getting txt data from grads we converted it into Excel sheet and plotted graph using Excel. We have plotted the data on Excel at every 24 hourly intervals for observing the changing scenario of energy and its fluxes for the movement of TCs.
Paint (formerly Paintbrush for Windows) is a simple computer graphics program that has been included with all versions of Microsoft Windows. It is often referred to as MS Paint or Microsoft Paint. The program mainly opens and saves files as Windows bitmap (24-bit, 256 color, 16 color, and monochrome, all with the .bmp extension), JPEG, GIF. We have converted our Excel graph into Paint and then transferred to Word.

Chapter IV

Results and Discussion

The model has simulated MSLP, maximum wind at 10 m level, track, Convective available potential energy (CAPE), Convective inhibition (CIN), Water vapor mixing ratio (WVMR), Temperature anomaly, Relative Humidity (RH), Specific Humidity (SH), Wind Speed (WS) and Wind direction for cyclone Hudhud and Mora. The parameters have been studied and analyzed for two cyclones. Simulated tracks and intensity have also been compared with the IMD observed results. The results have been presented in the following sub sections.

4.1 Tropical Cyclone Hudhud

4.1.1 Synoptic Situation of Tropical Cyclone Hudhud

The Very Severe Cyclonic Storm 'Hudhud' developed from a low pressure area which lay over Tenasserim coast and adjoining North Andaman Sea in the morning of 6 October 2014. It concentrated into a Depression in the morning of 7 October over the North Andaman Sea. Moving west-northwestwards it intensified into a Cyclonic Storm (CS) on 8 October and crossed Andaman Islands close to Long Island between 0300 and 0430 UTC of 8 October. It then emerged into Southeast Bay of Bengal (BoB) and continued to move west-northwestwards. It intensified into a Severe Cyclonic Storm (SCS) on 9 October and further into a Very Severe Cyclonic Storm (VSCS) in the afternoon of 10 October. It continued to intensify further while moving northwestwards and reached maximum intensity in the early morning of 12 October with a maximum sustained wind speed (MSW) of 180 kmph over the West Central BoB off Andhra Pradesh coast. The VSCS 'Hudhud' crossed north Andhra Pradesh coast over Visakhapatnam between 0630 and 0730 UTC of 12 October. After landfall, it continued to move northwestwards for some time and weakened gradually into SCS in the evening and further into a CS in the midnight of same day. It then, weakened further into a DD in the early morning of 13 and weakened into a depression in the evening of 13 October 2014.

4.1.2 Minimum Sea Level Pressure (MSLP)

The model simulated MSLP of TC Hudhud using different MP schemes coupling with KF scheme with four different initial conditions at 0000 UTC of 6, 7, 8 and 9 October 2014 are presented in Figure 1(a-d). The model simulated MSLP values of 920, 922, 923 and 931 hPa

(Figure 1a) are found for Thompson, NSSL, WSM6 and WDM6 schemes respectively for the initial conditions at 0000 UTC of 6 October. For the initial conditions at 0000 UTC of 7 October, the model has also simulated MSLP for Thompson, NSSL, WSM6 and WDM6 schemes, which are 920, 920, 921 and 930 hPa (Figure 1b) respectively. The model simulated MSLP of 913, 920, 927 and 930 hPa (Figure 1c) are found for Thompson, WSM6, NSSL and WDM6 schemes respectively for the initial conditions at 0000 UTC of 8 October.

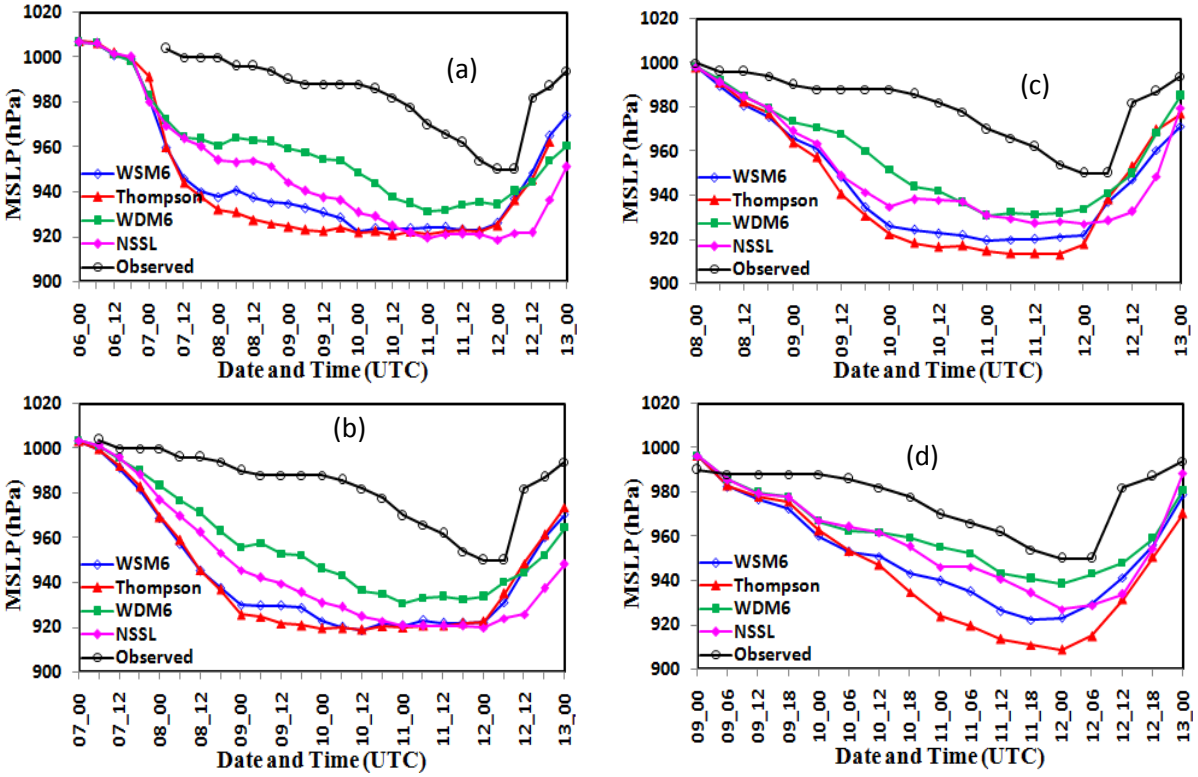

Figure 1: Model simulated (a-d) MSLP of TC Hudhud using four different MP schemes coupling with KF scheme with the initial conditions at 0000 UTC of 6, 7, 8 and 9 October 2014 respectively.

For the initial conditions at 0000 UTC of 9 October, the model simulated MSLP of 909, 922, 927 and 938 hPa (Figure 1d) are found for Thompson, WSM6, NSSL and WDM6 schemes respectively. The similar pattern of MSLP is found for all MPs with the initial conditions at 0000 UTC of 6, 7, 8 and 9 October. The model simulated pressure fall for different MPs with different initial conditions are much higher than that of IMD estimated pressure (950 hPa). The highest and lowest pressure fall are simulated by Thompson and WDM6 schemes respectively with different initial conditions.

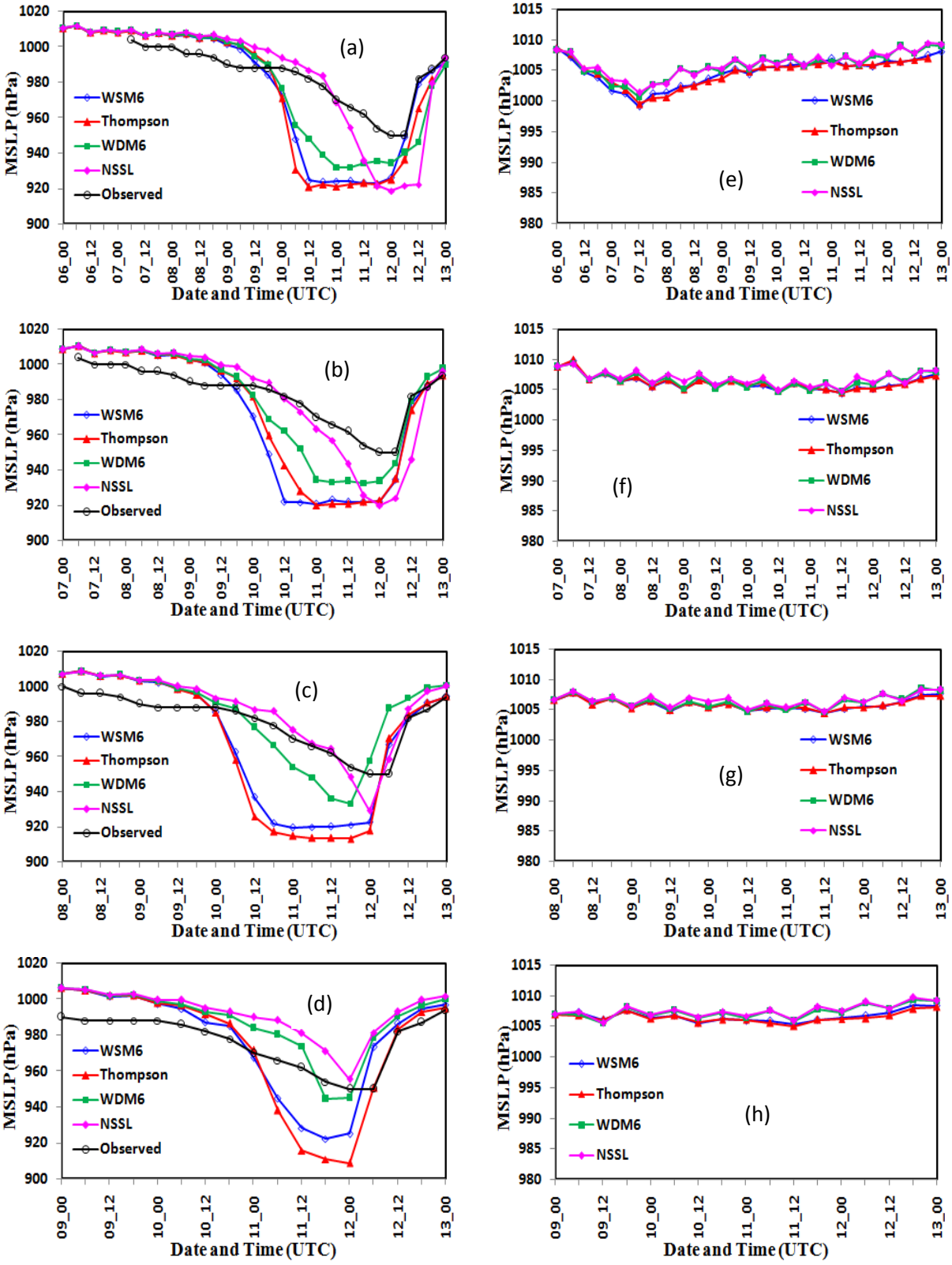

Figure 2: Model simulated MSLP (hPa) (a-d) at front and (e-h) at rear position of TC Hudhud using four different MP schemes coupling with KF scheme with the initial conditions at 0000 UTC of 6, 7, 8 and 9 October 2014 respectively.

The simulated MSLP at the front position of TC Hudhud for different initial conditions and for different MPs schemes are displayed in Figure 2(a-d). The simulated MSLP values are

918, 921, 922 and 932 hPa (Figure 2a) at 1800, 0000, 0600 UTC of 11 October and 0000 UTC of 12 October for NSSL, Thompson, WSM6 and WDM6 schemes respectively with the initial conditions at 0000 UTC of 6 October. The sharp fall of MSLP is simulated for WSM6, Thompson and WDM6 schemes much earlier than observed. For the initial conditions of 7 October, the Model has MSLP of front 920, 921, 933, 920 hPa (Figure 2b) at 0000, 1800, 0600 UTC of 11 October and 0000 UTC of 12 October for Thompson, WSM6, WDM6 and NSSL schemes respectively. The sharp fall of MSLP is seen for WSM6 and Thompson schemes much earlier than observed. The MSLP values are found 913, 919, 929 and 933 hPa (Figure 2c) at 1800, 0000, 1800 UTC of 11 October and 0000 UTC of 12 October for Thompson, WSM6, NSSL and WDM6 schemes respectively for the initial conditions at 0000 UTC of 8 October. The sharp fall of MSLP is seen and reached minimum value and shows almost constant at 1800 UTC of 10 October to 0000 UTC of 12 October with the initial conditions at 0000 UTC of 8 October for Thompson and WSM6 schemes. For the initial conditions at 0000 UTC of 9 October, the MSLP has simulated 922 and 944 hPa at the front position of the cyclone at 1800 UTC of 11 October and 955 and 909 hPa (Figure 2d) at 0000 of 12 October for WSM6, WDM6 NSSL and Thompson schemes respectively.

The model simulated MSLP at the rear position of TC Hudhud for different MPs schemes coupling with KF scheme are presented in Figures 2(e-h)). The simulated MSLP values at rear position are 999, 1000, 1001 and 1001 hPa for the initial conditions at 0000 UTC of 6 October (Figure 2e)and 1002, 1002, 1002 and 1003 hPa for the initial conditions at 0000 UTC of 7 October (Figure 2f) for WSM6, Thompson, WDM6 and NSSL schemes respectively. The simulated MSLP values at the rear position are found 1004, 1005, 1005 and 1005 hPa for the initial conditions at 0000 UTC of October (Figure 2g) and 1005, 1006, 1006 and 1006 hPa for the initial conditions at 0000 UTC of 9 October (Figure 2h) for Thompson, NSSL, WDM6 and WSM6 schemes respectively.

MSLP for TC Hudhud has found to decrease at front position with the progression of TC towards land after landfall it increased again and rear position SLP has increased continuously during the time of movement. WDM6 and NSSL schemes are closed to the IMD estimated SLP.

4.1.3 Maximum Wind Speed (MWS) at 10 m level

The model simulated MWSs using different MP schemes coupling with KF scheme with four different initial conditions at 0000 UTC of 6, 7, 8 and 9 October 2014 are presented in Figure

3(a-d). The MWSs 55, 55, 53 and 48 ms^{-1} are simulated (Figure 3a) at 0000 UTC of 9 October and 0600 and 1800 UTC of 10 October and 0600 UTC of 11 October MWSs of 55, 55, 53 and 50 ms^{-1} (Figure 3b) at 0000, 1800 UTC of 9 October and 0000 UTC of 12 October and 0600 UTC of 11 October for Thompson, WSM6, NSSL, and WDM6 schemes for the initial conditions at 0000 UTC of 6 and 7 October respectively.

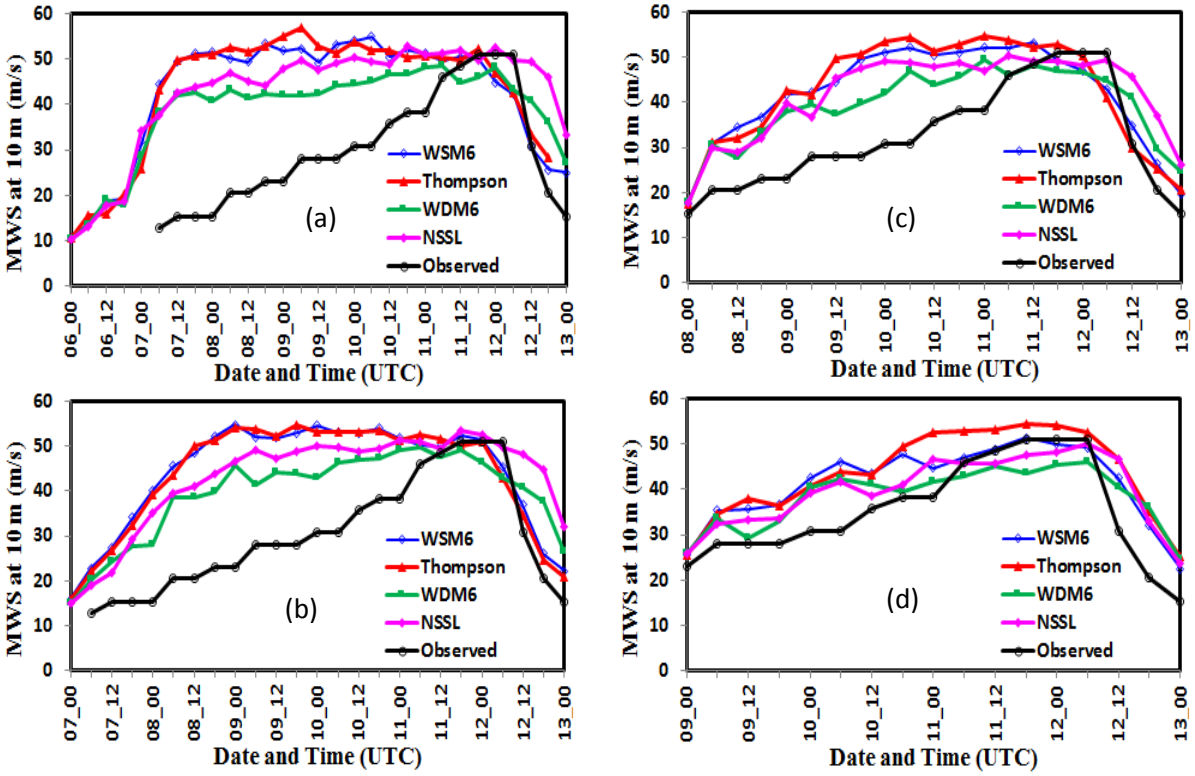

Figure 3: Model simulated (a-d) MWS at 10m level of TC Hudhud using four different MP schemes coupling with KF scheme with the initial conditions at 0000 UTC of 6, 7, 8 and 9 October 2014 respectively.

For the initial conditions at 0000 UTC of 8 (Figure 3c) and 9 (Figure 3d) Octobers the simulated MWS are 55, 53, 50 and 49 ms^{-1}at 0000, 1200, 0600 and 0000 UTC of 11 October and 54, 51, 50 and 46ms^{-1}at 1800 and 1800 UTC of 11 October and 0600 and 0600 UTC of 12 October for Thompson, WSM6, NSSL and WDM6 schemes respectively. The model simulated MWSs for different MPs with different initial conditions are almost similar to that of IMD observed (51 m s^{-1}) MWS. The highest and lowest MWS are simulated by Thompson and WDM6 schemes respectively with different initial conditions. The MWS at 10m level in front position is of the cyclone are 51 and 51 ms^{-1} at 1200 UTC of 10 October for WSM6 and Thompson schemes, and 47 and 53 ms^{-1} at 0000 UTC of 11 and 12 October for WDM6 and NSSL schemes respectively for the initial conditions at 0000 UTC of 6 October.

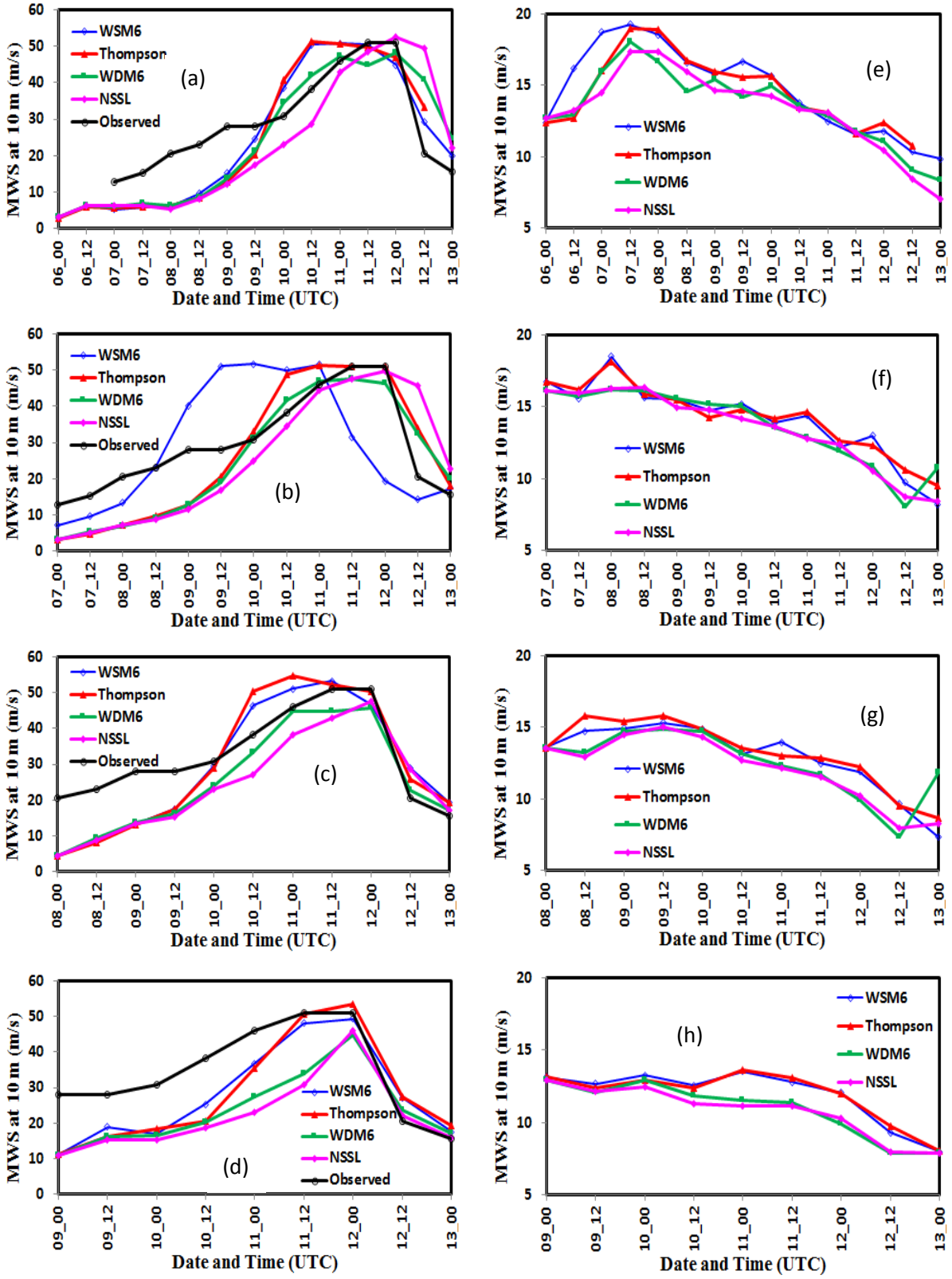

Figure 4: Model simulated MWS at 10 m level at (a-d) front and (e-h) rear position of TC Hudhud using four different MP schemes coupling with KF scheme with the initial conditions at 0000 UTC of 6, 7, 8 and 9 October 2014 respectively.

The MWS are found 51, 48, 47, and 49 ms^{-1} at 1200 UTC of 9 October, 1200 UTC of 10 and 11 October, 0000 UTC of 12 October for WSM6, Thompson, WDM6 and NSSL schemes

respectively for the initial conditions at 0000 UTC of 7 October (Figure 4(a-b)) respectively. The simulated MWS are 51, 48, 50 and 48 ms^{-1} at 0000 and 0000 UTC of 11, 1200 UTC of 10 and 0000 UTC of 12 October for WSM6, WDM6, Thompson and NSSL schemes respectively the initial conditions of 0000 UTC of 9 October. The MWS is simulated 45, 46, 49 and 54 m s^{-1} at 0000, 1200, 0000 UTC of 11 and 0000 UTC of 12 October for WDM6, NSSL, WSM6 and Thompson schemes (Figure 4(c-d)) respectively for the initial conditions of 0000 UTC of 9 October. The MWS at rear position are found 17, 18, 19, 19 ms^{-1} (Figure 4e) at 1200 UTC of 7 October, 16, 16, 18, 19 ms^{-1} (Figure 4f) at 0000 UTC of 8 October for NSSL, WDM6, Thompson and WSM6 schemes for the initial conditions of 0000 UTC of 6 and 7 October respectively.

For the initial conditions at 0000 UTC of 8 October, the MWS simulated are 14 and 15 ms^{-1} at 1200 UTC of 9 October and 15 and 16 ms^{-1} (Figure 4g) at 0000 UTC of 10 October for NSSL, WDM6, WSM6 and Thompson schemes respectively. The MWSs are found 12 and 13 ms^{-1} (Figure 4h) at 0000 UTC of 11 October, and 13 and 14 ms^{-1} at 1200 UTC of 12 October for NSSL, WDM6, Thompson and WSM6 schemes respectively for the initial conditions at 0000 UTC of 9 October. It is seen that the MWS at 10m level is found to decrease continuously with the movement of TC towards land.

4.1.4 Track of TC Hudhud

The model simulated tracks for prediction time 168, 144, 120 and 96-h model and IMD observed track of TC Hudhud for different MP schemes are presented in Figure 5(a-d). All the simulations have shown the north-northwestward movement of TC Hudhud with the initial conditions at 0000 UTC of 6, 7, 8 and 9 October 2014. The track forecasts for different sensitivity experiments have shown reasonably accurate prediction. WDM6 and Thompson schemes have simulated most deviated track and landfall time at 1700 and 0000 UTC of 11 October, and WSM6 and NSSL schemes have simulated less deviated and landfall time is 0500 UTC of 11 October and 0200 of 12 October with the (Figure 5a) initial conditions at 0000 UTC of 6 October 2014. The simulated track is deviated towards right from observed for all MPs with the initial conditions at 0000 UTC of 6 October 2014. For the initial conditions at 0000 UTC of 7 October 2014 (Figure 5b), WDM6 and WSM6 schemes have simulated most deviated track and landfall time is 0200 UTC of 12 October and 1000 UTC of 11 October respectively, and Thompson and NSSL schemes have simulated less deviated track and landfall time is 0000 UTC of 11 October and 0800 UTC of 12 October.

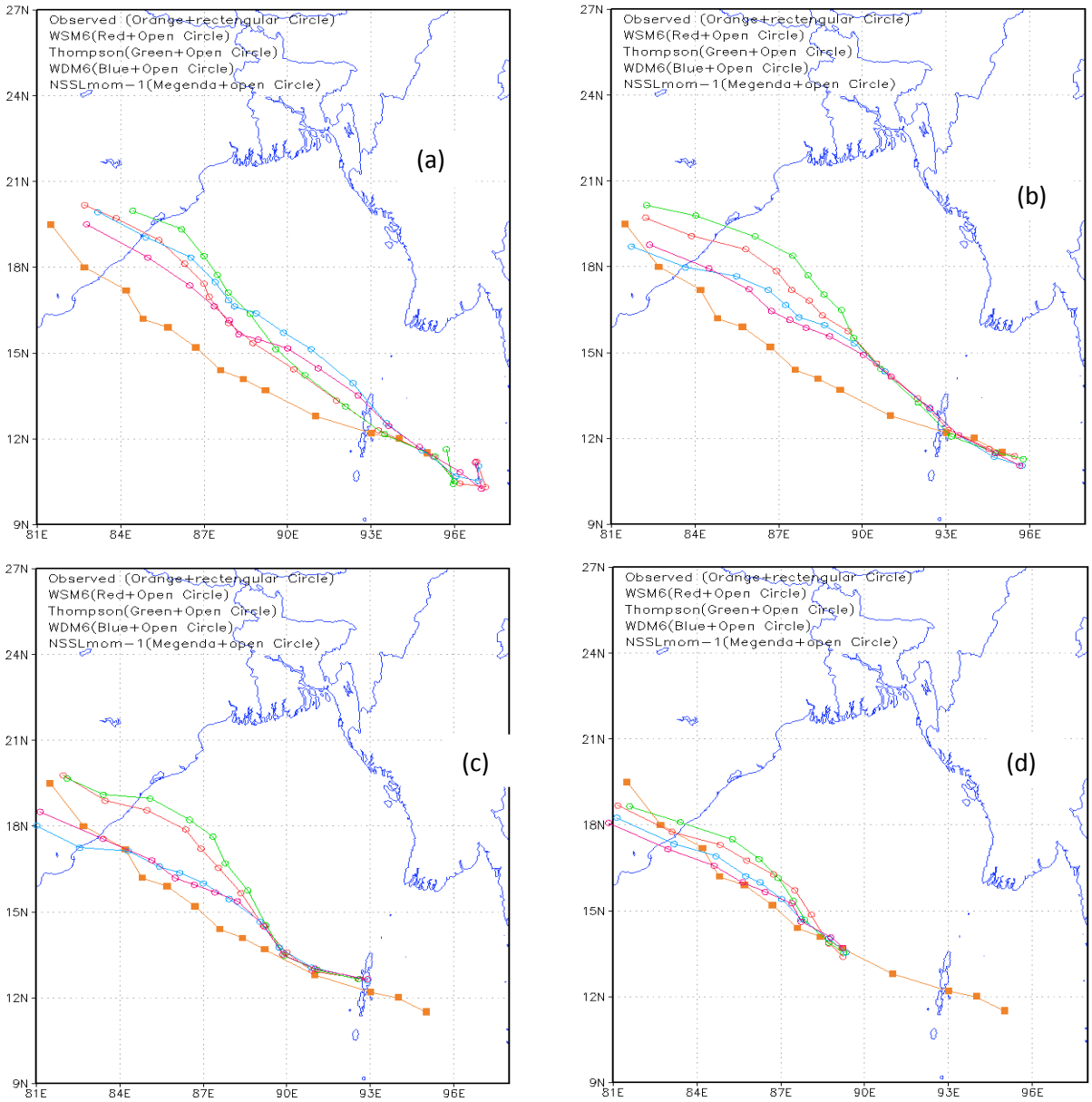

Figure 5: Model simulated and observed tracks of TC Hudhud using four different MP schemes coupled with KF scheme with the initial conditions at 0000 UTC of (a) 6 October, (b) 7 October, (c) 8 October and (d) 9 October respectively.

The simulated track for all MPs is deviated towards right for the initial conditions at 0000 UTC of 7 October. WSM6 and Thompson schemes have simulated most deviated track (Figure 5c) and landfall time is1100 and 0200 UTC of 11 October and WDM6 and NSSL schemes have simulated less deviated track and landfall time is 2200 and 1400 UTC of 12 October with the initial conditions at 0000 UTC of 8 October 2014. The track deviation is less for all MPs schemes with the initial conditions at 0000 UTC of 9 October (Figure 5d) and landfall times for WSM6, Thompson, WDM6 and NSSL schemes are 1100, 0500, 1900, 2200 UTC of 12 October. NSSL scheme gives the better results for the initial conditions at 0000 UTC of 6 and 7 October and WDM6 and Thompson schemes gives the better results for the initial conditions at 8 and 9 October.

4.1.5 Specific Humidity (SH)

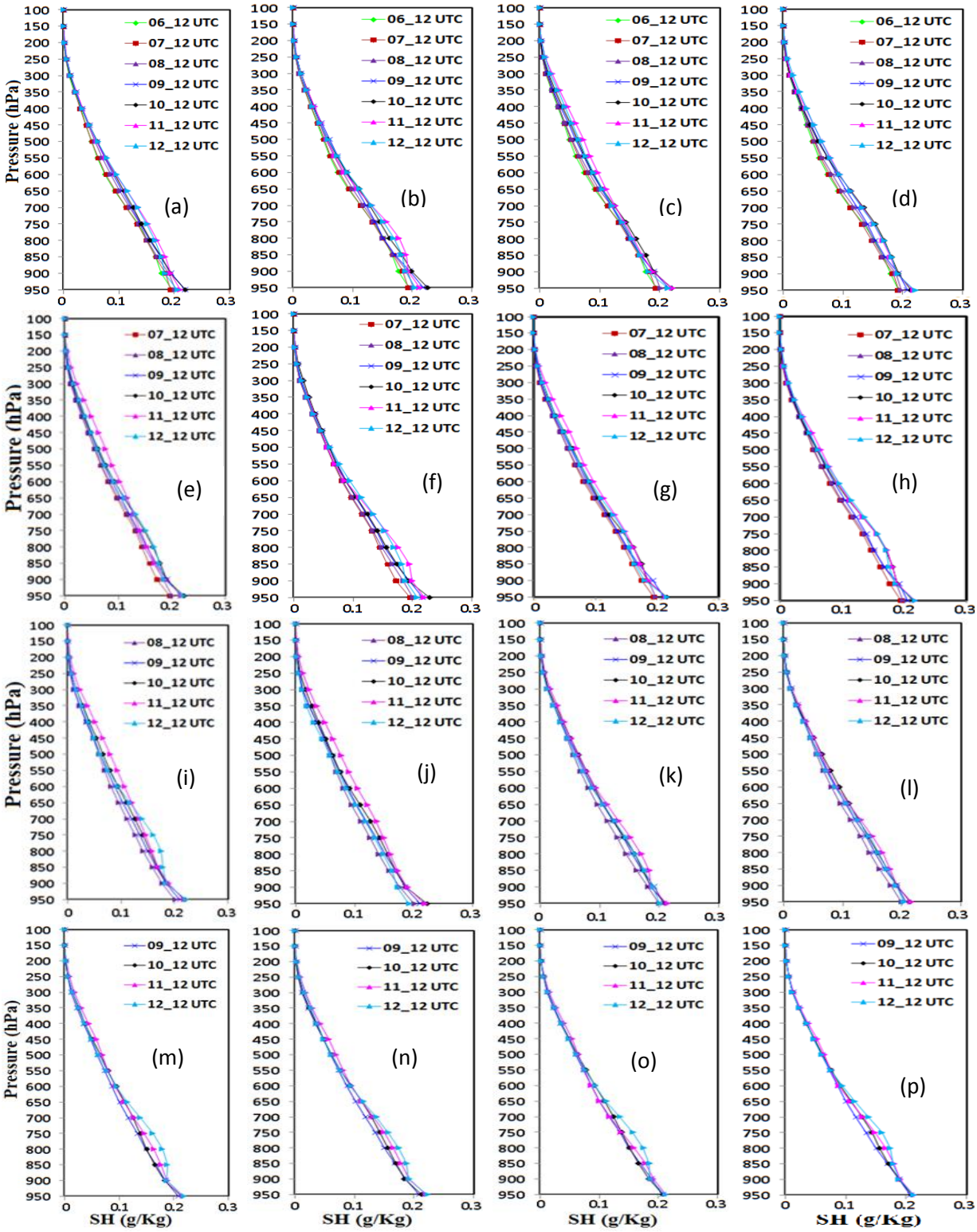

Figure 6: vertical profiles of Model simulated area averaged SH (g/kg)of TC Hudhud at 1200 UTC of different days at front position for four different MPs at (a-d) 6, (e-h) 7, (i-l) 8 and (m-p) 9October 0000 UTC initial conditions respectively.

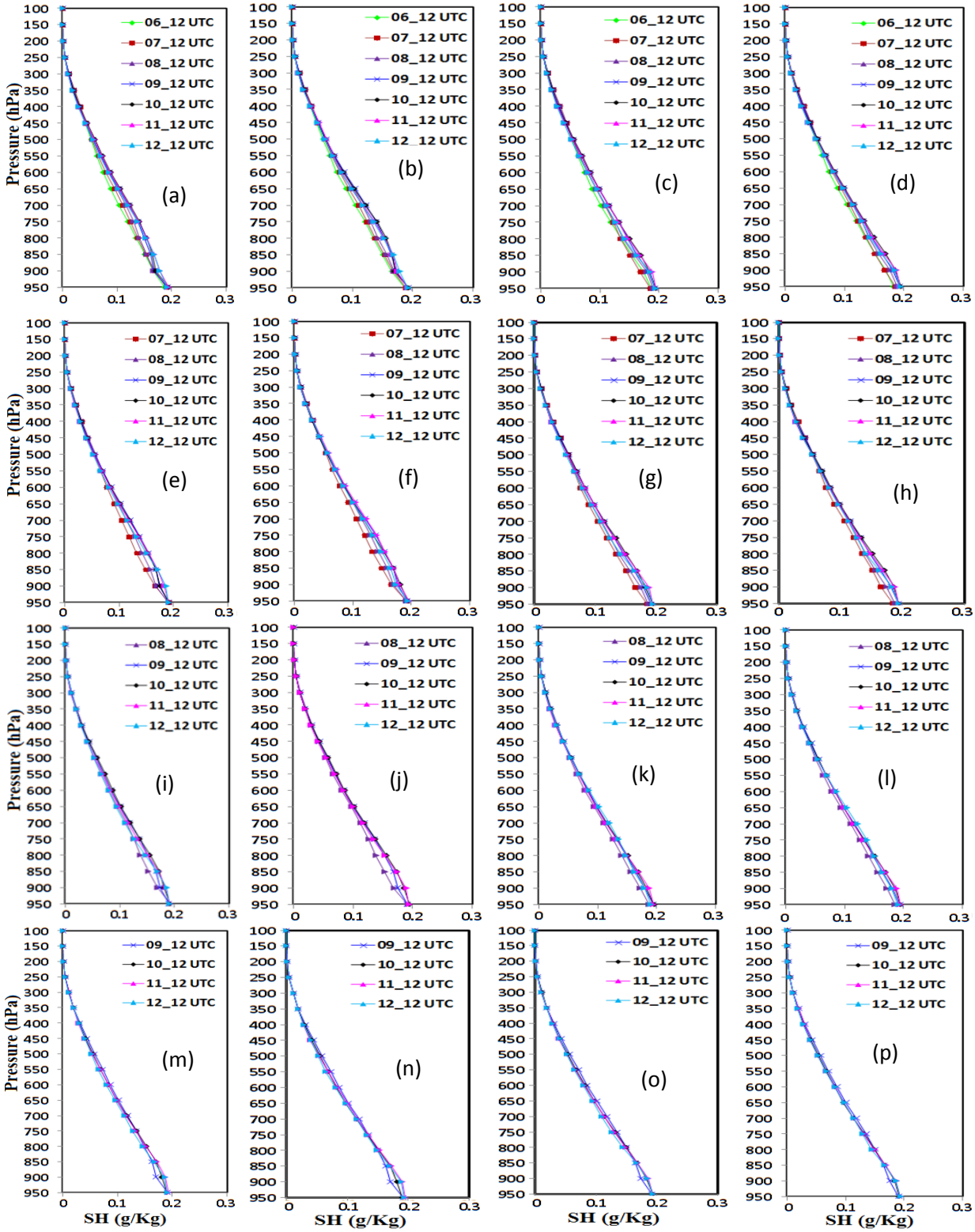

Figure 7: vertical profiles of Model simulated area averaged SH (g/kg) of TC Hudhud at 1200 UTC of different days at rear position for four different MPs at (a-d) 6, (e-h) 7, (i-l) 8 and (m-p) 9 October 0000 UTC initial conditions respectively.

Model simulated vertical variations of area averaged SH at the front position with four different MPs are presented in Figure 6(a-p) for the initial conditions at 0000 UTC of 6, 7, 8

and 9 October 2014. Maximum specific humidity is found at surface level. The distribution pattern of SH at 0000 UTC and 1200 UTC are almost similar so that variations of SH only at 1200 UTC are presented.

The vertical variations of area average SH at the front position show that SH is found to increase for all MP schemes during 6-11 October (Figure 6(a-d)), 7-11 October (Figure 6(e-h)) and 8-11 October (Figure 6(i-l)) after that it has decreased on 12 October except NSSL scheme, WSM6 & NSSL schemes and WSM6 scheme for the initial conditions of 0000 UTC of 6, 7 and 8 October respectively. The vertical variation of area average SH reveal that the SH increases for all MPs during 9-12 October (Figure 6(m-p)) with little exception in different levels for 0000 UTC of 9 October initial conditions.

The vertical variation of area average SH at rear position indicates that SH increases for all MPs up to 11 October with little anomalies for the 0000 UTC of 6 (Figure 7(a-d)), 7 (Figure 7(e-h)), 8 (Figure 7(i-l)) and 9 (Figure 7(m-p)) October initial conditions and after that it has decrease after passing out the landfall. It is found that the SH is increased as the cyclone propagates towards front position, it indicates that the cyclone moves in a direction where the SH increases.

4.1.6 Water Vapor Mixing Ratio (WVMR)

The temporal distribution of area average WVMR at 2 m level in front position for different MPs coupling with KF scheme of TC Hudhud is presented in Figure 8(a-h) for 0000 UTC of 6, 7, 8 and 9 October 2014 initial conditions. The area average WVMR at front position (Figure 8(a-d)) and rear position (Figure 8(e-h)) are found maximum for Thompson and minimum for WDM6 schemes using the initial conditions at 0000 UTC of 6, 7, 8 and 9 October 2014.

The simulated area average WVMR at front position (Figure 8a) for different MPs are almost constant during 0000 UTC of 6 October to 0000 UTC of 10 October and then WVMR has increased and reached maximum at 1200 UTC of 11 October for the initial conditions of 0000 UTC of 6 October. The area average WVMR is found maximum 22.8 g/kg and minimum 21.8 g/kg for Thompson and WDM6 schemes respectively. For the initial conditions of 0000 UTC of 7 October (Figure 8b) the temporal distribution of area average WVMR shown that WVMR has increased continuously with the progression of time for all MPs and reached Maximum at 1200 UTC of 11 October for different MPs respectively. The

area average maximum and minimum WVMR are found to be 23 and 21.4 g/kg for Thompson and WDM6 schemes respectively.

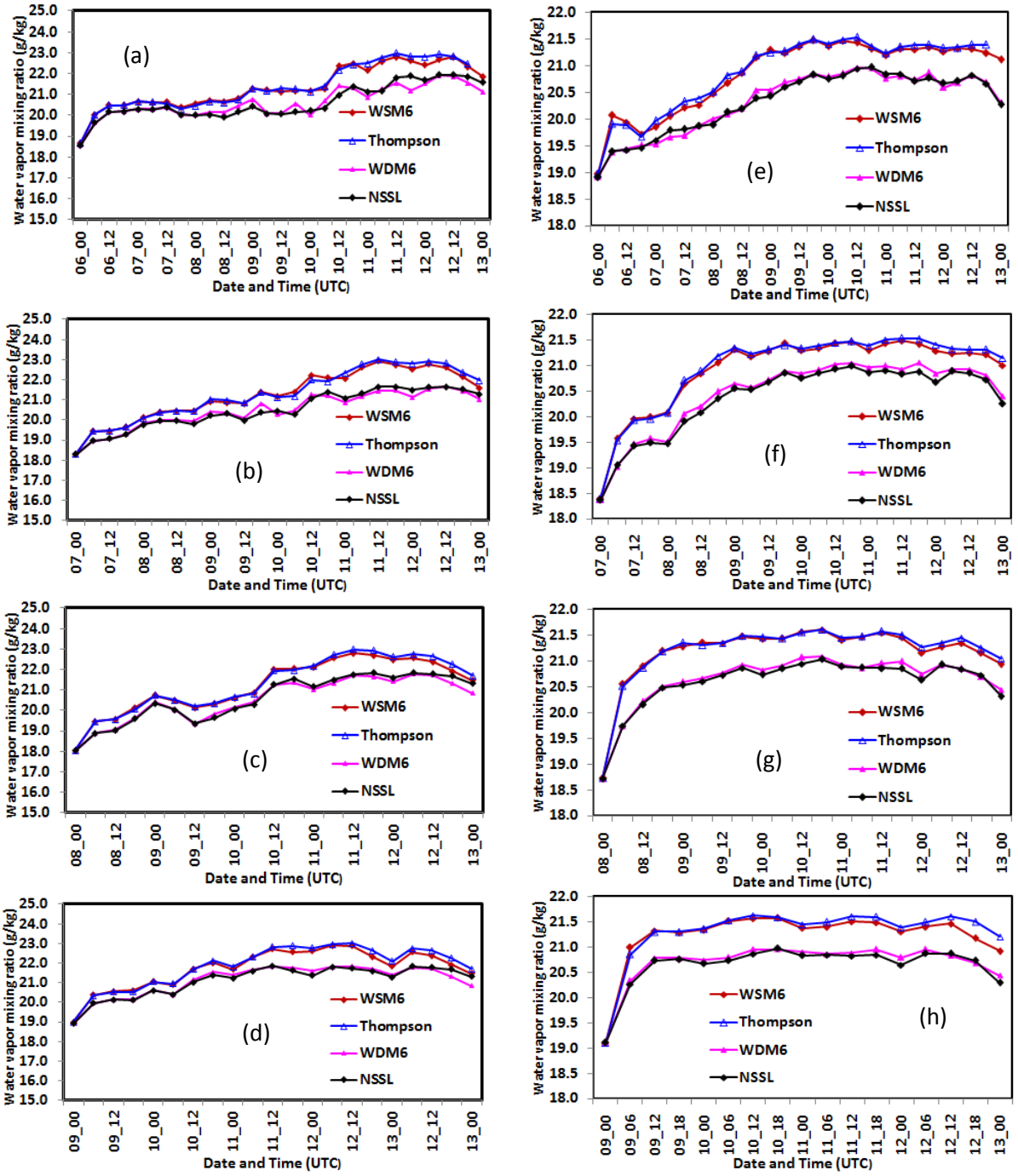

Figure 8: Model simulated area average WVMR of TC Hudhud for four different MPs at (a-d) front and (e-h) rear position with 0000 UTC of 6, 7, 8 and 9 October initial conditions respectively.

The temporal distribution of area average WVMR for all MPs (Figure 8c) has shown increasing tendency of WVMR except at 0000 to 1200 UTC of 9 October and reached maximum at 1200 UTC of 11 October for different MPs for the initial conditions at 0000 UTC of 8 October. The area average maximum and minimum WVMR are 23 and 21.7 g/kg

for Thompson and WDM6 schemes respectively. For the initial conditions at 0000 UTC of 9 October, the area average WVMR at front position (Figure 8d) has increased for all MPs and reached maximum at 0600 of 12 October for different MPs with little exception. The area average maximum and minimum WVMR are 23 and 21.8 g/kg for Thompson and NSSL schemes respectively.

The area average WVMR at rear position for all MPs has increased and reached maximum (Figure 8e) at 1800 UTC of 9 October for WSM6 and WDM6 schemes and 1200 and 1800 UTC of 10 October for Thompson and NSSL schemes respectively for the initial conditions at 0000 UTC of 6 October. The maximum and minimum WVMR are 21.5 and 20.8 g/kg for Thompson and NSSL schemes respectively. For the initial conditions of 0000 UTC of 7 (Figure 8f) and 8 (Figure 8g) October, the area average WVMR for all MPs has increased up to 0000 UTC of 9 October and after that it shows almost constant values. The area average maximum and minimum WVMR are 21.5 and 21 g/kg and 21.6 and 21 g/kg for Thompson and NSSL schemes based on the initial conditions on 7 and 8 October respectively. The area average WVMR (Figure 8h) is found to increase till 1200 UTC of 9 October and after that it shows almost constant values for all MPs for the initial conditions of 0000 UTC of 9 October. The maximum and minimum WVMR are 22 and 21 g/kg for Thompson and WDM6 schemes. It is found that the WVMR is increased as the cyclone propagates towards the front position; it indicates that the cyclone moves in a direction where the WVMR increases.

4.1.7 Relative Humidity (RH)

Model simulated vertical profiles of area averaged RH (%) at the front position with four different MPs coupling with KF scheme are presented in Figures 9(a-p) for initial conditions at 0000 UTC of 6, 7, 8 and 9 October 2014. The simulated RH has been found below 90% from surface to 100 hPa levels for all MPs on 6, 7, 8, and 9 October 2014. From figure 9, it is seen that the simulated RH is minimum at around 400-100 hPa. The distribution pattern of RH at 0000 UTC and 1200 UTC are almost similar so that only 1200 UTC graphs are presented. The vertical variation of area average RH Shows that RH increases for WSM6, Thompson, WDM6 and NSSL schemes (Figure 9(a-d)) during 6-7 October and 9-11 October after that it has decreased on 12 October with little exception for the initial conditions of 0000 UTC of 6 October. The vertical variation of area average RH is found to increase throughout the troposphere for all MPs during 8-11 (Figure 9(e-h)) and decrease on 12 October with little exception for the initial conditions of 0000 UTC of 7 October.

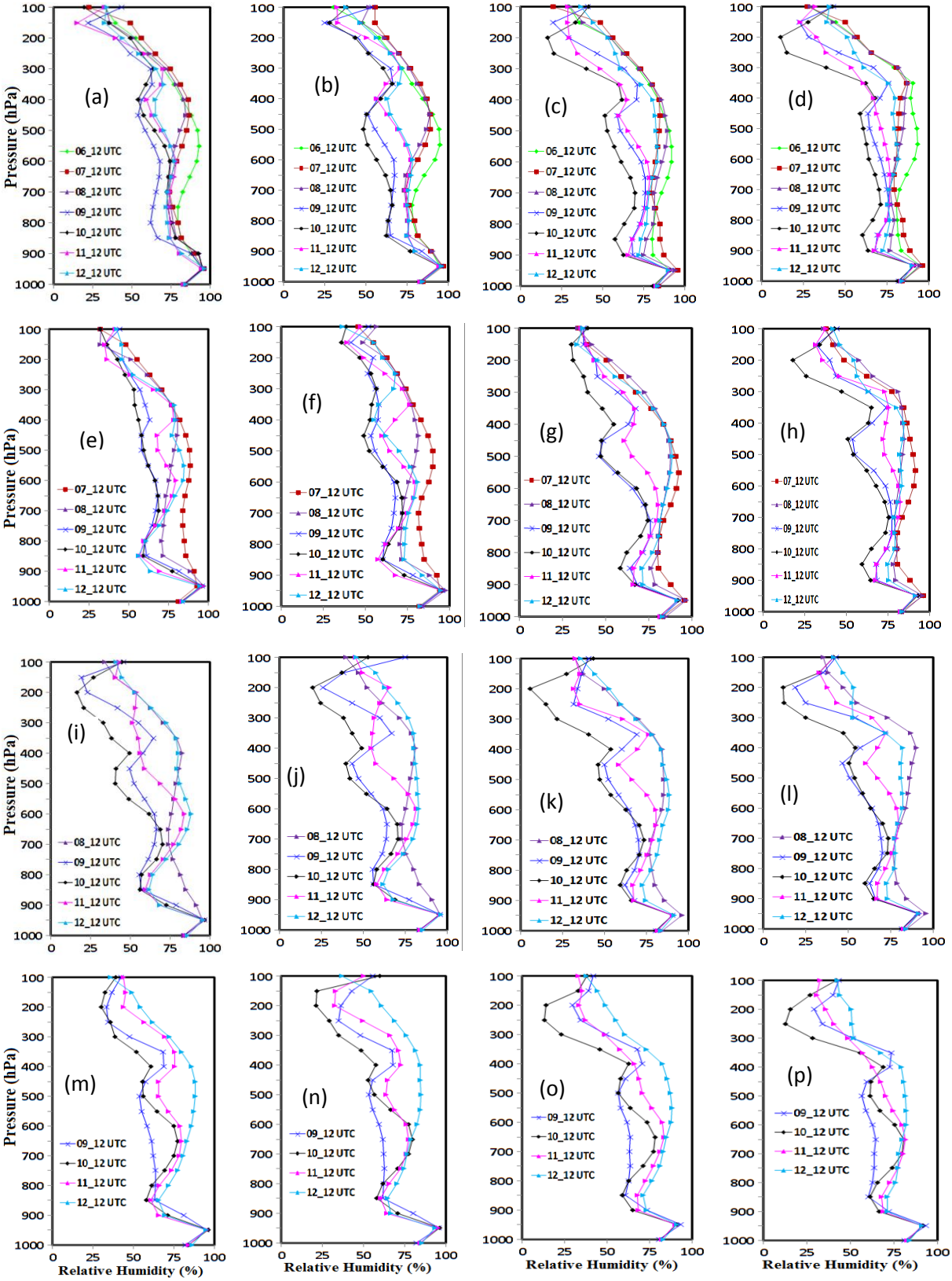

Figure 9: Model simulated area averaged RH (%) at 1200 UTC of different days in front position of TC Hudhud for four different MPs at 0000 UTC initial conditions of (a-d) 6, (e-h) 7, (i-l) 8 and (m-p) 9October 2014 respectively.

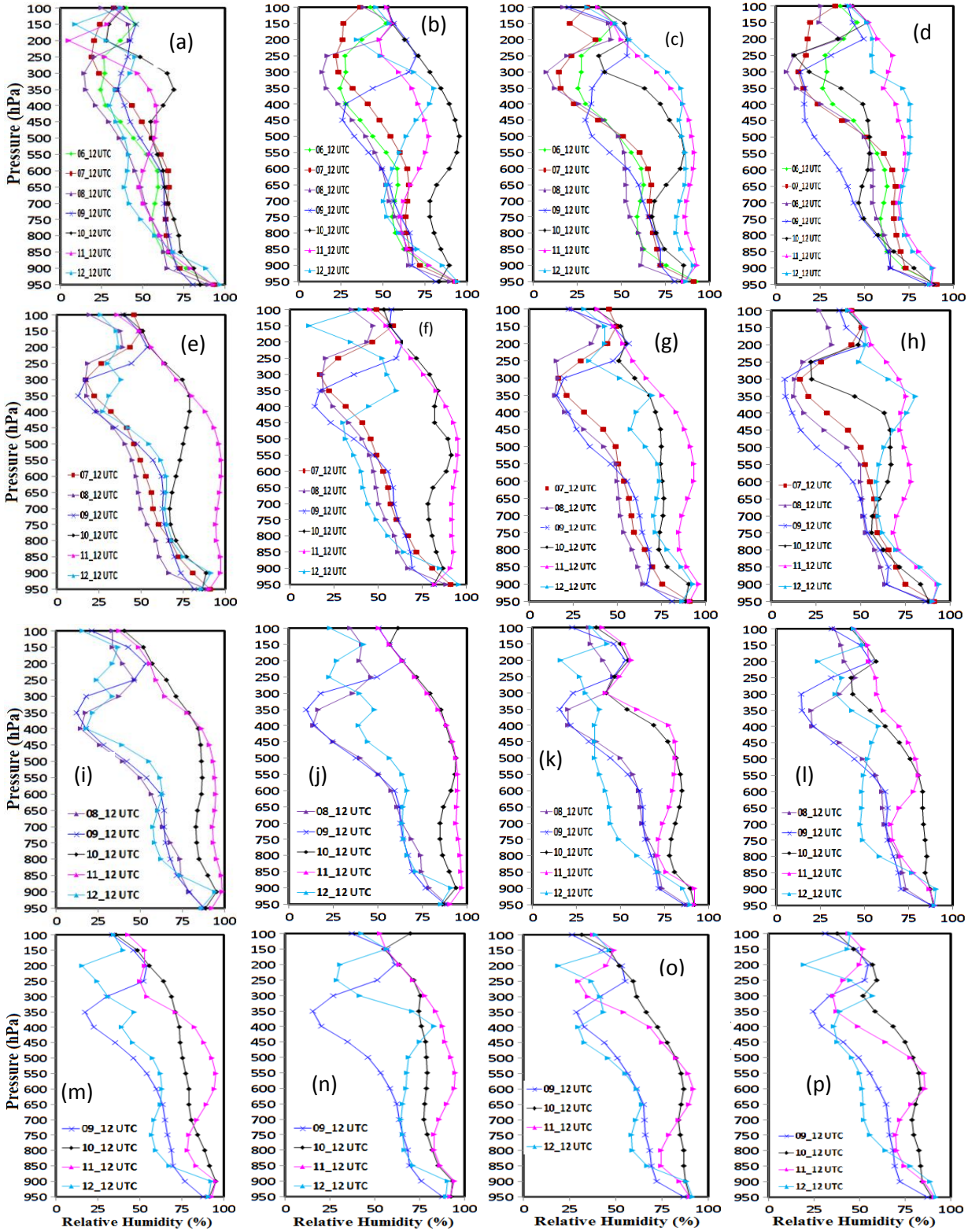

Figure 10: Model simulated area averaged RH (%) at 1200 UTC of different days in rear position of TC Hudhud for four different MPs at 0000 UTC initial conditions of (a-d) 6, (e-h) 7, (i-l) 8 and (m-p) 9 October 2014 respectively.

For the initial conditions of 0000 UTC of 8 October, the area average RH is found to increase with the progress of the days for all MP schemes during 9-11 October (Figure 9(i-l)) and it

has decreased on 12 with little exception in different levels. The vertical variation of area average RH is found to increase for all MP schemes during 9-11 October (Figure 9(m-p)) and decrease on 12 October with little exception for the initial conditions of 0000 UTC of 9 October.

Vertical variations of area averaged RH (%) at rear position with four different MPs coupling with KF scheme for the initial conditions at 0000 UTC of 6, 7, 8 and 9 October 2014 are presented in Figs 10(a-p). The area average RH is found to decrease throughout the troposphere for WSM6, Thompson, WDM6 and NSSL schemes during (Figure 10(a-d)) 6-10 October and found to increase on 11-12 October with little exception for the initial conditions of 0000 UTC of 6 October.

The area average RH is found to decrease throughout the troposphere for all MPs during (Figure 10(e-h)) 7-10 and Then found to increase till 12 October with little exception for the initial conditions of 0000 UTC of 7 October. For the initial conditions of 0000 UTC of 8 October, the area average RH is found to decrease for all MP schemes during 8-10 October (Figure 10(i-l)) and it has increased up to 12 October throughout the troposphere with little exception in different levels. The area average RH is found to increase for all MP schemes during 9-12 October (Figure 10(m-p)) for the initial conditions of 0000 UTC of 9 October. The RH is found to increase at front position and decrease at rear position from the starting of model run to 11 October and after that it has increased at rear position and decreased at front position. The cyclone moves in a region where the RH is found to increase.

4.1.8 Temperature anomaly

The model simulated temperature anomalies at the front and rear positions at 0000 UTC of 6, 7, 8, and 9 October 2014 for WSM6, Thompson, WDM6 and NSSL schemes coupling with KF scheme are presented in Figures 11(a-p) and 12(a-p). The area average temperature anomaly is found positive from 950 hPa to150 hPa for all initial conditions. The distribution patterns of temperature at 0000 UTC and 1200 UTC are almost similar so that only 1200 UTC graphs are presented for analysis.

The area average temperature is increased continuously at different vertical levels at front position of TC Hudhud for WSM6, Thompson, WDM6 and NSSL schemes from the initial conditions of model run to 1200 UTC of 11 October and is decreased at 1200 UTC of 12 October with little exception for the initial conditions of 0000 UTC of 6 (Figure 11(a-d))

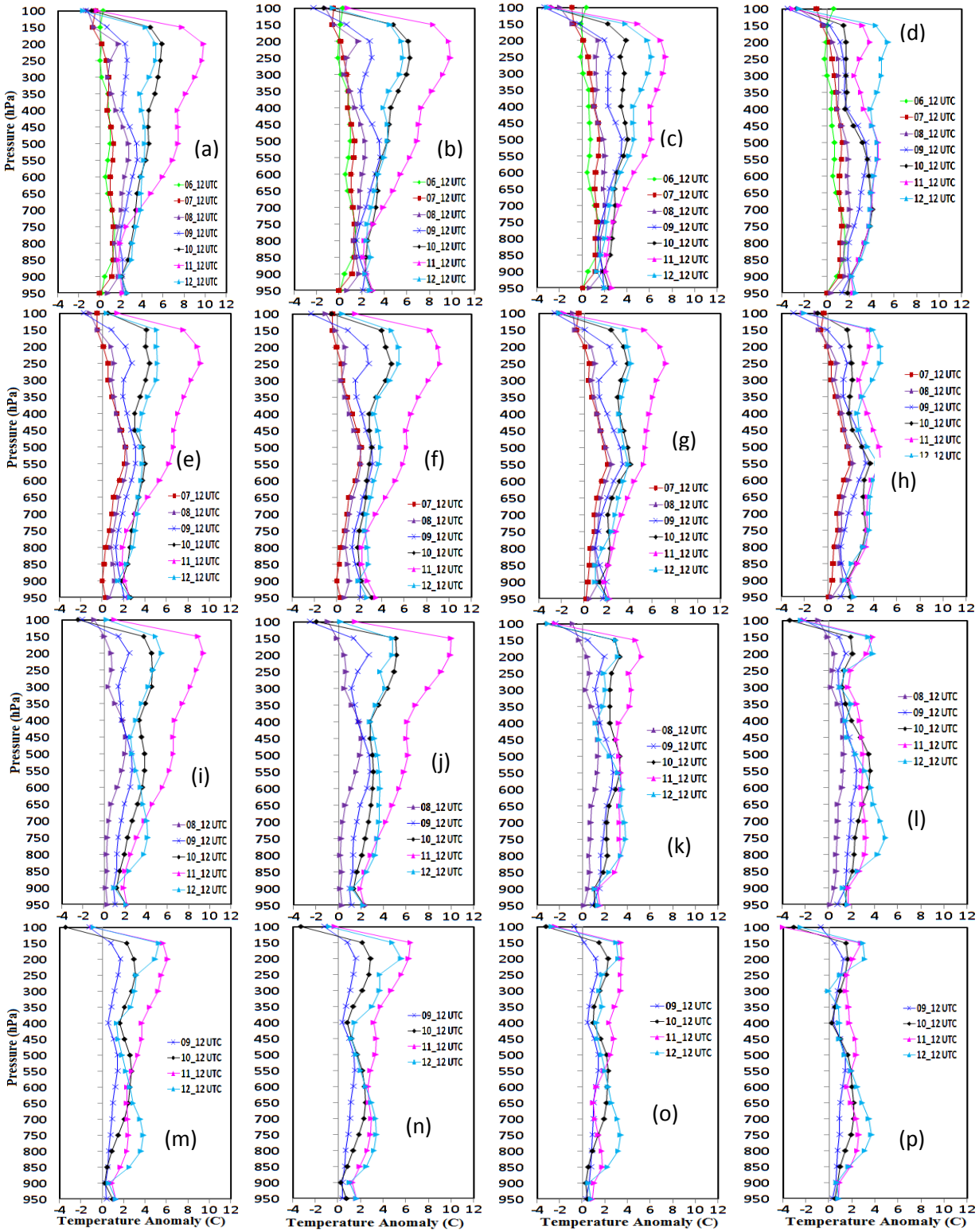

Figure 11: Model simulated vertical temperature anomaly at front position of TC Hudhud using different MPs with the initial conditions at 0000 UTC on (a-d)6, (e-h)7, (i-l)8 and (m-p)9October 2014 respectively.

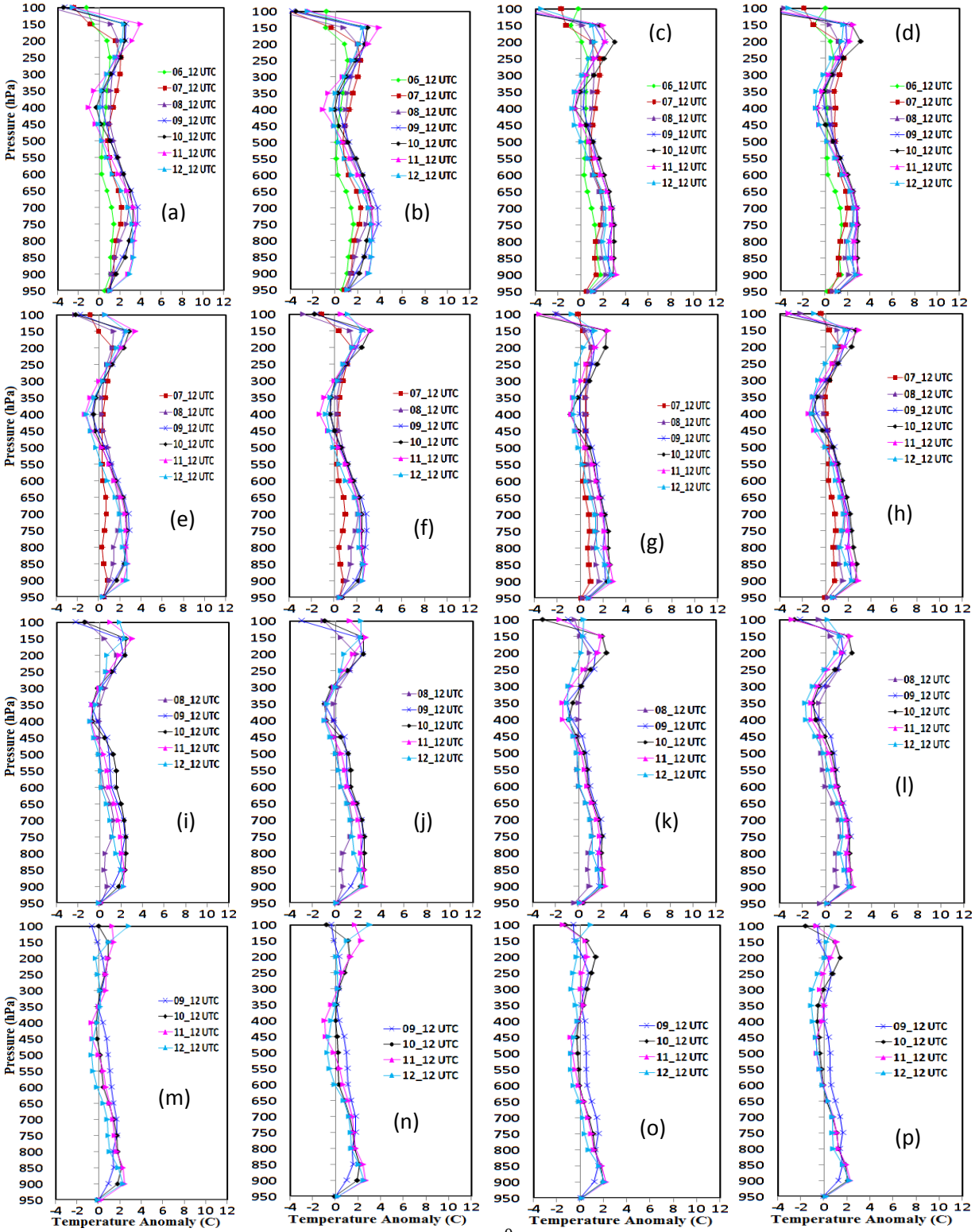

Figure 12: Model simulated vertical temperature (^{0}C) anomaly at rear position of TC Hudhud using four different MPs with the initial conditions at 0000 UTC on (a-d) 6, (e-h) 7, (i-l) 8 and (m-p) 9 October 2014 respectively.

and 7 (Figure 11(e-h)) October. The increase of average temperature is found maximum at 200 hPa for all MPs for all the initial conditions of model run. The simulated area average

maximum temperature is around 10^0C for WSM6 and Thompson schemes, 7^0C for WDM6 and 5^0Cfor NSSL scheme at 200 hPa level. The area average temperature is increased for NSSL scheme at 1200 UTC of 12 October and this increase is maximum at 200 hPa. For the initial conditions at 0000 UTC of 8 (Figure 11(i-l)) and 9 (Figure 11(m-p)) October, the temperature has found to increase for all MPs till on 11 October and then decreased 12 October with little exception for different vertical levels. For 0000 UTC of 8 and 9 October initial conditions increase of temperature is found minimum at 400 hPa level and it is also increased on 12 October below 700 hPa. The area average temperature in the upper level is significantly higher on 11 October except NSSL scheme.

The temperature at rear position is found to increase continuously from the initial conditions of model run to 11 October at 750 and 200 hPa level and decrease continuously and found negative at 500-300 hPa level for all initial conditions and for MP schemes (Figures 12(a-p)). The highest temperature anomaly is found at 950-650 hPa with little exception and found to decrease with time gradually for the initial conditions at 0000 UTC of 6, 7, 8 and 9 October for all MPs. The temperature anomaly at front position for all MPs shows increasing tendency till on 11 October then decreasing tendency on 12 October for all initial conditions with little exception at different vertical levels. At rear position, two crests are found, one at 750 hPa and another at 200 hPa and one trough at 400 hPa where the area average temperature continuously is decreased and reached negative for all the initial conditions and for all MP schemes.

4.1.9 Wind Speed (WS) at different pressure level

The wind speed forecasts for the TC Hudhud using four different MPs are presented in Figure 13(a-p) with the initial conditions at 0000 UTC of 6, 7, 8 and 9 October 2014. The distribution pattern of wind speed is almost similar at 0000 UTC and 1200 UTC so that only 1200 UTC graphs are presented. The area average wind speed is almost constant for all MPs during 6-8 October from 950 to 250 hPa level (Figure 13(a-d)) and after that it is increased significantly during 8-11 October as the cyclone moves towards the front and is decreased on 12 October except NSSL scheme by which the wind speed is also increased for the initial conditions at 0000 UTC of 6October. The area average wind speed is increased little at 7 to 8 October for all MPs from 950 to 250 hPa level (Figure 13(e-h)) and after that it is increased significantly during 8-11 October as the cyclone moves towards the front and decreased on 12 October except NSSL scheme by which the wind speed is also increased for the initial

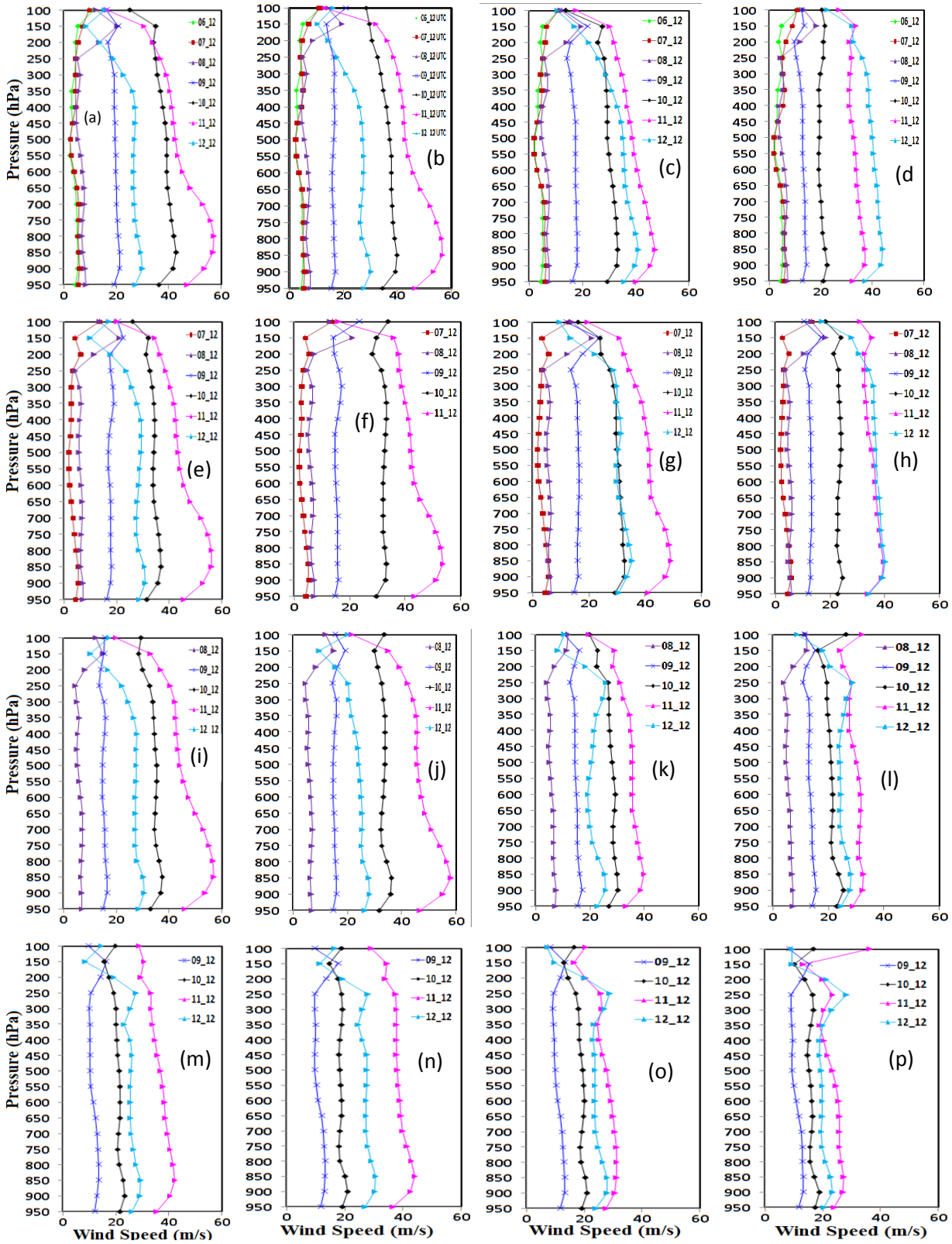

Figure 13: Model simulated area average wind speed at front position of TC Hudhud using four different MPs with the initial conditions at 0000 UTC on (a-d) 6, (e-h) 7, (i-l) 8 and (m-p) 9 October 2014 respectively.

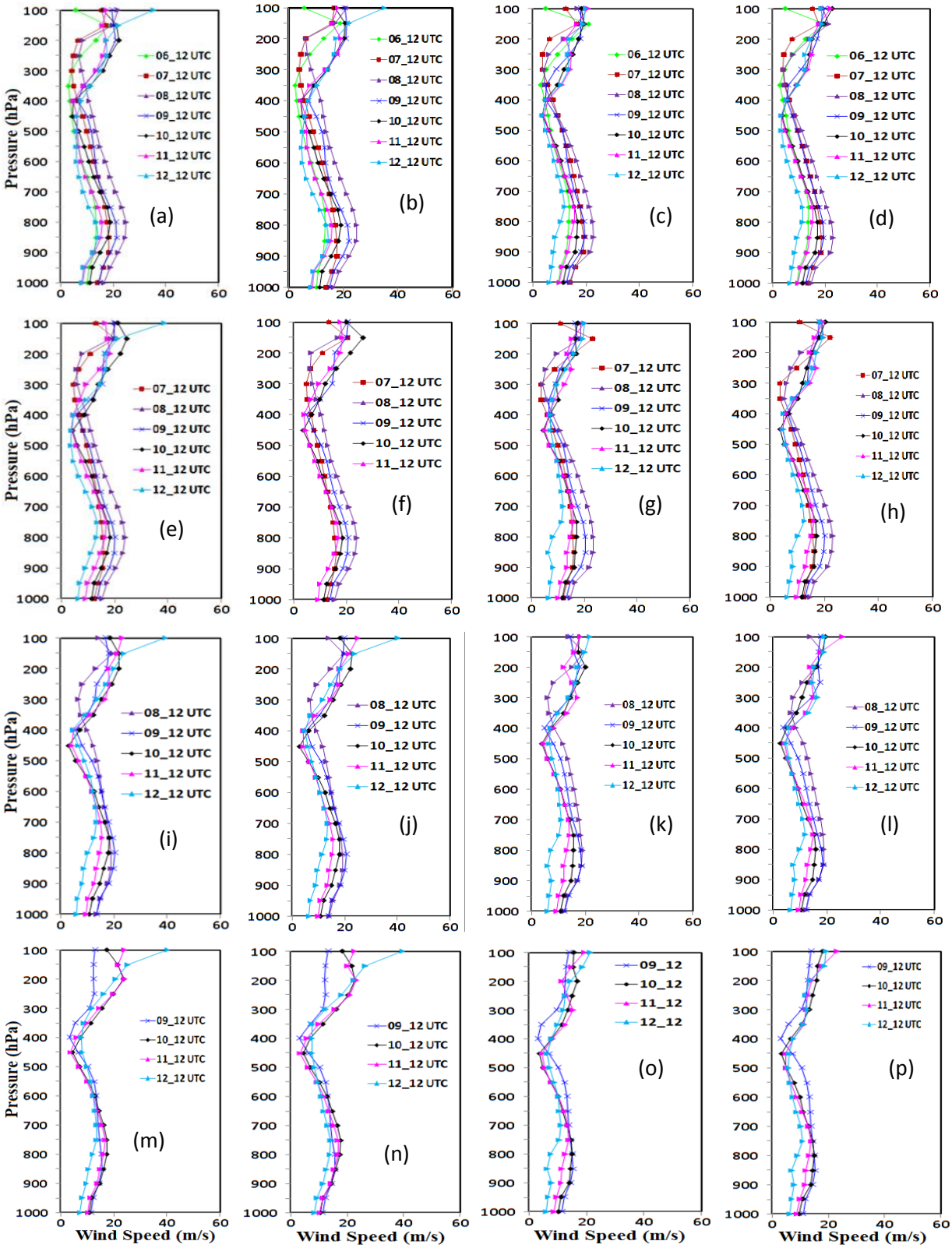

Figure 14: Model simulated area average wind speed at rear position of TC Hudhud using four different MPs coupling with KF scheme with the initial conditions at 0000 UTC on (a-d) 6, (e-h) 7, (i-l) 8 and (m-p) 9 October 2014 respectively.

conditions at 0000 UTC of 7October. The area average wind speed is found to increase significantly for all MPs from 950 to 250 hPa level as shown in Figure 13(i-l) during 8-11 October as the cyclone moves towards the front and is found to decrease on 12 October for the initial conditions at 0000 UTC of 8 October. The area average wind speed is found to increase significantly for all MPs from 950 to 250 hPa level (Figure 13(m-p)) during 9-11 October as the cyclone moves towards front and decreased on 12 October for the initial conditions at 0000 UTC of 9October. On 11 October the WS is found significantly higher at 850 hPa for WSM6, Thompson and WDM6 schemes for the initial conditions at 0000 UTC of 6, 7 and 8October.

The area average wind speed at rear position is found to increase for WSM6, Thompson, WDM6 and NSSL schemes up to 8 October and decreased during 9-12 October for the initial conditions at 0000 UTC of 6 (Figure 14(a-d)), 7 (Figure 14(e-h)), 8 (Figure 14(i-l)) and 9 (Figure 14(m-p)) October. The area average wind speed is found maximum at 850 hPa level and minimum at 400 hPa level at rear position for all MPs for all different initial conditions. The area average WS is found to increase at front position from 950 to 250 hPa levels for all MPs before crossing the cyclone over land and after crossing over land the WS is found to decrease on 1200 UTC of 12 October for all initial conditions. The area average WS is found to decrease at rear position from 950 to 450 hPa levels for all MPs during 8 to 12 October for all initial conditions.

4.1.12 Wind Direction (WD)

Model simulated vertical variations of area average WD at front position for four different MPs are presented in Figures 15(a-p) for the initial conditions at 0000 UTC of 6, 7, 8 and 9 October 2014. The distribution pattern of WD for all MPs with different initial conditions at 0000 UTC and 1200 UTC are almost similar and only the graphs at 1200 UTC so that only 1200 UTC graphs are presented.

It is observed from the simulated results that the easterly wind is flowing from surface to 600 hPa levels and westerly winds from 500 to 250 hPa level (Figure 15(a-d)) on 6-7 October 2014 for all MPs except NSSL scheme with the initial conditions at 0000 UTC of 6 October. During 8-10 October, the northeasterly to easterly wind flow is continuing and during 11-12 October the wind flow is shifted from northeasterly to southerly from surface to 100 hPa levels for all MPs with the 0000 UTC of 6 October initial conditions. Due to the northeasterly to easterly flow during 8-10 October at front position the TC moved towards west

southwestward i.e. the eastern coast of India and due to the southerly flow from surface to 100 hPa levels on 11 October it shifted towards north and crossed eastern coast of Indian.

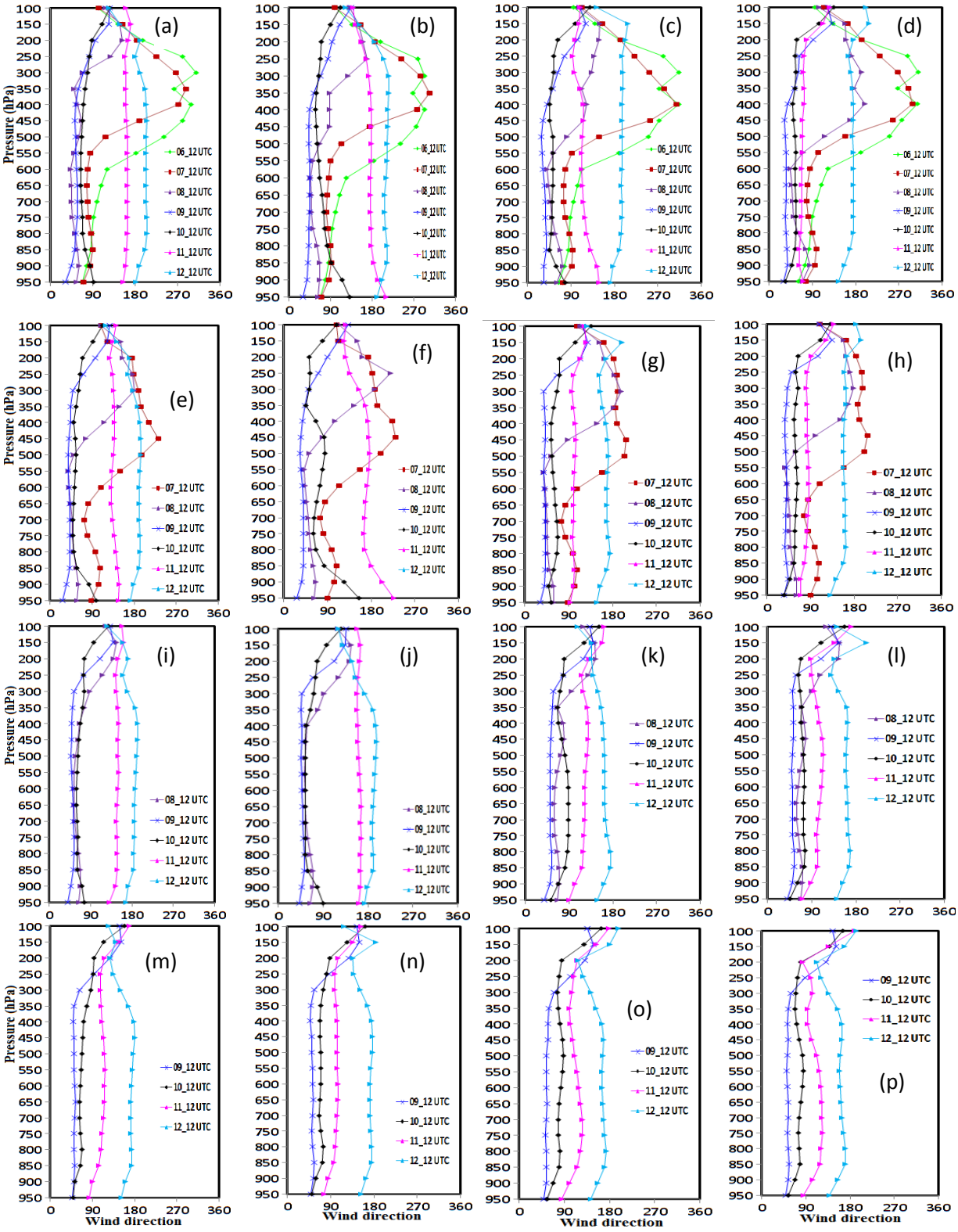

Figure 15: Model simulated area average wind direction at 1200 UTC of different days at front position of TC Hudhud for four different MPs on (a-d) 6, (e-h) 7, (i-l) 8 and (m-p) 9 October 0000 UTC initial conditions respectively.

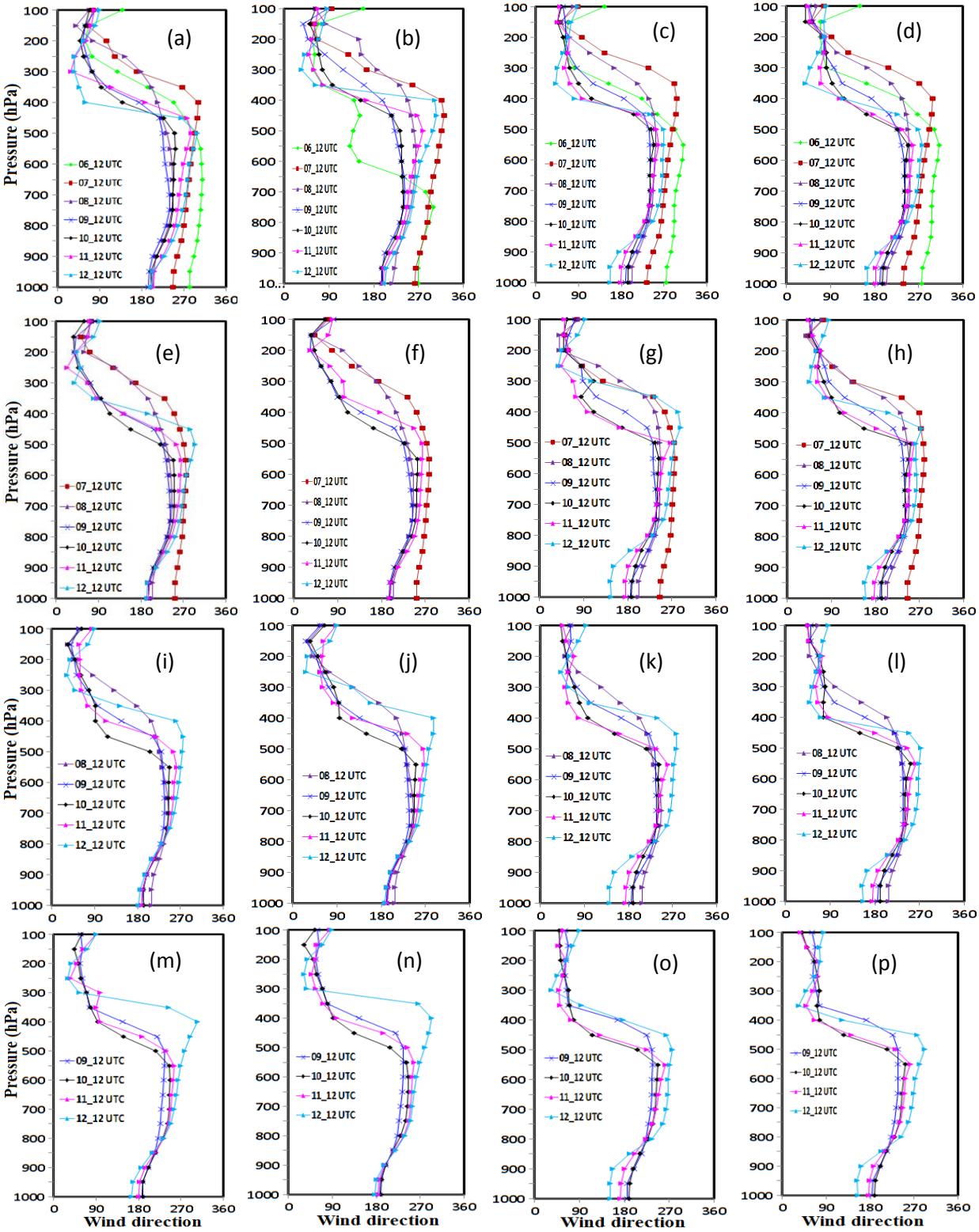

Figure 16: Model simulated area average wind direction at 1200 UTC of different days in rear position of TC Hudhud for four different MPs on (a-d) 6, (e-h) 7, (i-l) 8 and (m-p) 9 October 0000 UTC initial conditions respectively.

It is observed from the simulated results that the easterly wind is flowing from surface to 600 hPa levels and southerly to southwesterly winds from 500 to 250 hPa level (Figure 15(e-h))

on 7 October 2014 for all MPs with the 0000 UTC of 7 October initial conditions. On 8 October, the northeasterly wind is flowing from surface to 500 hPa and southerly to southeasterly wind from 450 to 200 hPa levels for all MPs with the 0000 UTC of 7 October initial conditions. During 9-10 October the northeasterly to easterly wind flow is continuing and during 11-12 October the wind flow are shifted to south-southeasterly from surface to 100 hPa levels for all MPs with the 0000 UTC of 7 October initial conditions. Due to the northeasterly to easterly flow during 9-10 October and easterly to southeasterly flow on 11 October the TC Hudhud moved towards eastern coast of India.

The northeasterly wind is flowing from surface to 200 hPa levels on 8-10 (Figure 15(i-l)) and 9-10 (Figure 15(m-p)) October 2014 for all MPs with the 0000 UTC of 8 and 9 October initial conditions. On 11 and 12 October the south-southeasterly and almost southerly wind is flowing from surface to 200 hPa levels for all MPs with the 0000 UTC of 8 and 9 October initial conditions. Due to the northeasterly to easterly flow during 8-10 October and southeasterly flow on 11 October the TC Hudhud moved towards west northwestern direction.

It is observed from the model simulated results that at rear position the area average wind is flowing southerly from surface to 850 hPa, westerly to southwesterly from 800 to 450 hPa and easterly wind from 450 to 100 hPa levels for all MPs for the initial conditions at 0000 UTC of 6 (Figure 16(a-d)), 7 (Figure 16(e-h)), 8 (Figure 16(i-l)) and 9 (Figure 16(m-p)) October 2014.

4.1.10 Convective Available Potential Energy (CAPE)

Model simulated vertical variations of area average CAPE at front position with four different MPs are presented in Figures 17(a-p) for 0000 UTC on 6, 7, 8 and 9 October 2014 initial conditions. It is found from Figure 19(a-p) that the CAPE is decreased continuously from 950 to 800 hPa for all combination of MPs with different initial conditions. The CAPE is found to be zero from 800 to 100 hPa level, that's why the value of CAPE has been plotted up to 800 hPa. The distribution patterns of CAPE at 0000 UTC and 1200 UTC are almost similar so that only 1200 UTC graphs are presented.

The area average CAPE is found to decrease for WSM6, Thompson, WDM6 and NSSL schemes during 6-9 October (Figure 17(a-d)) and increase on 10 and decrease again up to 12 October with little exception for the initial conditions of 0000 UTC of 6 October. The area average CAPE is found to decrease for all MP schemes during 7-9 October (Figure 17(e-h)) and increase on 10 and decrease again on 11 October with little exception for the initial conditions of 0000 UTC of 7 October.

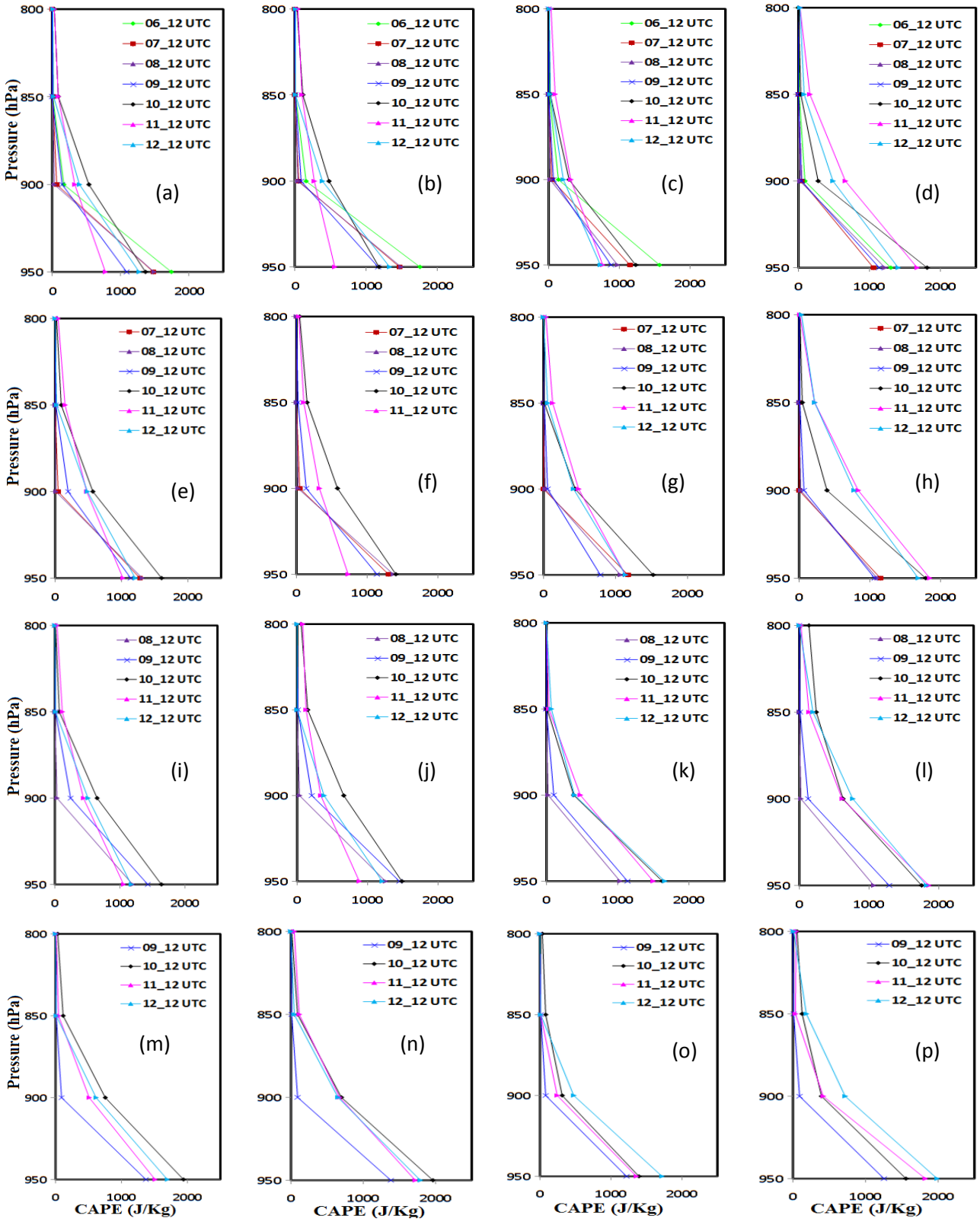

Figure 17: Vertical variation of CAPE simulated area average CAPE at 1200 UTC of different days at front position of TC Hudhud using four different MPs with the initial conditions at 0000 UTC on (a-d) 6, (e-h) 7, (i-l) 8 and (m-p) 9 October 2014 respectively.

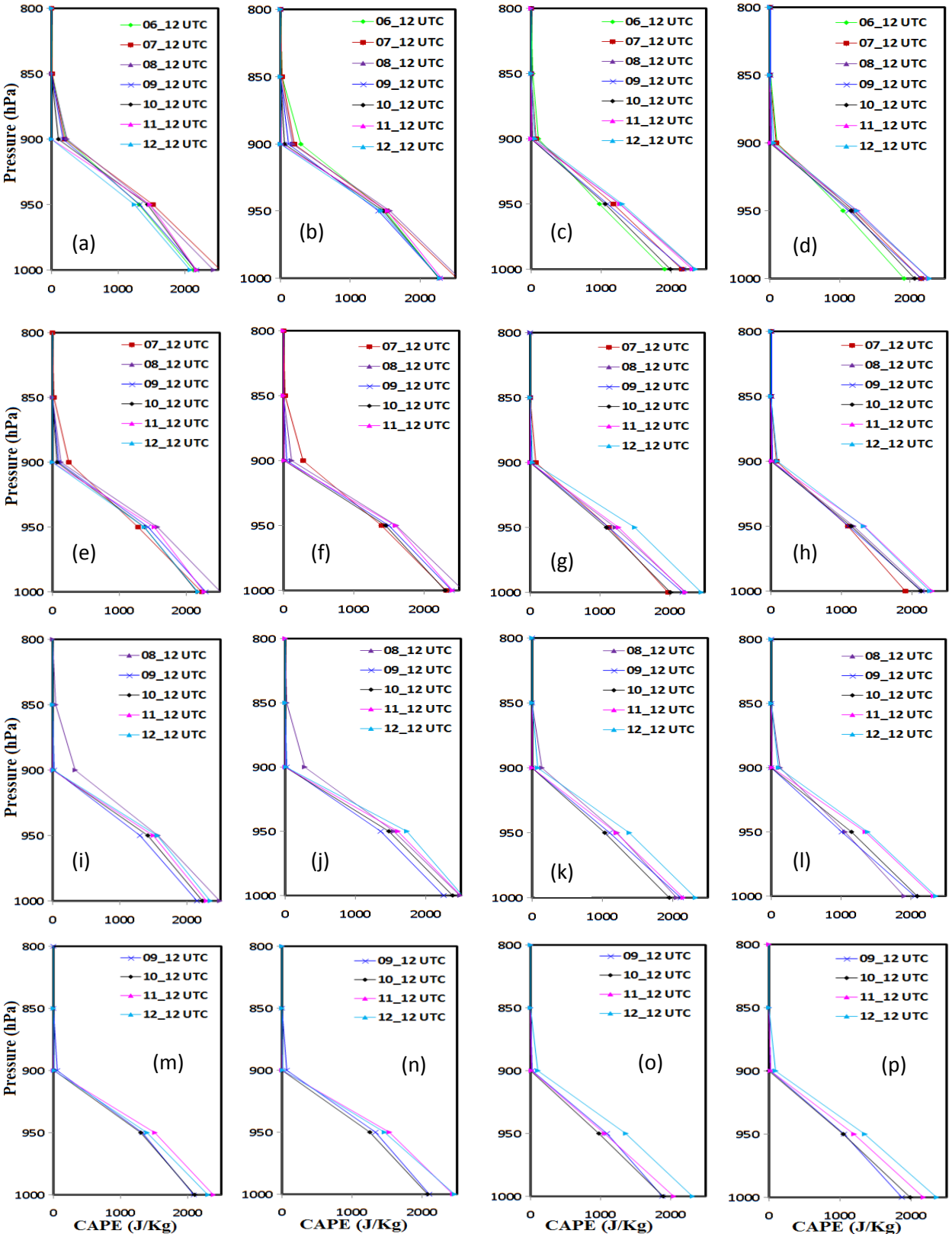

Figure 18: Model simulated area average CAPE at 1200 UTC of different days at rear position of TC Hudhud using four different MPs with the initial conditions at 0000 UTC on (a-d) 6, (e-h) 7, (i-l) 8 and (m-p) 9 October 2014 respectively.

The area average CAPE is found to increase for WSM6, Thompson, WDM6 and NSSL schemes during 8-10 October (Figure 17(i-l)) and has decreased on11 October and increase again on 12 October except NSSL for the initial conditions of 0000 UTC of 8 October. The area average CAPE is found to increase for WSM6, Thompson, WDM6 and NSSL schemes during 9-10 October (Figure 17(m-p)) and has decreased on11 October with little exception and increase again on 12 October for the initial conditions of 0000 UTC of 9 October.

Model simulated vertical variation of area average CAPE at the rear position with four different MPs are presented in Figs 18(a-p) for 0000 UTC of 6, 7, 8 and 9 October 2014 initial conditions. The CAPE is found to be zero from 850 to 100 hPa level, that's why the value of CAPE has been plotted up to 800 hPa. The distribution patterns of CAPE at 0000 UTC and 1200 UTC are almost similar so that only 1200 UTC graphs are presented. It is found from Figures 18(a-h) that the CAPE has increased for all combination of MPs from 1000 to 900 hPa up to 8 October then decrease on 9 and increased again till on 11 October with little exception for the initial conditions of 0000 UTC of 6 and 7 October. The area average CAPE is found to increase from 9 to 12 October (Figure 18(i-l)) for the initial conditions of 0000 UTC of 8 October. The area average CAPE is found to decrease for all schemes during 9-10 October (Figure 18(m-p)) and increase till 12 October with little exception for the initial conditions of 0000 UTC of 9 October.

4.1.11 Convective Inhibition (CIN)

Model simulated area average CIN at front position with four different MPs for 0000 UTC of 6, 7, 8 and 9 October 2014 initial conditions are presented in Figs 21(a-p). It is found from Figures 19(a-p) that the CIN is increased from 950 to 900 hPa after that it is decreased and reaches near zero at 800 hPa. That's why the value of CIN has been plotted up to 800 hPa. Maximum CIN is simulated at 900 hPa for all MPs with different initial conditions. The changing pattern of CIN at 0000 UTC and 1200 UTC are almost similar so that only 1200 UTC graphs are presented.

The area average CIN is found to decrease for WSM6 and NSSL schemes during 6-8 October (Figure 19(a-d)) then it increased during 9-12 October with little exception.CIN has increased during 6-7 October and increase during 8-9 October for Thompson and WDM6.The vertical distribution pattern also suggests that the CIN finally decreased during 10 to 12 October for the initial conditions of 0000 UTC of 6 October. The area average CIN is found to increase for all MP schemes during 7-10 October (Figure 19(e-h)) and decreased on

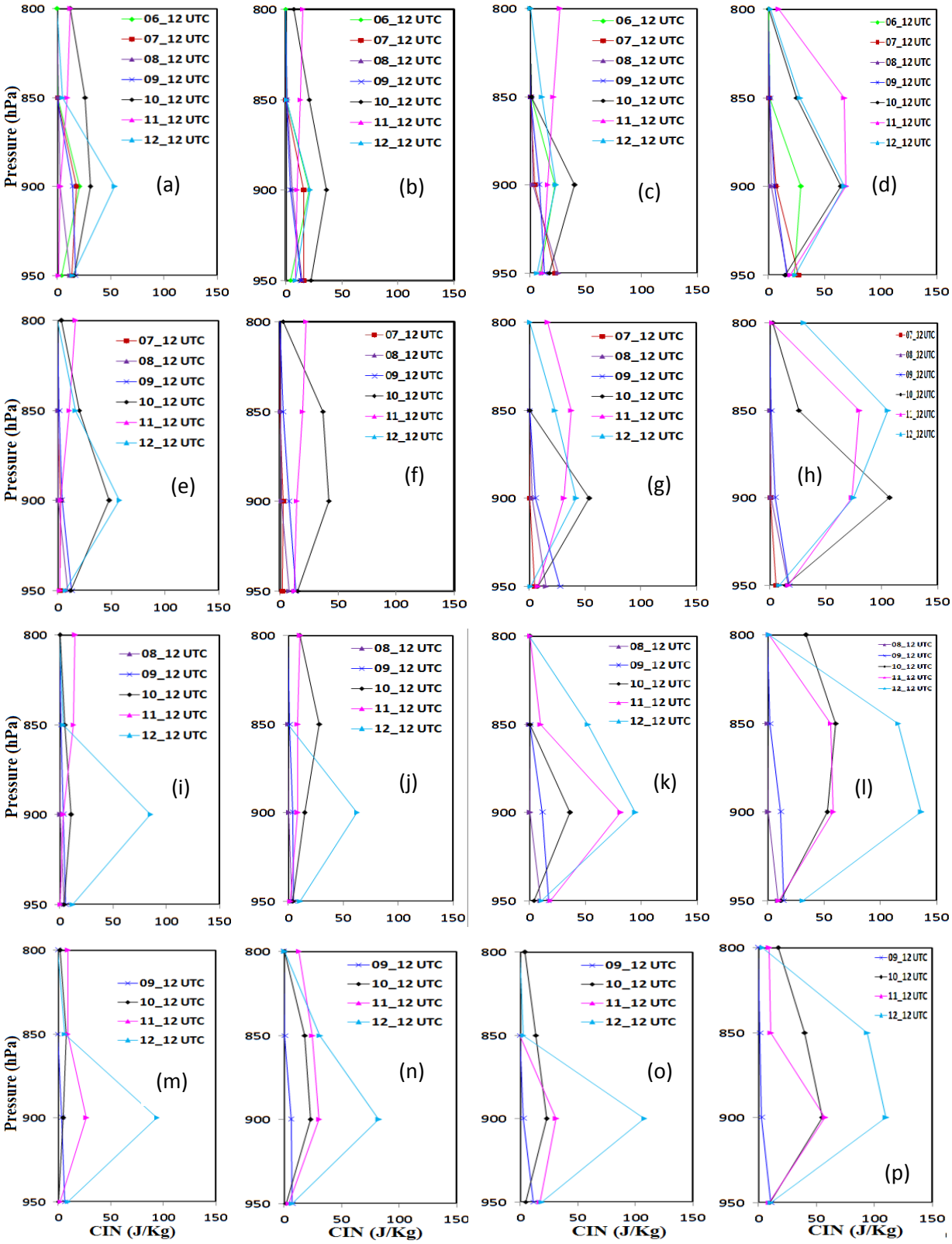

Figure 19: Model simulated area average CIN at 1200 UTC of different days at front position of TC Hudhud for four different MPs on (a-d) 6, (e-h) 7, (i-l) 8 and (m-p) 9 October 0000 UTC initial conditions respectively.

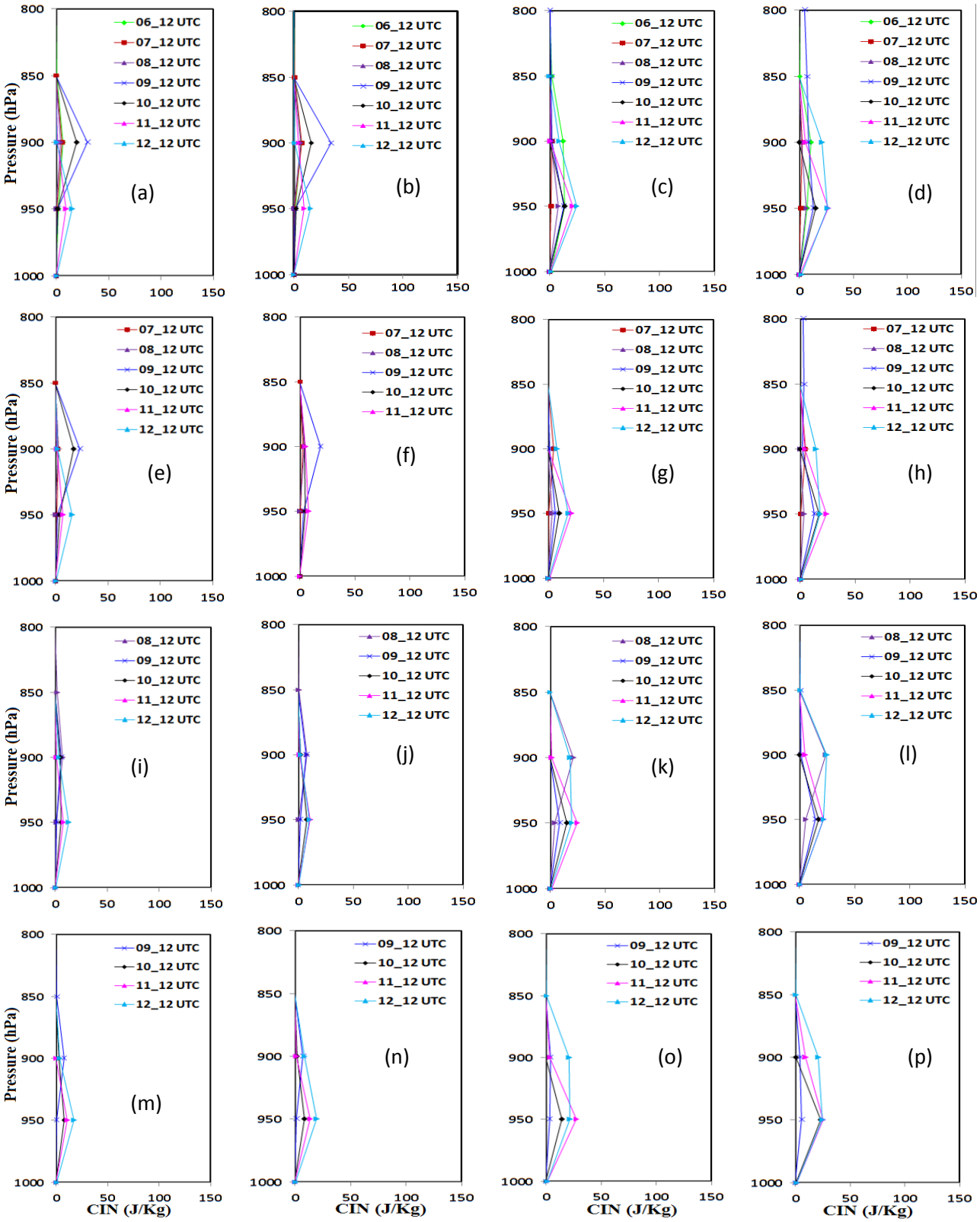

Figure 20: Model simulated area average CIN at 1200 UTC of different days at rear position of TC Hudhud for four different MPs on (a-d) 6, (e-h) 7, (i-l) 8 and (m-p) 9 October 0000 UTC initial conditions respectively.

The area average CIN is found to increase for WSM6 and Thompson schemes during 8-10 October (Figure 19(i-l)) then decrease on 11 October after that it again increased on 12 October while WDM6 and NSSL has increased on 8 up to 12 October for the initial conditions of 0000 UTC of 8 October. The area average CIN is found to increase for WSM6, Thompson, WDM6 and NSSL schemes during 9-12 October (Figure 19(m-p)) with little exception for the initial conditions of 0000 UTC of 9 October.

The area average CIN at the rear position is simulated zero at the surface for all MPs for all the initial conditions and are presented in Figure 20(a-p). Little amount of CIN is seen at 900 hPa level for WSM6 and Thompson schemes during 6-10 (Figure 20(a-b)) and 7-10 (Figure 20(e-f)) October and at 950 hPa during 11-12 October for the initial conditions at 0000 UTC of 6 and 7 October. The CIN has increased at 950 hPa level for WDM6 and NSSL schemes during 6-10 (Figure 20(c-d)) and 7-10 (Figure 20(g-h)) October for the initial conditions at 0000 UTC of 6 and 7 October. The area average CIN has found to increase for all MP schemes during 8-12 October (Figure 20(i-l)) and 9-12 October (Figure 20(m-p)) with little exception of WDM6 scheme for the initial conditions of 0000 UTC of 8 and 9 October.

4.2 Tropical Cyclone Mora

4.2.1 Synoptic situation of Tropical Cyclone Mora

The tropical cyclone 'Mora' developed from a low pressure area which lay over southeast BoB and adjoining areas of central BoB at 0300 UTC of 25 May 2017. It is persisted over the same region on 26 and seen as a well-marked low pressure area at 0300UTC of 27 over east central and adjoining west central and southeast BoB. It moved northeastwards and intensified into a depression (D) over east central BoB at 0000 UTC of 28May. Continuing its northeastwards movement, it further intensified into a deep depression (DD) at 0900 UTC and into a cyclonic storm (CS) "MORA" over east central BoB at 1800UTC of 28May. Thereafter, it moved north-northeastwards and further intensified into a severe cyclonic storm (SCS) at 1200 UTC of 29. The system reached its peak intensity 30-33 ms^{-1}(110-120kph) at 2100 UTC of 29 May. It continued to move nearly north-northeastwards and crossed Bangladesh coast close to south of Chittagong in between 0400 and 0500 UTC of 30 May. After landfall, the system weakened into a CS at 0900 UTC of 30 May, into a DD at 1200UTC and depression at 1800 UTC on that day.

4.2.2 Minimum Sea Level Pressure (SLP)

The model simulated SLP of TC Mora using different MP schemes coupling with KF scheme with four different initial conditions at 0000 UTC of 25, 26, 27 and 28 May 2017 are presented in Figure 21(a-d). The model simulated SLP value for Thompson, WSM6, WDM6 and NSSL schemes are 915, 917, 920 and 950 hPa (Figure 21a), 921, 922, 924 and 926 hPa (Figure 21b), 932, 941, 944 and 948 hPa (Figure 21c) and 929, 930, 938 and 941 hPa (Figure 21d) for the initial conditions at 0000 UTC of 25, 26, 27 and 28 May respectively. The model simulated pressure fall for different MPs with different initial conditions are significantly higher than that estimated central pressure of IMD observed (978 hPa).

The simulated SLP at front position of TC Mora for different initial conditions and for different MPs schemes are displayed in Figure 22(a-d). The simulated SLP values are 915, 917, 920 and 950 hPa (Figure 2a) at 1200, 1800, 1800 UTC of 29 May and 1500 UTC of 30 May for Thompson, WSM6, WDM6 and NSSL schemes respectively with the initial conditions at 0000 UTC of 25 May. The sharp fall of SLP has found for WSM6, Thompson and WDM6 schemes much earlier than observed. For the initial conditions of 0000 UTC of 26 May the SLP at front position are 922& 922 hPa at 0000 and 0600 UTC of 30 May for WSM6 and NSSL schemes, 926 and 926 hPa (Figure 22b) at 2100 UTC of 29 May for

WDM6 &Thompson schemes respectively. The SLP values are found 933, 941, 944 and 951 hPa (Figure 22c) at 0300, 0900, 1200 and 0600 UTC of 30 May for WSM6, WDM6, NSSL and Thompson schemes respectively for the initial conditions at 0000 UTC of 27 May. For the initial conditions at 0000 UTC of 28 May the SLP has simulated at front position of the cyclone 927, 938, 942 and 930 hPa (Figure 22d) at 2100, 2100 and 1800 UTC of 29 May and 0300 UTC of 30 for Thompson, WDM6, WSM6 and NSSL schemes respectively.

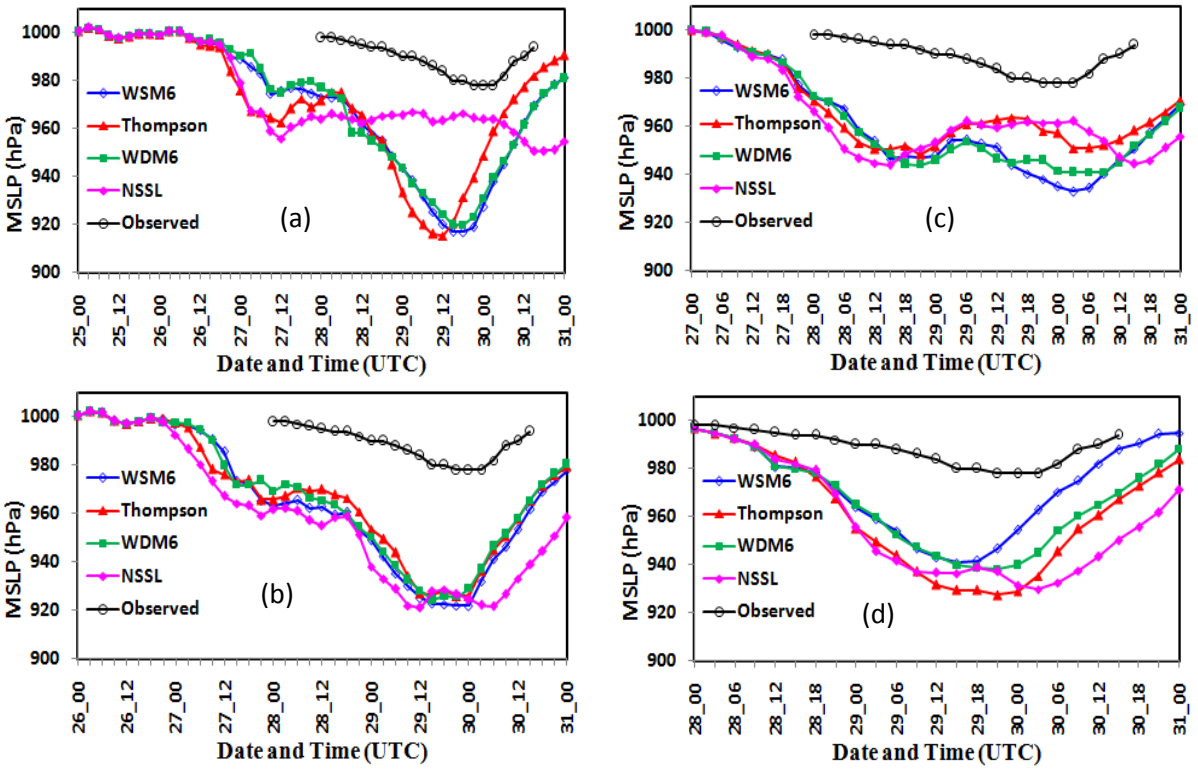

Figure 21: Model simulated SLP of TC Mora using four different MP schemes with the initial conditions at 0000 UTC on (a) 25 May, (b) 26 May, (c) 27 May and (d) 28 May 2017 respectively.

The model simulated SLP at the rear position of TC Mora for different MPs schemes with different initial conditions are presented in Figure 22(e-h).The simulated SLP values at rear position is 1000 hPa for the initial conditions at 0000 UTC of 25 May (Figure 22e) and 1001, 1001, 1001 and 1000 hPa for the initial conditions at 0000 UTC of 26 May (Figure 22f) for WSM6, Thompson, WDM6 and NSSL schemes respectively. The simulated MSLP at rear position are found 1001 hPa for the initial conditions at 0000 UTC of 27 May (Figure 2g) and 1002 hPa for the initial conditions at 0000 UTC of 28 May (Figure 22h) for Thompson, NSSL, WDM6 and WSM6 schemes respectively. SLP at front position for all MPs has fallen more than the IMD estimated for all initial conditions. The time to reach SLP minimum for

all MPs is almost similar to that of IMD estimated. At rear position SLP is almost constant all MPs. From the above discussion NSSL and WDM6 schemes the better performance.

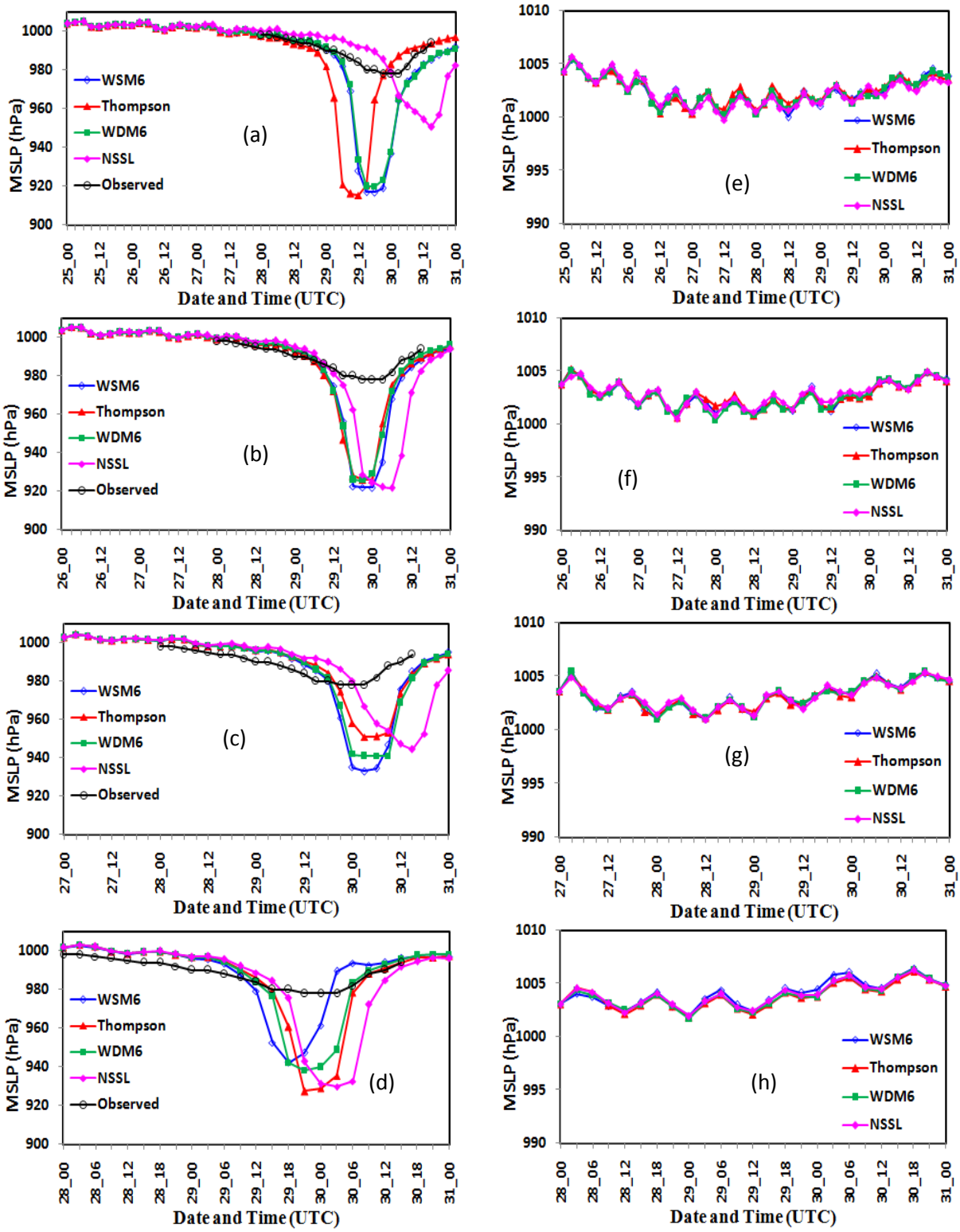

Figure 22: Model simulated MSLP at (figure 22(a-d)) front and (figure 22 (e-h)) rear position of TC Mora using four different MP schemes with the initial conditions at 0000 UTC on 25, 26, 27 and 28 May 2017 respectively.

4.2.3 Maximum Wind Speed (MWS) at 10 m level

The model simulated MWSs using different MP schemes coupling with KF scheme with four different initial conditions at 0000 UTC of 25, 26, 27 and 28 May 2017 are presented in Figure 23(a-d). The MWS (Figure 23a) of 52, 51, 50 and 45 ms^{-1} are simulated at 2100, 1500, 0900 and 1200 UTC of 29 May for WSM6, WDM6, Thompson and NSSL schemes for the initial conditions at 0000 UTC of 25 May respectively. The MWSs of 52, 51 and 50 are simulated at 1200 and 49 ms^{-1} (Figure 23b) at 2100 UTC of 29 May for Thompson, NSSL, WSM6 and WDM6 schemes for the initial conditions at 0000 UTC of 26 May respectively. For the initial conditions at 0000 UTC of 27 (Figure 23c) May the MWSs is 50, 49, 47 and 47 ms^{-1} are simulated at 1800, 0000, 0000 UTC of 29 May and 0300 UTC of 30 May for WDM6, WSM6, NSSL and Thompson schemes respectively. The MWSs (Figure 23d) are 51, 50 and 49 ms^{-1} at 1500 UTC and 46 ms^{-1} at 1200 UTC of 29 May for NSSL, Thompson, WDM6, and WSM6 schemes respectively for the initial conditions at 0000 UTC of 28 May.

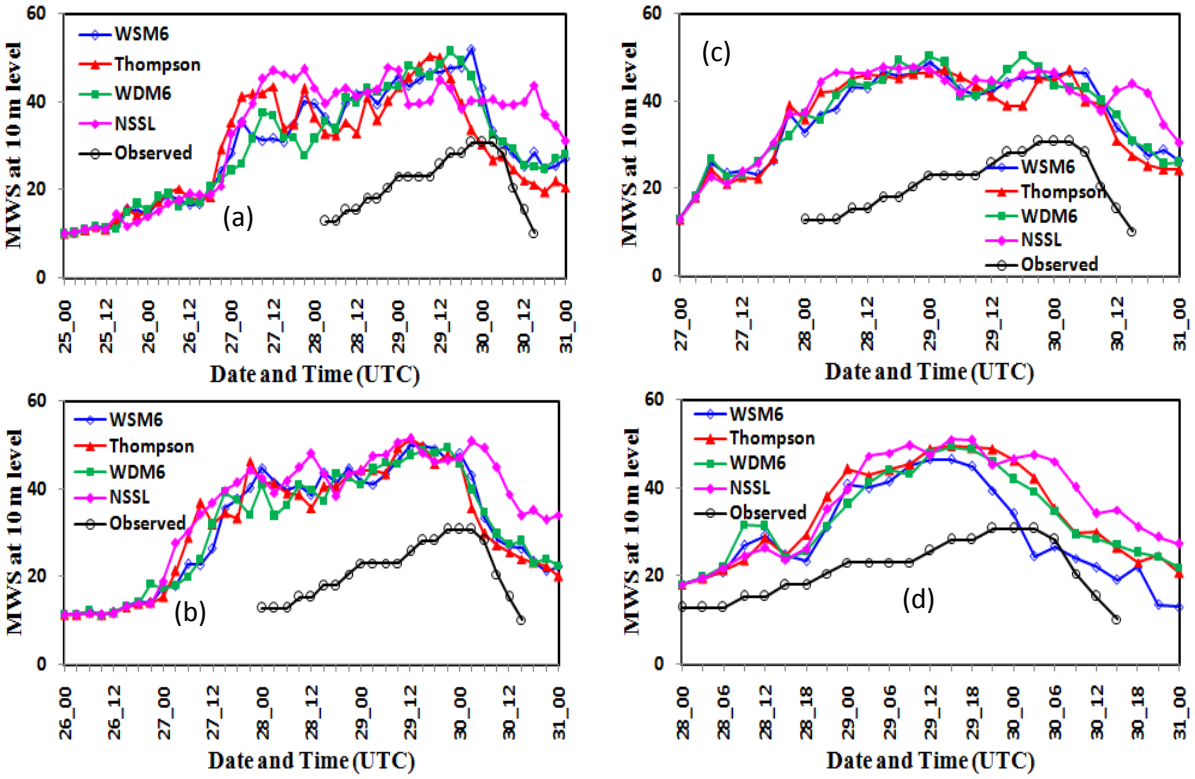

Figure 23: Model simulated MWS at 10m level of TC Mora using four different MPs with the initial conditions at 0000 UTC of (a) 25 May, (b) 26 May, (c) 27 May and (d) 28 May 2017 respectively.

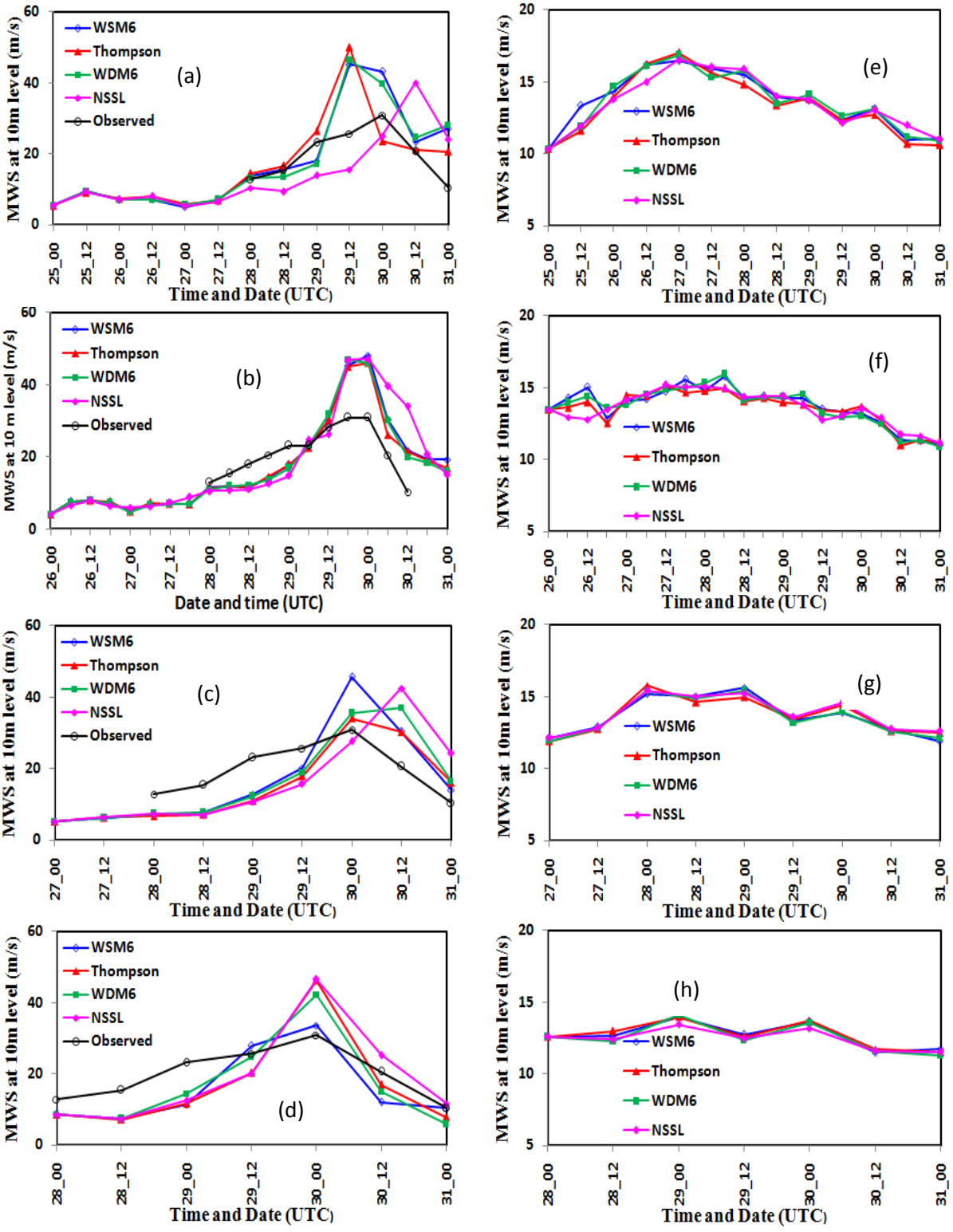

Figure 24: Model simulated MWS at 10 m level of TC Mora at (a-d) front and (e-h) rear position using four different MP schemes with the initial conditions at 0000 UTC on (a) 25 May, (b) 26 May, (c) 27 May and (d) 28 May 2017 respectively

The MWSs at 10m level in front position of the cyclone are 50, 46 and 45 ms^{-1} at 1200 UTC of 29 May for Thompson, WDM6 and WSM6 schemes and 39 ms^{-1} at 1200 UTC of 30 May

for NSSL schemes ((Figure 24a)) respectively for the initial conditions at 0000 UTC of 25 May. The MWSs are found 48, 47, 46, and 46 ms^{-1} at 0000 UTC of 30 May for WSM6, NSSL, Thompson and WDM6 schemes respectively for the initial conditions at 0000 UTC of 26 May ((Figure 24b)) respectively. The simulated MWSs are 46, 42, 37 and 34 ms^{-1} at 0000, 1200, 1200 and 0000 UTC of 30 May ((Figure 24c)) and 33, 47, 42 and 46 m s^{-1} at 0000 UTC of 30 May ((Figure 24d)) for WSM6, NSSL, WDM6 and Thompson schemes with the initial conditions at 0000 UTC of 27 and 28 May respectively.

The MWSs at rear position are found 17, 17, 17, 16 ms^{-1} (Figure 24e) at 0000 UTC of 25 May, 16 & 16 and 15 & 15 ms^{-1} (Figure 24f) at 0600 UTC of 28 and 1200 UTC of 27 May for WSM6, WDM6, Thompson and NSSL schemes with the initial conditions of 0000 UTC of 25 and 26 May respectively. For the initial conditions at 0000 UTC of 27 May the simulated MWSs are 16 & 15 ms^{-1} at 0000 UTC of 28 May and 16 & 15 ms^{-1} (Figure 24g) at 0000 UTC of 29 May and 14, 13, 14 and 14 ms^{-1} (Figure 24h) for Thompson, NSSL, WSM6 and WDM6 schemes respectively. The MWSs at 10m level in rear position of the cyclone are almost constant with the movement of TC towards land.

4.2.4 Track of TC Mora

The model simulated tracks for prediction times of 168, 144, 120 and 96-h and IMD estimated track of TC Mora for different MP schemes are presented in Figure 25(a-d). All the simulations have shown the northward movement of TC Mora with the initial conditions at 0000 UTC of 25, 26, 27 and 28 May. The track forecasts for different sensitivity experiments have shown reasonably accurate prediction. Initially the track is found erratic and after that it moves towards left from observed for all MPs with the initial conditions at 0000 UTC of 25, 26, 27 and 28 May. WDM6 and NSSL schemes have simulated most deviated track WSM6 and Thompson schemes have simulated less deviated track (Figure 25a) with the initial conditions at 0000 UTC of 25 May 2017. For the initial conditions of 0000 UTC of 26 May 2017 (Figure 25b), WDM6 and WSM6 schemes have simulated most deviated track and Thompson and NSSL schemes have simulated less deviated track. The simulated track shifted towards right for all MPs for different initial conditions of model run but still it also propagated towards left of the observed track for the initial conditions at 0000 UTC of 25, 26 27 and 28 (Figure 25d) May. The landfall times are 0200, 0800, 0900 and 0000 UTC of 30 May for WSM6, Thompson, WDM6 and NSSL schemes respectively with the initial conditions at 0000 UTC of 28 May. WSM6 scheme gives the better results for the initial conditions at 0000 UTC of 25, 26, 27 and 28 May initial conditions.

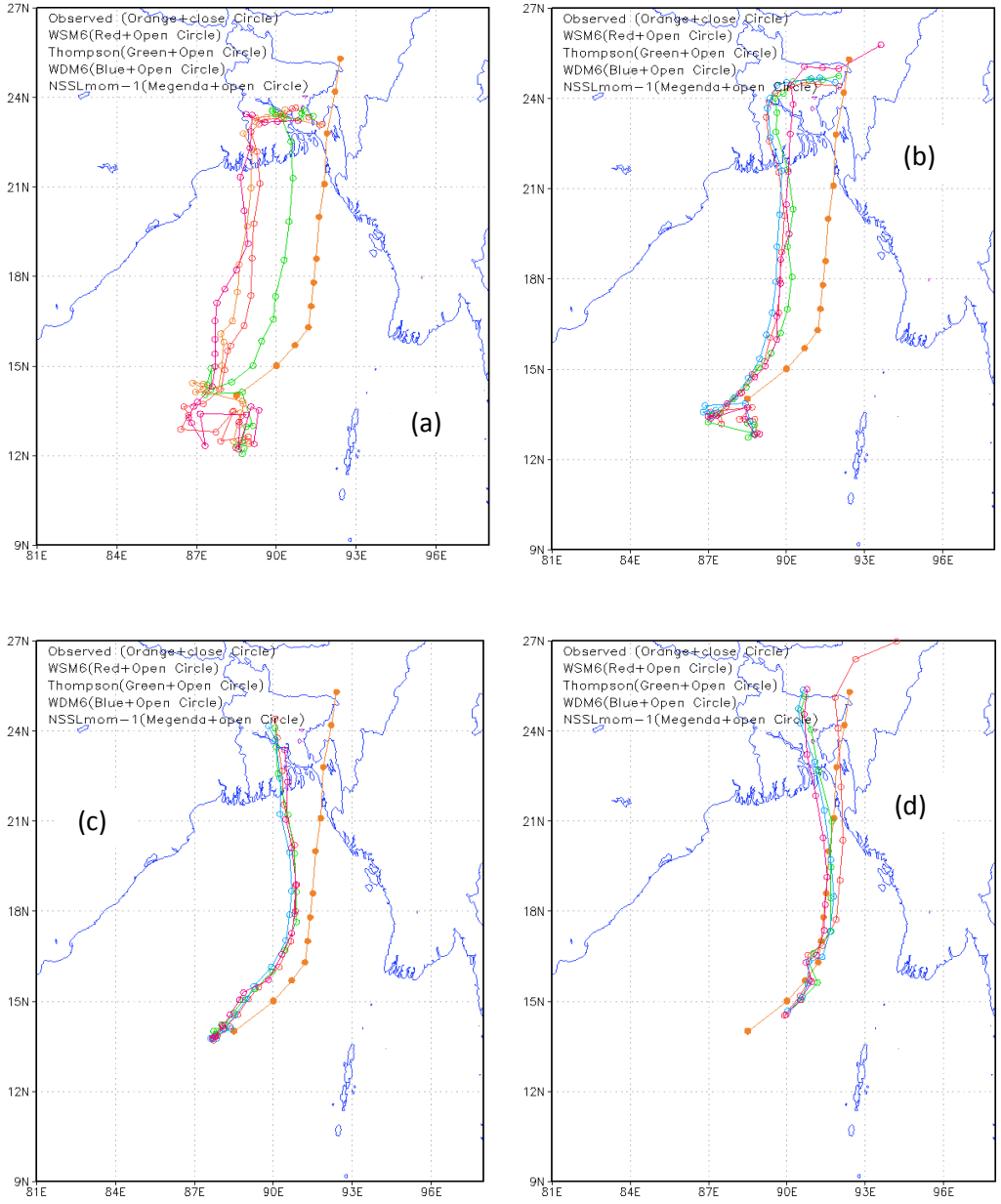

Figure 25: Model simulated and observed tracks of TC Mora using four different MP schemes with the initial conditions at 0000 UTC on (a) 25, (b) 26, (c) 27 and (d) 28 May 2017 respectively.

4.2.5 Specific Humidity (SH)

Vertical variations of model simulated area average SH at the front position with four different MPs and for the initial conditions at 0000 UTC of 25, 26, 27 and 28 May 2017 are presented in Figures 26(a-p). Maximum SH is found at 900 hPa level. The distribution pattern of SH at 0000 UTC and 1200 UTC are almost similar so that only at 1200 UTC are presented.

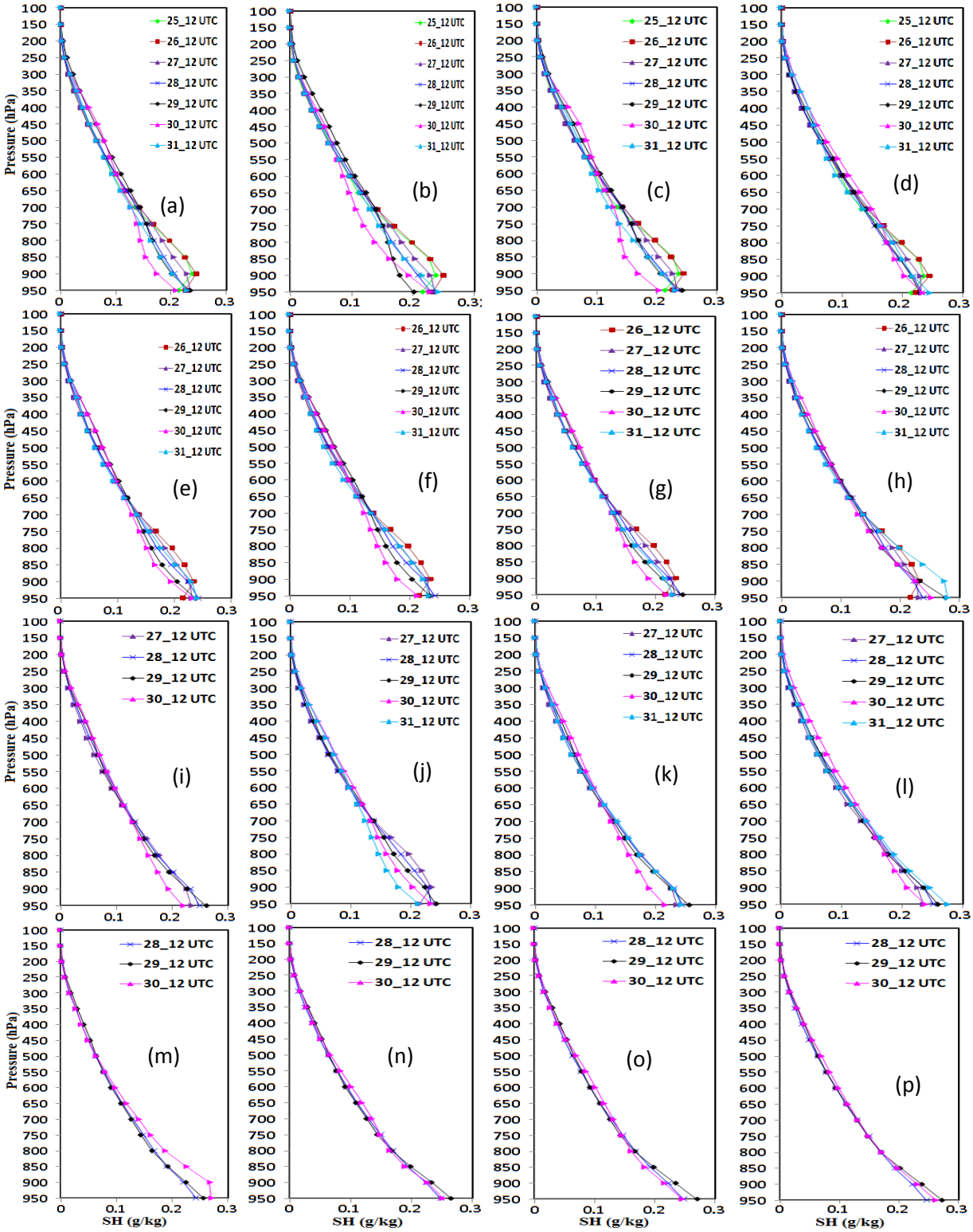

Figure 26: Vertical profiles of Model simulated area average SH (g/kg) at front position of TC Mora at 1200 UTC of different days for four different MPs at 0000 UTC on (a-d) 25 May, (e-h) 26 May, (i-l) 27 May and (m-p) 28 May initial conditions respectively.

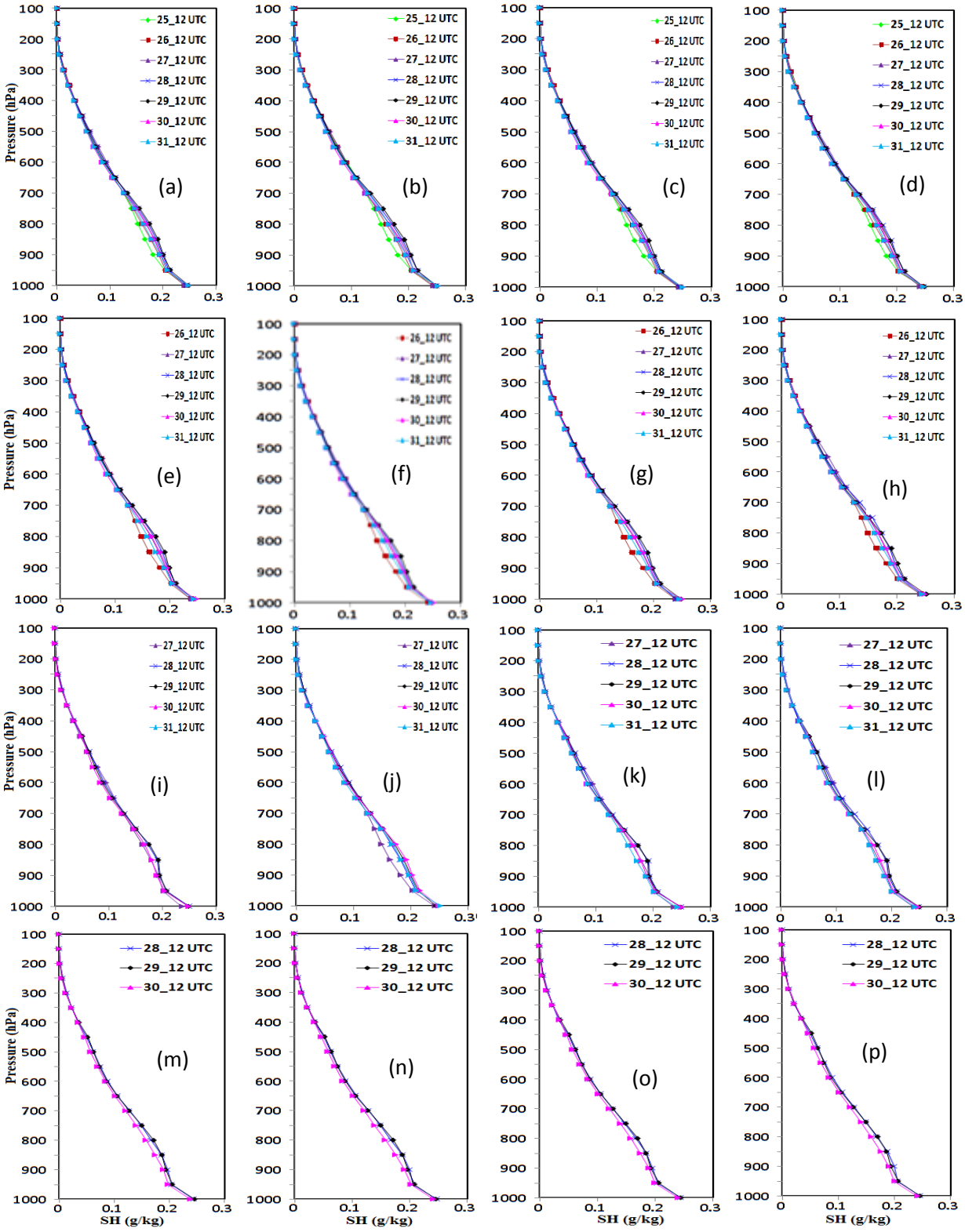

Figure 27: Vertical profiles of Model simulated area averaged SH (g/kg) of TC Mora at 1200 UTC of different days at rear position for four different MPs at (a-d) 25 May, (e-h) 26 May, (i-l) 27 May and (m-p) 28 May 0000 UTC initial conditions respectively.

The vertical variations of area average SH at the front position at 0000 UTC of 25 (Figure 26(a-d)), 26 (Figure 26(e-h)) and 27 (Figure 26(i-l)) May for WSM6, Thompson, WDM6 and NSSL schemes is found to decrease up to 30 May after that it increased on 31 May with little exception. For the initial conditions of 0000 UTC (Figure 26(m-p)) 28 May the vertical variations of area average SH is found to increase for all MP schemes till 30 May and decreased on 31 May with little exception.

The vertical variations of area average SH at the rear position indicate the SH increase for all MPs up to 29 May with little anomalies for the 0000 UTC of 25 (Figure 27(a-d)), 26 (Figure 27(e-h)), 27 (Figure 27(i-l)) and 28 (Figure 27(m-p)) May initial conditions and after that it has decrease after passing out the landfall. The SH at front and rear position is found to increase for all MPs for all initial conditions except 25 and 26 May at front position. The cyclone moves in a direction where the SH increases.

4.2.6 Water Vapor Mixing Ratio (WVMR)

The temporal distribution of area average simulated WVMR at 2 m level in front position for different MPs coupling with KF scheme of TC Mora for 0000 UTC of 25, 26, 27 and 28 May 2017 initial conditions are presented in Figure 28(a-d). The area average WVMR at front (Figure 28(a-d)) and rear positions (Figure 28(e-h)) are found minimum for WDM6 schemes and erratic behavior using the initial conditions of 0000 UTC of 25, 26, 27 and 28 May 2017. The simulated area average WVMR at front position (Figure 28a) for different MPs are rise and fall irregularly during 0000 UTC of 25 May to 1500 UTC of 29 May for and then WVMR has decreased except NSSL scheme for the initial conditions of 0000 UTC of 25 May. The area average WVMR is found maximum 24 g/kg and minimum 19.5 g/kg for NSSL and Thompson schemes respectively. For the initial conditions of 0000 UTC of 26 May (Figure 28b) the temporal distribution of area average shown that WVMR is increased continuously with the progression of time for all MPs and reached maximum at 1500 UTC of 28 May for different MPs respectively. The area average maximum and minimum WVMR is found 23 and 21.6 g/kg for Thompson and WDM6 schemes respectively.

The temporal distribution of area average WVMR for all MPs (Figure 28c) has shown increasing tendency of WVMR and reached maximum at 1500 UTC of 29 May for different MPs and simulated maximum and minimum WVMR are 23.9 and 20.2 g/kg for NSSL and WDM6 schemes for the initial conditions at 0000 UTC of 27 May. For the initial conditions at 0000 UTC of 28 May the area average WVMR at front position (Figure 28d) has increased

for all MPs and reached maximum at 1200 UTC of 30 May for different MPs and maximum and minimum WVMR are found 26 and 20.8 g/kg for WSM6 and WDM6 schemes respectively.

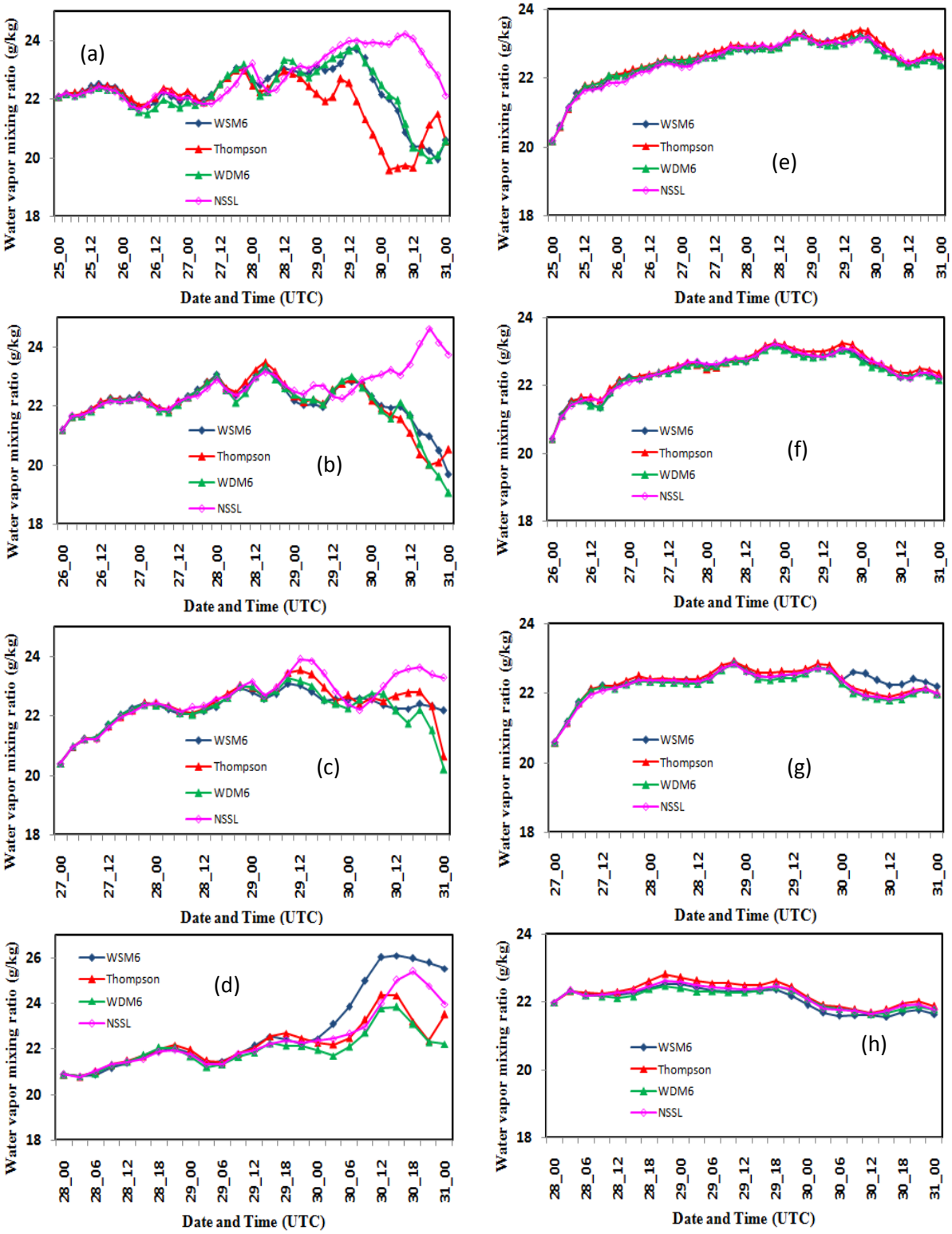

Figure 28: Model simulated area average WVMR of TC Mora for four different MPs at (a-d) front and (e-h) rear position with 0000 UTC of 25, 26, 27 and 28 May initial conditions respectively.

The area average WVMR at rear position for all MPs has increased and reached maximum (Figure 28e) at 1800 UTC of 29 May for all MPs respectively for the initial conditions at 0000 UTC of 25 May. The maximum and minimum WVMR is 23.4 and 20.6 g/kg for Thompson and WDM6 schemes. For the initial conditions of 0000 UTC of 26 (Figure 28f) and 27 (Figure 28g) May, the area average WVMR for all MPs has increased up to 1800 UTC of 29 May and 2100 UTC of 28 May and after that it has decreased. The area average maximum and minimum WVMR is 23.2 & 20.4 and 22.9 & 20.4 g/kg for Thompson and NSSL schemes based on the initial conditions on 26 and 27 respectively. The area average WVMR (Figure 28h) is found to increase till 2100 UTC of 28 May and after that it decreased for all MPs for the initial conditions of 0000 UTC of 28 May. The maximum and minimum WVMR are 22.8 and 21 g/kg for Thompson and WSM6 schemes. The cyclone moves in a direction where the WVMR has increased.

4.2.7 Relative Humidity (RH)

Model simulated vertical profiles of area averaged RH (%) at the front position with four different MPs are presented in Figure 29(a-p) for initial conditions at 0000 UTC of 25, 26, 27 and 28 May 2017. The distribution pattern of RH at 0000 UTC and 1200 UTC are almost similar so that only 1200 UTC graphs are presented. The vertical variation of area average RH Shows that RH increases for WSM6, Thompson, WDM6 and NSSL schemes (Figure 29(a-d)) during 27-29 May and decrease on 30-31 May i.e. after landfall with little exception for the initial conditions of 0000 UTC of 25 May. The vertical variation of area average RH is found to increase for all MPs during 26-29 (Figure 29(e-h)) and is found to decrease on 30-31May i.e. after landfalls for the initial conditions of 0000 UTC of 26 May. For the initial conditions of 0000 UTC of 27 May the area average RH is found to increase for all MP schemes during 27-30 May (Figure 29(i-l)) and decreased on 31 May. The vertical variation of area average RH is found to increase for all MP schemes during 28-29 May (Figure 29(m-p)) and decreased on 30 May with little exception for the initial conditions of 0000 UTC of 28May.

Vertical variations of area averaged RH (%) at rear position with four different MPs coupling with KF scheme for initial conditions at 0000 UTC of 25, 26, 27 and 28 May 2017 are presented in Figure 30(a-p). The area average RH is found to decrease for all MPs and for all initial conditions (Figure 30(a-p)) from the starting of model run to 29 May and after that it has increased.

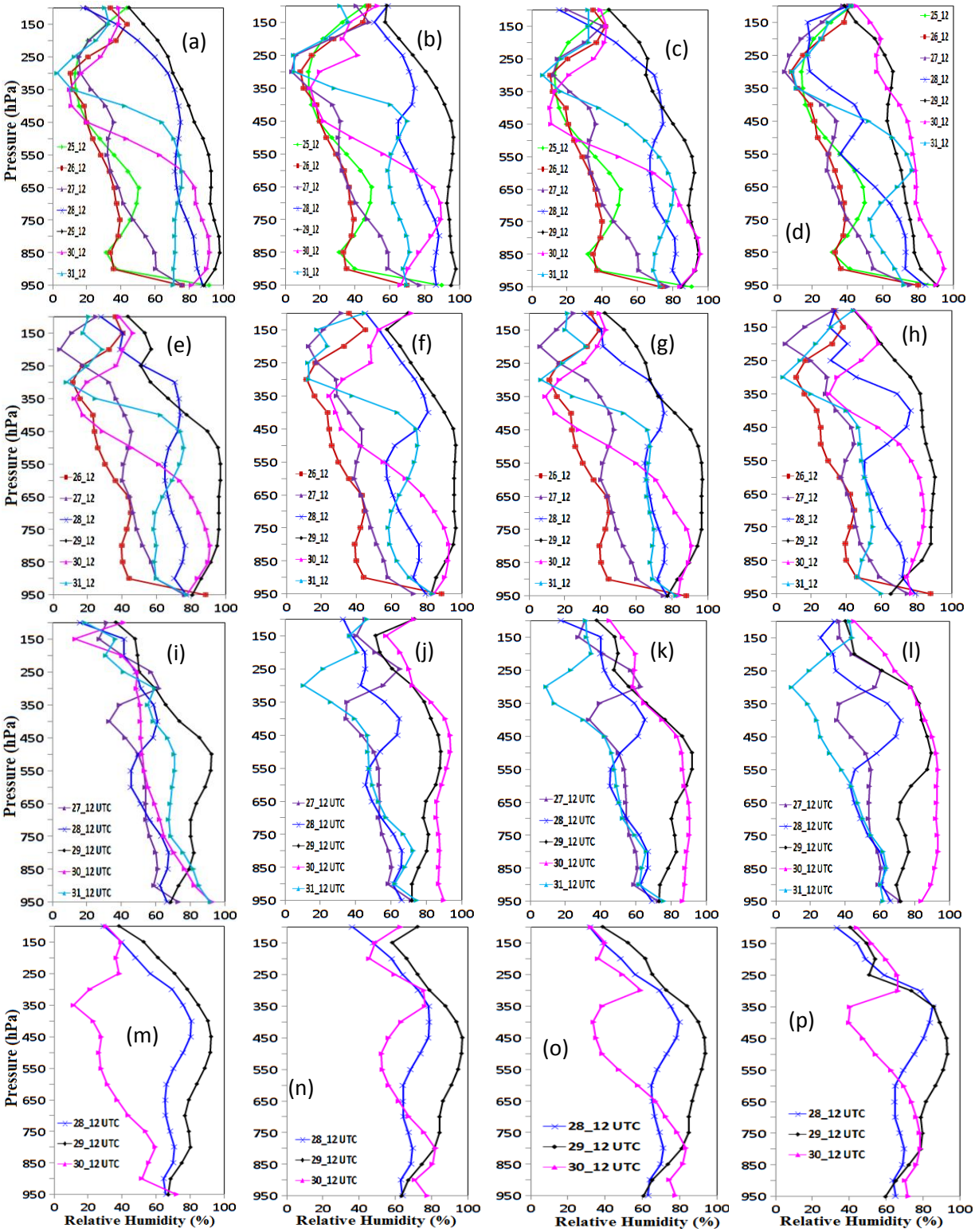

Figure 29: The vertical variation of model simulated area average RH (%) at 1200 UTC of different days in front position of TC Mora for four different MPs at 0000 UTC on (a-d) 25 May, (e-h) 26 May, (i-l) 27 May and (m-p) 28 May 2017 initial conditions respectively.

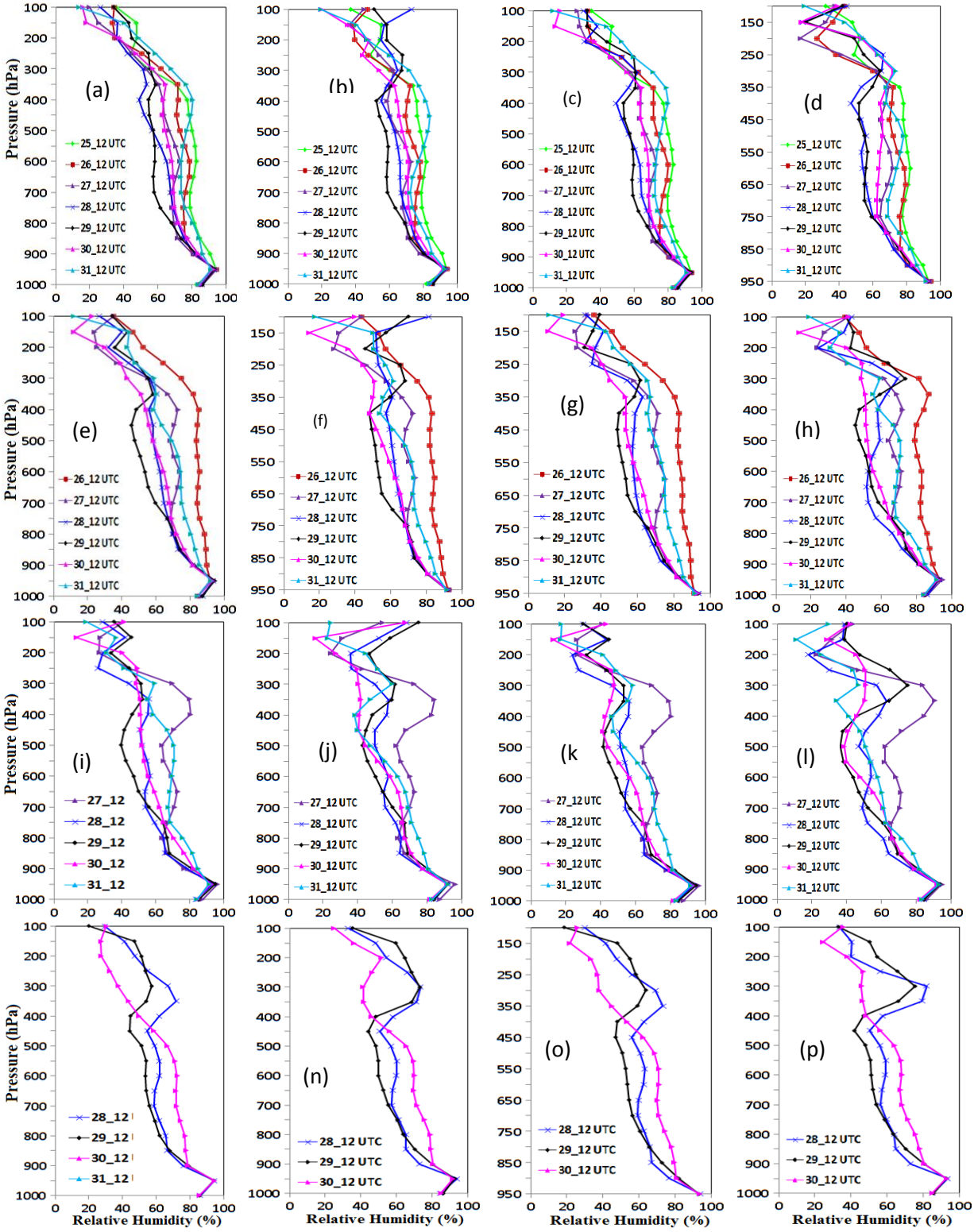

Figure 30: The vertical variation of model simulated area average RH (%) at 1200 UTC of different days in rear position of TC Mora for four different MPs at 0000 UTC of (a-d) 25 May, (e-h) 26 May, (i-l) 27 May and (m-p) 28 May 2017 initial conditions respectively.

The RH is found to increase at front position and decrease at rear position from the starting of model run to 29 May and after that it has increased at rear position and decreased at front position. The cyclone moves in a direction where the RH has increased.

4.2.8 Temperature Anomaly

The simulated area average temperature anomalies at the front and rear positions of TC Mora at 0000 UTC of 25, 26, 27, and 28 May 2017 for WSM6, Thompson, WDM6 and NSSL schemes are presented in Figure 31(a-p) and Figure 32(a-p) respectively. The temperature is found to increase at front position from 650-150 hPa for all initial conditions and decrease from 900 hPa to 700 hPa level with the initial conditions at 0000 UTC of 25, 26 and 27 May with little anomalies with the progression of time. The distribution patterns of temperature at 0000 UTC and 1200 UTC are almost similar so that only 1200 UTC graphs are presented.

The area average temperature is increased and decreased continuously from 650-150 and 950-700 hPa levels at front position of TC Hudhud for WSM6, Thompson, WDM6 and NSSL schemes from the initial conditions of model run to 1200 UTC of 29 May with little exception for the initial conditions of 0000 UTC of 25 (Figure 31(a-d)), 26 (Figure 31(e-h)) and 27 (Figure 31(i-l)) May. The increase of average temperature is found maximum at 200 hPa for all MPs for all the initial conditions of model run. This increase is significant in the upper troposphere for WSM6, Thompson and WDM6 schemes on 29 May for the initial conditions of 0000 UTC of 25 and 26 May and mid troposphere for the initial conditions of 0000 UTC of 27 May. The area average temperature increase has not significant for NSSL scheme for all the initial conditions of model run. For the initial conditions at 0000 UTC of 28 (Figure 31(m-p)) May, the temperature is found to increase for all MPs on 29 May at all levels.

The temperature at rear position is found to increase for all MPs during 950-700 and 600-500 hPa and decreases at 600-500 and 400-150 hPa for the initial conditions of 0000 UTC of 25 (Figure 32(a-d)), 26 (Figure 32(e-h)), 27 (Figure 32 i-l) and 28 (Figure 32 m-p) May. The maximum increase and decrease of temperature has found 850 and 200 hPa with little exception. The pattern looks like crisscross in the vertical direction.

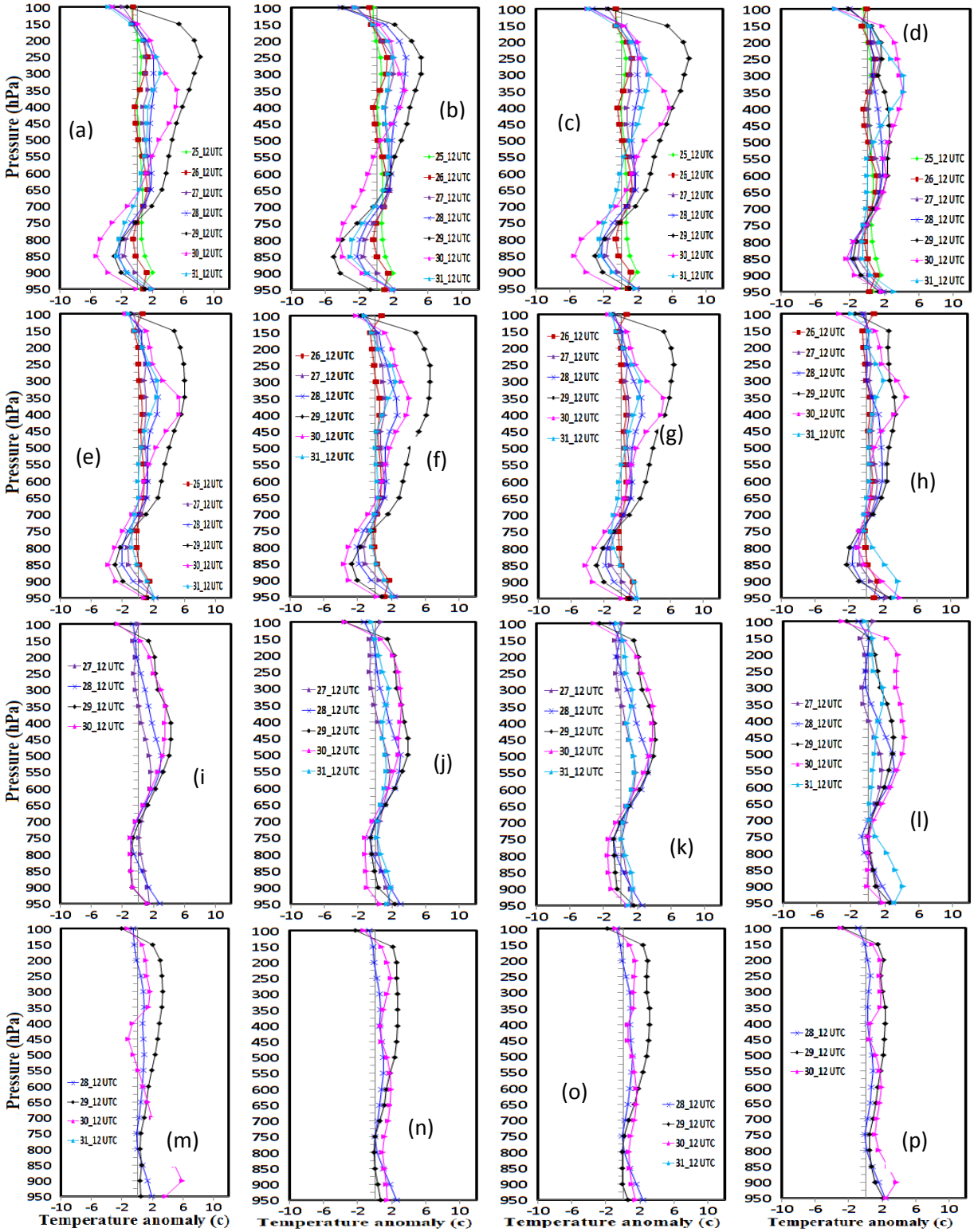

Figure 31: Vertical variation of Model simulated temperature anomaly at front position of TC Mora using different MPs with the initial conditions at 0000 UTC on (a-d) 25 May, (e-h) 26 May, (i-l) 27 May and (m-p) 28 May 2017 respectively.

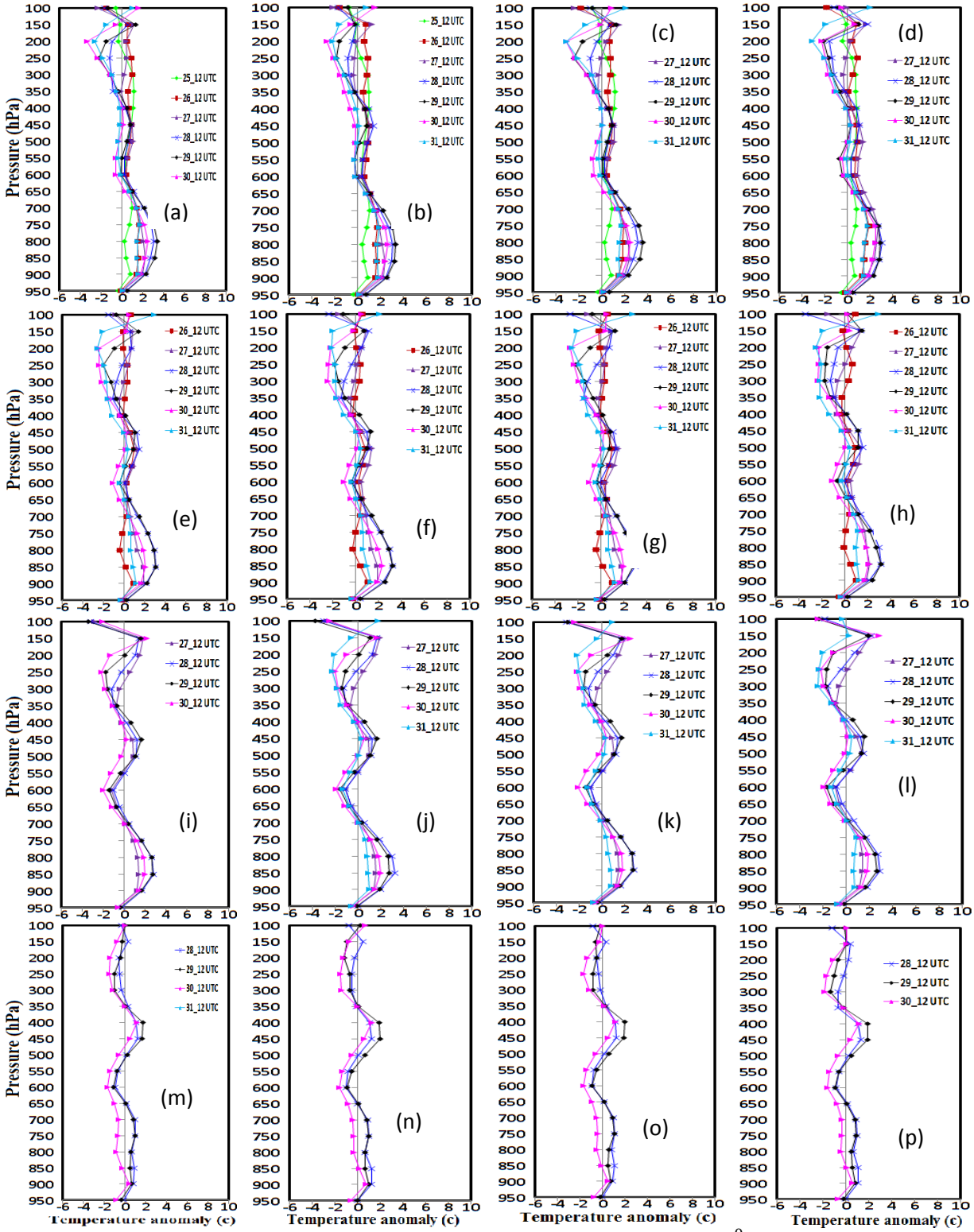

Figure 32: Vertical variation of Model simulated temperature anomaly (^{0}C) at rear position of TC Mora using four different MPs with the initial conditions at 0000 UTC on (a-d) 25 May, (e-h) 26 May, (i-l) 27 May and (m-p) 28 May 2017 respectively.

The temperature is found to increase at front position from 650-150 hPa for all initial conditions and decrease from 900-700 hPa level with the initial conditions at 0000 UTC of

25, 26 and 27 May with little anomalies with the progression of time. The maximum increase and decrease of temperature has found 850 and 200 hPa with little exception at rear position.

4.2.9 Wind Speed (WS) at different pressure level

The wind speed forecasts at front domain for TC Mora using four different MPs with the initial conditions at 0000 UTC of 25, 26, 27 and 28 May 2017 are presented in Figure 33(a-p). The distribution pattern of wind speed is almost similar at 0000 UTC and 1200 UTC so that only 1200 UTC graphs are presented. The area average wind speed is almost constant at different vertical levels for all MPs during 25-27 May from 950 to 250 hPa level (Figure 33(a-d)) and after that it is increased significantly during 27-29 May as the cyclone moves towards the front and decreased on 30 May except NSSL scheme by which the wind speed is also increased for the initial conditions at 0000 UTC of 25 May. The area average wind speed has increased little at 26 to 27 May for all MPs from 950 to 250 hPa (Figure 33(e-h)) level and after that it has increased significantly during 27-29 May as the cyclone moves toward the front and is found to decrease on 30 May except NSSL scheme by which the wind speed is also increased for the initial conditions at 0000 UTC of 26 May. The area average wind speed is found to increase significantly for all MPs from 950 to 250 hPa level (Figure 33(i-l)) during 27-30 May as the cyclone moves towards front for the initial conditions at 0000 UTC of 27 May. The area average wind speed is found to increase significantly for all MPs from 950 to 400 hPa level (Figure 33(m-p)) during 28-29 May as the cyclone moves towards front and is found to decrease on 30 May for the initial conditions at 0000 UTC of 28 May. The wind speed is still higher on 30 May i.e., after crossing the front position for NSSL scheme with all initial conditions. On 29 May the WS is found significantly higher at 850 hPa level for WSM6, Thompson and WDM6 schemes for the initial conditions at 0000 UTC of 25, 26 and 28 May.

The area average wind speed at rear position is found to decrease for all MPs from the day of model run to 30 May except 25 May for the initial conditions at 0000 UTC of 25 (Figure 34(a-d)), 26 (Figure 34(e-h)), 27 (Figure 34(i-l)) and 28 (Figure 34(m-p)) May. The area average wind speed is found maximum at 850 hPa and minimum at 400 hPa at rear position for all MPs for all initial conditions. The area average WS is found to increase at front position from 950 to 250 hPa levels for all MPs before crossing the cyclone at front position for all initial conditions. The area average WS at rear position is found to decrease and reached minimum at 400 hPa level for all MPs from the day of model run to 30 May except 25 May for all initial conditions.

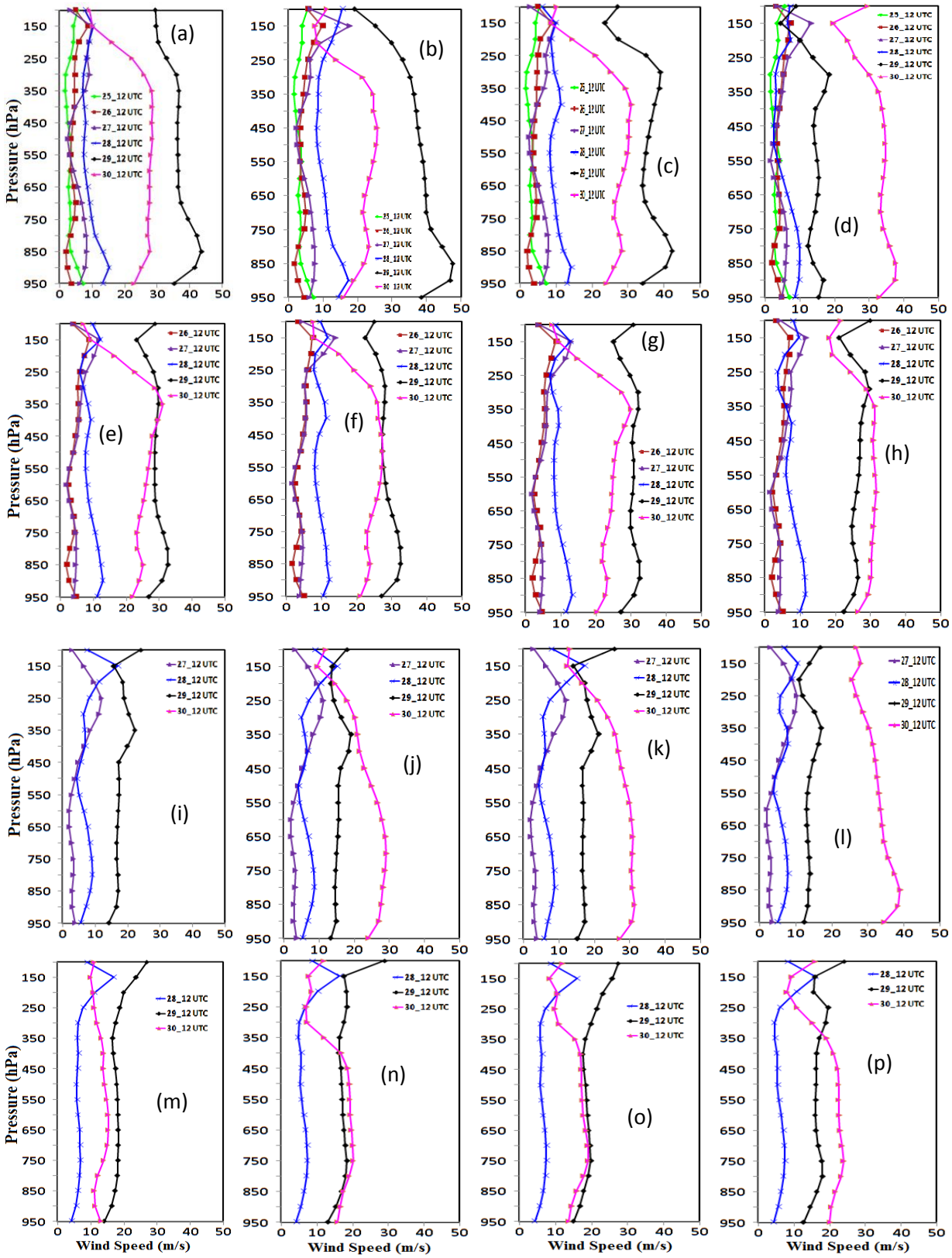

Figure 33: Vertical profiles of Model simulated area average wind speed at front position of TC Mora using four different MPs with the initial conditions at 0000 UTC on (a-d) 25 May, (e-h) 26 May, (i-l) 27 May and (m-p) 28 May 2017 respectively.

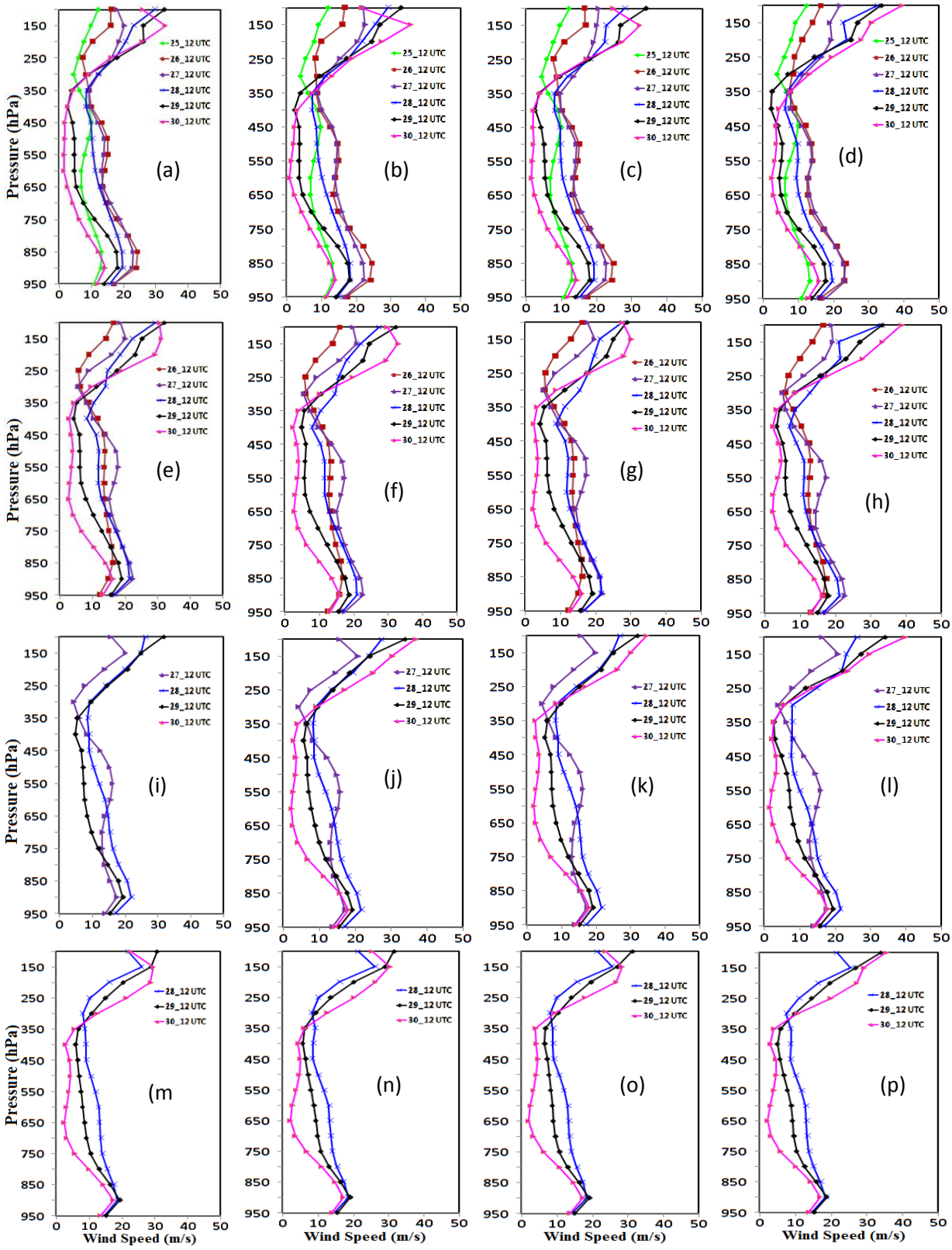

Figure 34: Vertical profiles of Model simulated Model simulated area average wind speed at rear position of TC Mora using four different MPs with the initial conditions at 0000 UTC on (a-d) 25 May, (e-h) 26 May, (i-l) 27 May and (m-p) 28 May 2017 respectively.

4.2.10 Wind Direction (WD)

Model simulated vertical variations of area average WD at front position for four different MPs are presented in Figure 35(a-p) for initial conditions at 0000 UTC of 25, 26, 27 and 28 May 2017. The distribution pattern of WD for all MPs with different initial conditions at 0000 UTC and 1200 UTC are almost similar and only the graphs at 1200 UTC are presented.

The south-southwesterly wind is flowing at different levels on 25 and 26 May and southeasterly wind is flowing from surface to 550 hPa and southwesterly from 500 to 150 hPa level during 27-29 May (Figure 35(a-d)) for the 0000 UTC of 25 May initial conditions. On 30 May westerly wind is simulated at all levels by Thompson, WSM6 and WDM6 schemes and southerly wind by NSSL schemes. Due to the south-southwesterly wind in the upper troposphere during 27-29 May and westerly wind on 30 May the TC Mora moved towards Bangladesh coast.

On 26 May the easterly wind is flowing in the lower troposphere and westerly wind is simulated in the middle to upper troposphere for all MPs with the initial conditions at 0000 UTC of 26 May (Figure 35(e-h)). The easterly wind is flowing from surface to 500 hPa and southerly wind from 500 to 150 hPa levels during 27-29 May. On 30 May the wind is westerly from surface to 100 hPa level for all MPs with the initial conditions at 0000 UTC of 26 May. Due to the southerly wind in the upper troposphere during 27-29 May and westerly wind at all levels on 30 May the TC Mora moved towards Bangladesh coast.

On 27 May the wind flowing southwesterly to easterly from surface to 600 hPa and southwesterly wind flowing from 600 to 100 hPa for all MPs and 28-29 May easterly to southeasterly wind is flowing and on 30 May the wind flow is shifted to westerly from surface to 100 hPa levels for all MPs with the 0000 UTC of ((Figure 35(i-l)) 27 May and 28 May (Figure 35(m-p)) initial conditions. Due to the southeasterly wind flow in the upper air during 28-29 and westerly wind at all levels on 30 May the TC Mora moved towards Bangladesh coast. It is observed from the model simulated results that at rear position the area average wind is flowing southwesterly to westerly from surface to 400 hPa and southerly to easterly from 400 to 100 hPa levels for all MPs for the initial conditions at 0000 UTC of 25 (Figure 36(a-d)), 26 (Figure 36(e-h)), 27 (Figure 36(i-l)) and 28 (Figure 36(m-p)) May 2017.

It is clearly seen that due to the southwesterly wind in the upper troposphere during 27-29 May 2017 and westerly wind at all levels on 30 May the TC Mora moved towards Bangladesh coast.

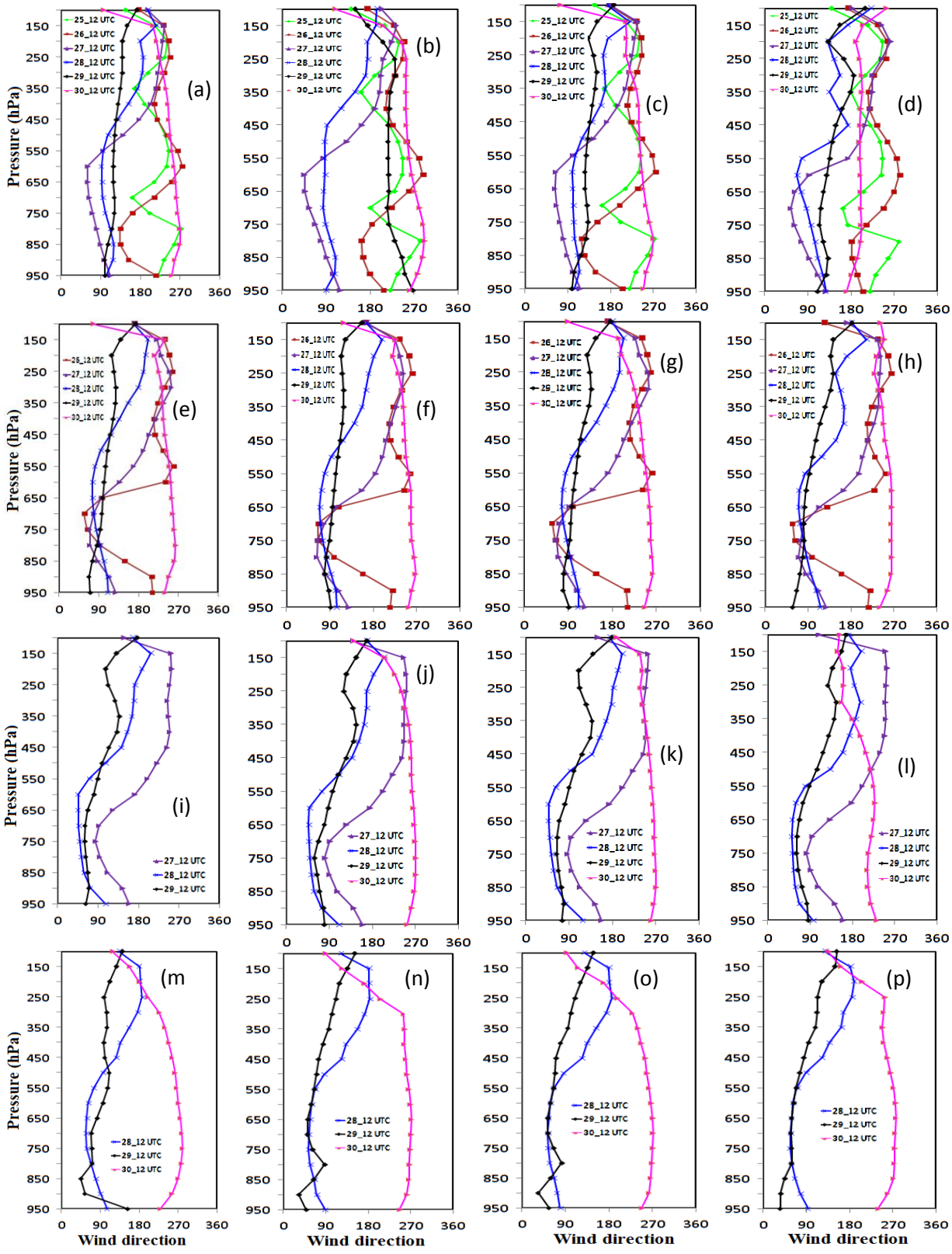

Figure 35: Vertical profiles of Model simulated area average wind direction at 1200 UTC of different days at front position of TC Mora for four different MPs on (a-d) 25 May, (e-h) 26 May, (i-l) 27 May and (m-p) 28 May 0000 UTC initial conditions.

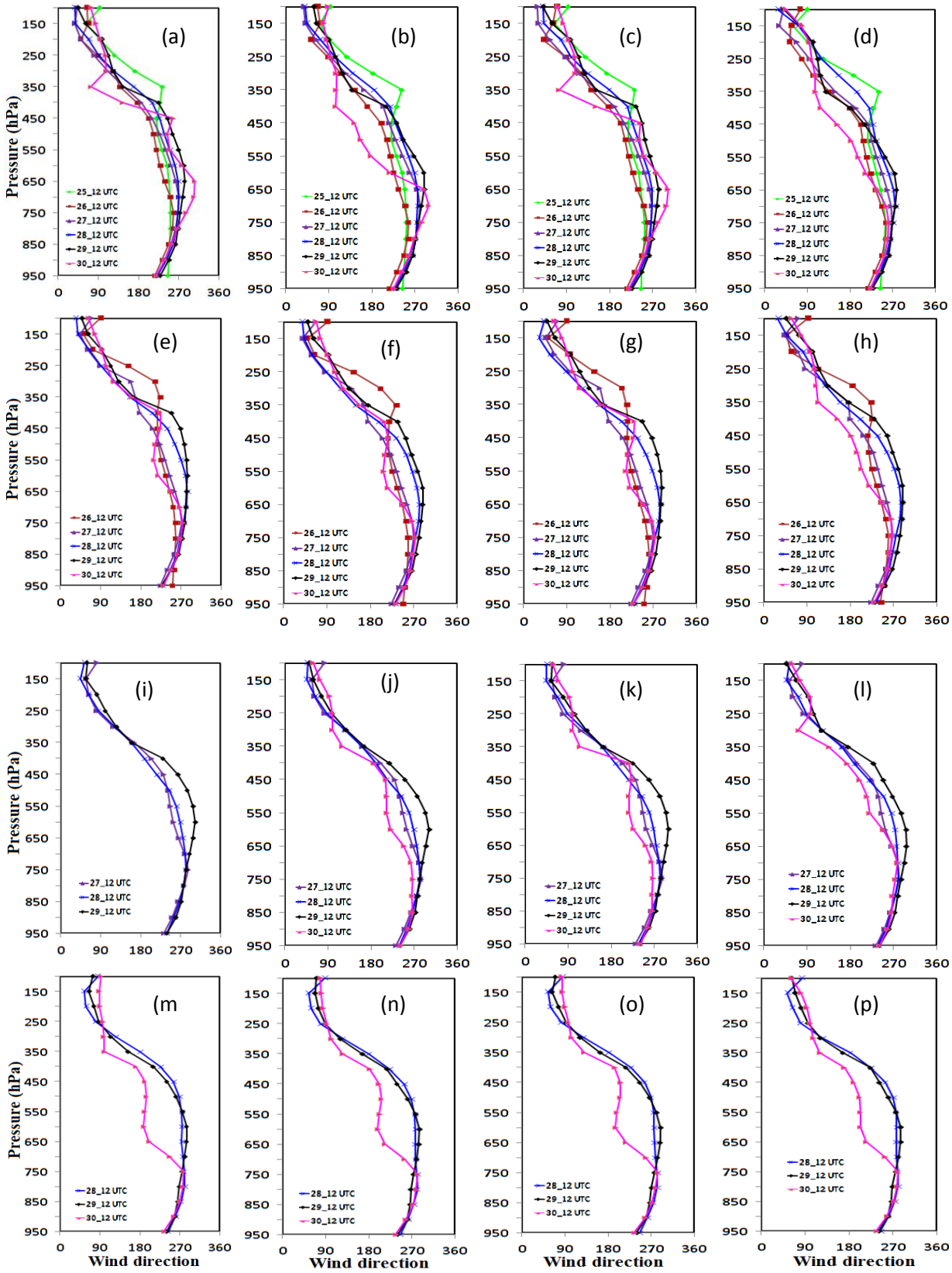

Figure 36: Vertical profiles of Model simulated area average wind direction at 1200 UTC of different days in rear position of TC Mora for four different MPs with (a-d) 25 May, (e-h) 26 May, (i-l) 27 May and (m-p) 28 May 0000 UTC initial conditions respectively.

4.2.11 Convective Available Potential Energy (CAPE)

Model simulated vertical variations of area average CAPE at front position with four different MPs for 0000 UTC of 25, 26, 27 and 28 May 2017 initial conditions are presented in Figure 37(a-p). It is found from Figure 37(a-p) that the CAPE has decreased continuously from 950 to 800 hPa for all combination of MPs with different initial conditions. The CAPE is found to be zero from 800 to 100 hPa level, that's why the value of CAPE has been plotted up to 800 hPa. The distribution patterns of CAPE at 0000 UTC and 1200 UTC are almost similar so that only 1200 UTC graphs are presented.

The area average CAPE is found to decrease for WSM6, Thompson, WDM6 and NSSL schemes during 25-26 May (Figure 37(a-d)) and increase during 26-29 and decrease again on 30 May with little exception for the initial conditions of 0000 UTC of 25 May. The area average CAPE is found to decrease for all MP schemes during 26-27 May (Figure 37(e-h)) and increase on 28 and decrease again on 30 May with little exception for the initial conditions of 0000 UTC of 26 May.

The area average CAPE is found to increase for WSM6, Thompson, WDM6 and NSSL schemes during 27-29 May (Figure 37(i-l)) and decrease again on 30 May for the initial conditions of 0000 UTC of 27 May. The area average CAPE is found to increase for WSM6, Thompson, WDM6 and NSSL schemes during 28-30 May (Figure 37(m-p)) for the initial conditions of 0000 UTC of 28 May.

Model simulated vertical variation of area average CAPE at rear position with four different MPs are presented in Figure 38(a-p) for 0000 UTC of 25, 26, 27 and 28 May 2017 initial conditions. It is found from Figure 38(a-h) that the CAPE has decreased for all combination of MPs during 25-26 and increased up to 29 May then decreased on 30 May with little exception for the initial conditions of 0000 UTC of 25 and 26 May. The area average CAPE is found to increase from 27 to 29 May and decrease on 30 May for the initial conditions of 0000 UTC of (Figure 38(i-l)) 27 and (Figure 38(m-p)) 28 May 2017. Due to the increase of area average CAPE at lower troposphere at front position the TC Mora moved towards front position.

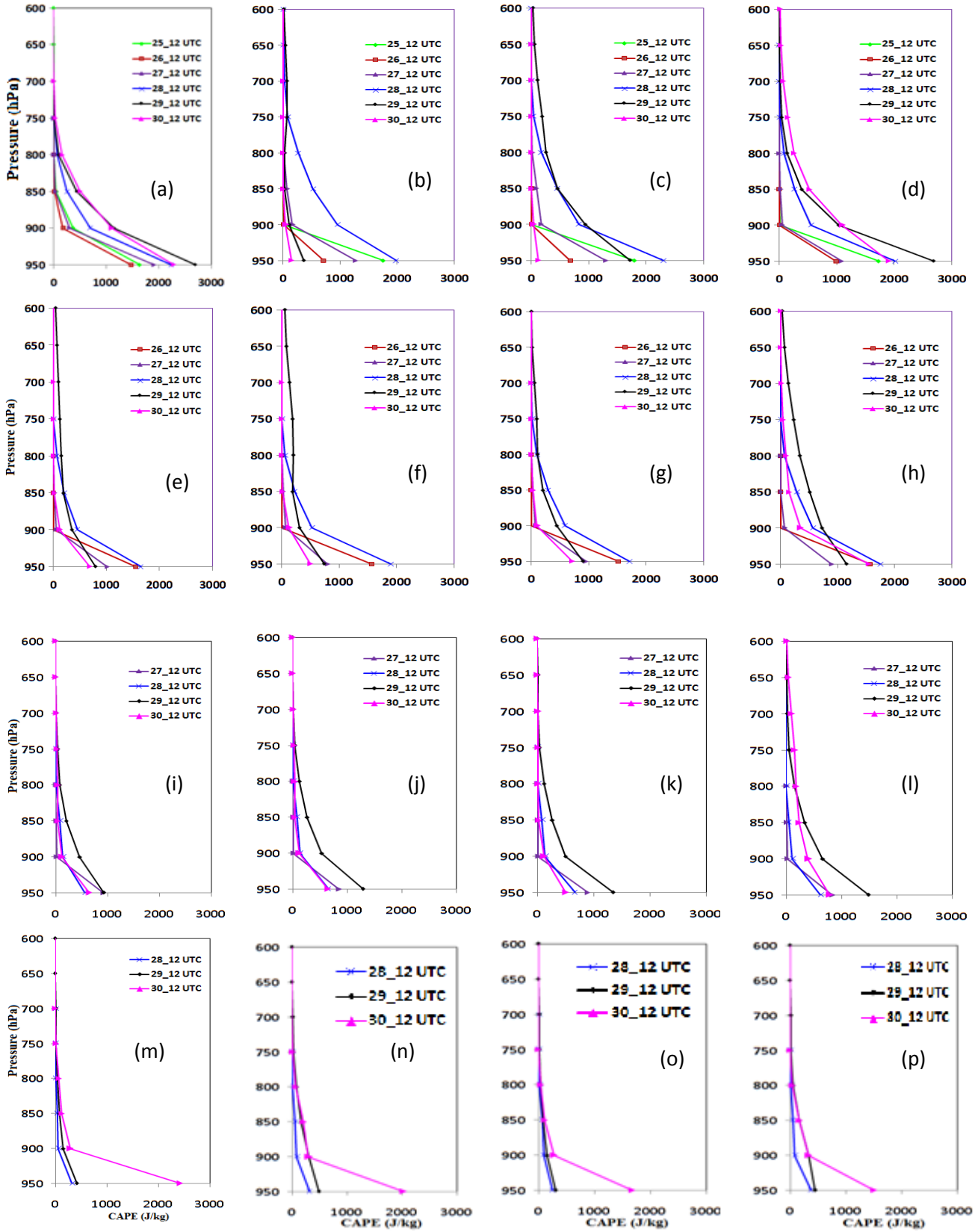

Figure 37: Vertical profiles of Model simulated area average CAPE at front position of TC Mora using four different MPs with the initial conditions at 0000 UTC of (a-d) 25 May, (e-h) 26 May, (i-l) 27 May and (m-p) 28May 2017 respectively.

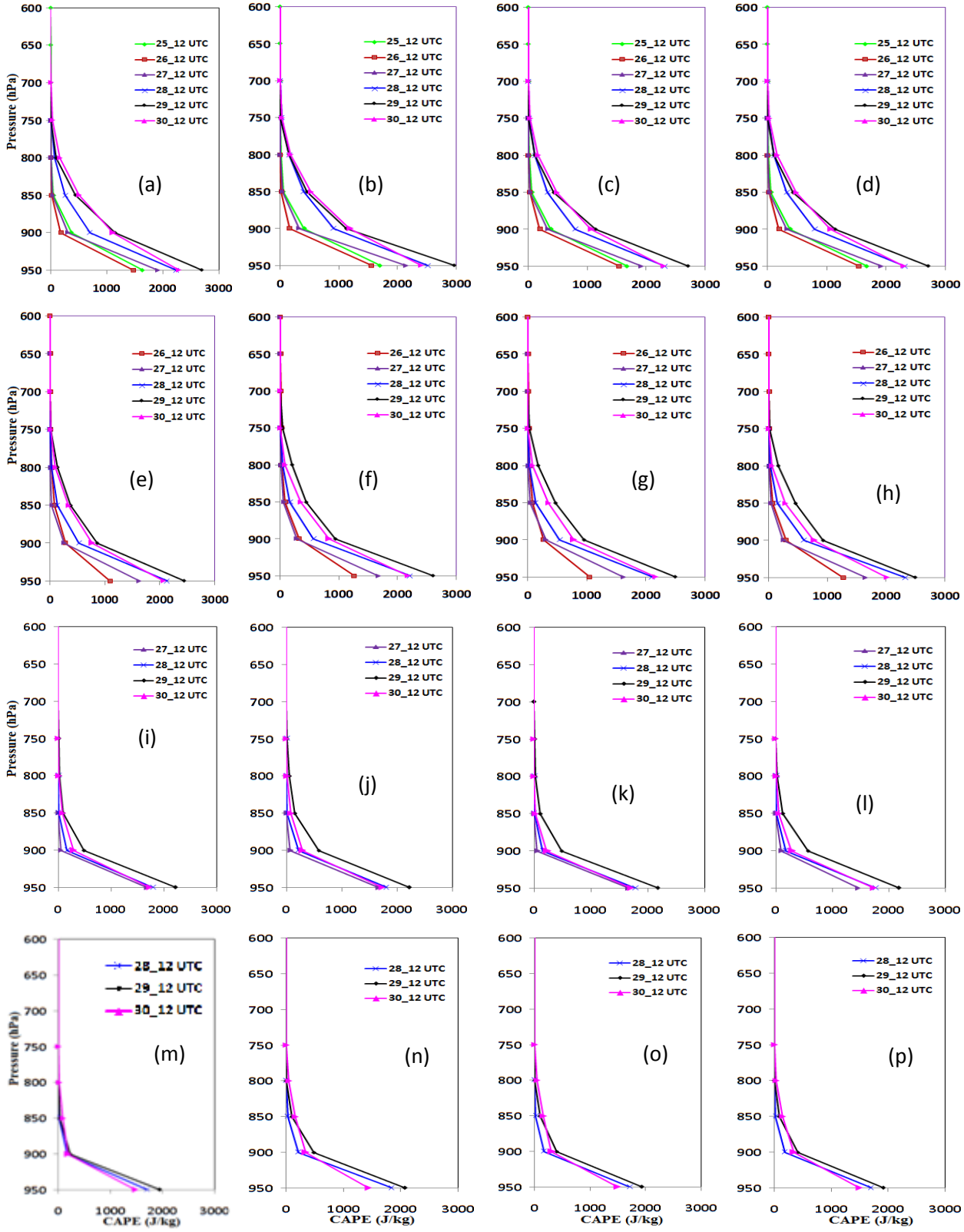

Figure 38: Vertical profiles of Model simulated area average CAPE at rear position of TC Mora using four different MPs with the initial conditions at 0000 UTC of (a-d) 25 May, (e-h) 26 May, (i-l) 27 May and (m-p) 28 May 2017 respectively.

4.1.12 Convective Inhibition (CIN)

Model simulated vertical variations of area average CIN at the front and rear positions with four different MPs with 0000 UTC of 25, 26, 27 and 28 May 2017 initial conditions are presented in Figure 39(a-p) and Figure 40(a-p). It is found from Figure 39(a-p) that the CIN has reached near to zero at 800 hPa. That's why the value of CIN has been plotted up to 800 hPa. The changing pattern of CIN at 0000 UTC and 1200 UTC are almost similar so that only 1200 UTC graphs are presented.

The area average CIN is found to increase for all MP schemes during 25-27 May (Figure 39(a-d)) and decrease during 28-30 May at 900 to 700 hPa level for the initial conditions of 0000 UTC of 25 May. The area average CIN is found to decrease for all MP schemes during 26-30 May (Figure 39(e-h)) except NSSL scheme for the initial conditions of 0000 UTC of 26 May. The area average CIN is found to decrease for all MP schemes during 27-29 May (Figure 39(i-l)) and decrease on 30 May except NSSL for the initial conditions of 0000 UTC of 27 May. For the initial conditions of 0000 UTC of 28 May the area average CIN is found to increase (Figure 39(m-p)) for WSM6, Thompson, WDM6 and NSSL schemes during 28-29 May and then decrease on 30 May.

The area average CIN at rear position is simulated zero at the surface for all MPs for all the initial conditions and are presented in Figure 40(a-p). Maximum amount of CIN has simulated at 900 hPa and it increase for all MPs during 25-29 (Figure 40(a-d)) and 26-29 (Figure 40(e-h)) May and decrease on 30 May for the initial conditions at 0000 UTC of 25 and 26May. The area average CIN is found to increase for all MP schemes during 27-29 May (Figure 40(i-l)) and 28-29 May (Figure 40(m-p)) and decreased 30 May for the initial conditions of 0000 UTC of 27 and 28 May 2017.

It is seen that the CIN is found to increase at 900 hPa level at front and rear positions during the starting of initial conditions of model run to that of 29 May and it decreased on 30 May. But the maximum values of CIN are insignificant, which is favorable for cyclone movement in that direction.

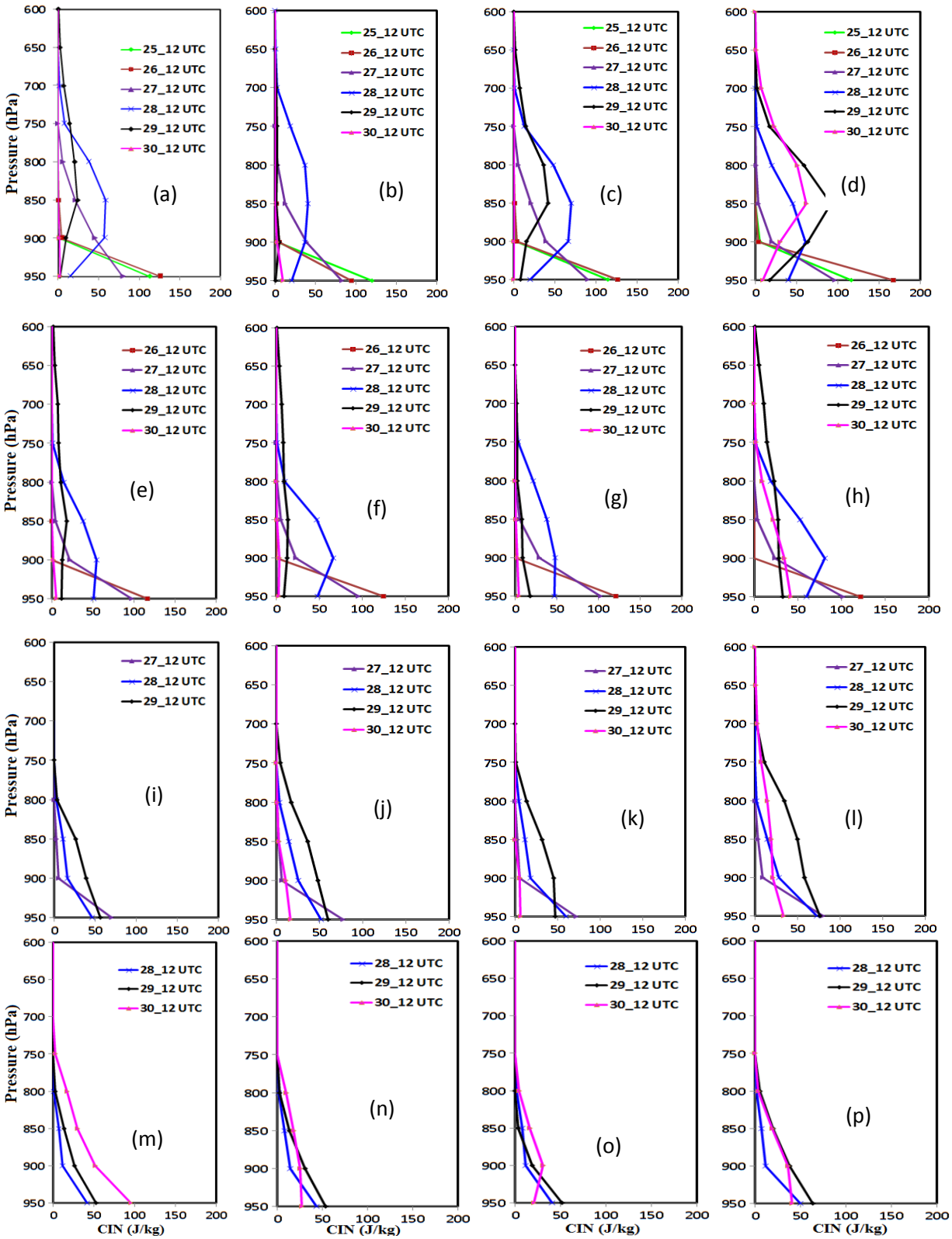

Figure 39: Model simulated area average CIN at front position of TC Mora for four different MPs on (a-d) 25 May, (e-h) 26 May, (i-l) 27 May and (m-p) 28 May 0000 UTC initial conditions respectively.

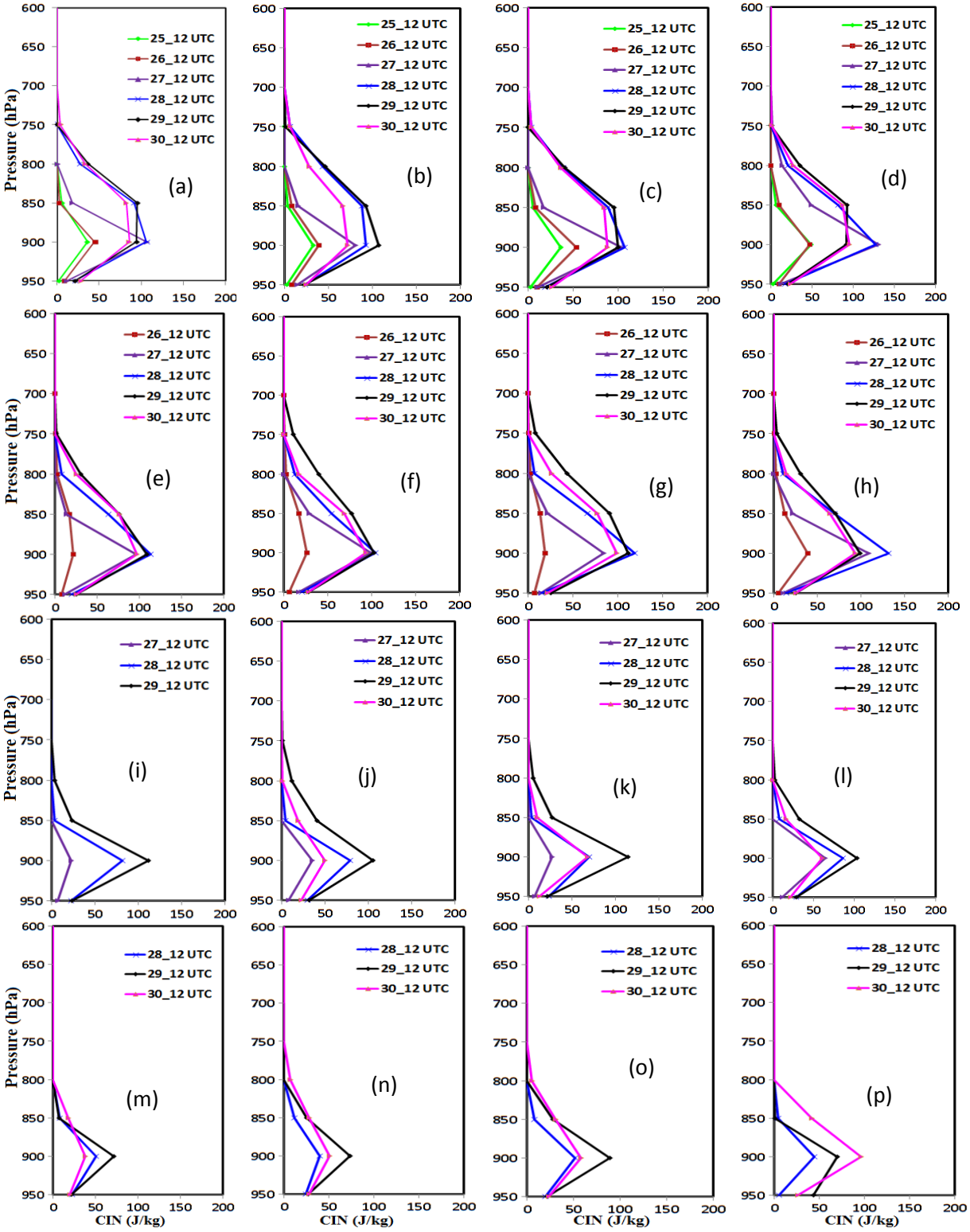

Figure 40: Vertical profiles of Model simulated area average CIN at rear position of TC Mora for four different MPs on (a-d) 25 May, (e-h) 26 May, (i-l) 27 May and (m-p) 28 May 0000 UTC initial conditions respectively.

Chapter V
Conclusions

In this research, WRF-ARW model has been used to simulate the characteristic features of TC Hudhud and Mora those formed in the Bay of Bengal and crossed the coasts of Visakhapatnam of India and Bangladesh. The NCEP FNL data is interpolated to the model horizontal and vertical grids and the model has been integrated for 168, 144, 120 and 96-h period for TC Hudhud and TC Mora. 16 experiments have been conducted in each of TCs by using WSM6-class graupel scheme, Thompson graupel, WDM6-class graupel and NSSL momentum-1 schemes in combination with KF scheme with four different initial conditions. In this regard, the initial conditions of 0000 UTC of 6, 7, 8 and 9 October 2014 have been considered for TC Hudhud and 0000 UTC of 25, 26, 27 and 28 May 2017 have been considered for TC Mora. To examine the impact of environmental moisture on the intensification of TCs we have considered two regions inside the model domain as front and rear of the cyclone. We have considered (17-20^{o}N & 85-88^{o}E) and (7-10^{o}N & 92-95^{o}E) position of TC Hudhud and (20-22^{o}N & 88-92^{o}E) and (8-10^{o}N & 86-90^{o}E) position of TC Mora as the front and rear positions of TCs respectively. Track of TCs, Maximum wind speed at 10m level, Minimum Sea level pressure (SLP), Convective available potential energy (CAPE), Convective inhibition (CIN), Relative Humidity (RH), Specific Humidity (SH), Water vapor mixing ratio (WVMR) at 2 meter level, Temperature anomaly, Wind speed (WS) and Wind direction (WD) at different levels have been simulated and analyzed in rear and front position.

The simulated MWS for all MPs at front position for TC Hudhud is similar with all initial conditions but for TC Mora it is much higher than that of IMD estimated wind speed. The time to reach MWS for all MPs is almost similar for TC Hudhud but in case of TC Mora the simulated MWS is found to reach much earlier than that of observed. For different initial conditions of model run and for all MPs, the MWS of TC Hudhud and TC Mora at rear position is decreased continuously and found to remain almost constant with the progression of TC towards land. The SH at front and rear positions is found to increase for TC Hudhud and TC Mora for all MPs till on 1200 UTC of 11 October for all initial conditions except NSSL scheme for all initial conditions except 25 and 26 May at front position respectively. The MSLP for TC Hudhud and TC Mora is found to decrease at front position with the movement of TC towards land and after landfall it is found to increase again; at rear position it has increased continuously during the time of movement of TCs. At rear position, the SLP is almost constant for all MPs and for all initial conditions of model run.

The area average WVMR at front and rear position has found to increase up to 1800 UTC of 29 May except 27 and 28 May at front position for all MPs and for all initial conditions of TC Mora. The RH is found to increase and decrease at front and rear position respectively before crossing the land for

all initial conditions of model run of TC Hudhud and TC Mora after that it has decreased at front and increased at rear position. This suggests that the WVMR is increased in front position towards the movement of TCs. The temperature has increased at all vertical levels for all MPs at front position of TC Hudhud for all initial conditions with little exception. The temperature is found to increase at front position of TC Mora from 650-150 hPa and decreased from 900-700 hPa level for all initial conditions of model run with little anomalies with the progression of time. At rear position it has found two crest one at 750 hPa and another at 200 hPa and one trough at 400 hPa level where the area average temperature continuously decreased and reached negative for all initial conditions and for all MP schemes. In case of TC Mora the vertical variation of temperature is found zigzag.

The area average WS for TC Hudhud and Mora is found to increase at front position from 950 to 250 hPa levels for all MPs before crossing the land and after crossing it is found to decrease for all initial conditions. The area average WS at rear position of TC Hudhud is found to decrease from 950 to 450 hPa levels for all MPs for all initial conditions and for TC Mora it is found to decrease and reached minimum at 400 hPa level for all MPs for all initial conditions. Due to the northeasterly to easterly wind from surface to 200 hPa level during 8-10 October 2014 and southeasterly wind on 11 October at front position the TC Hudhud moved towards eastern coast of India and for southwesterly wind in the upper troposphere during 27-29 May 2017 and westerly wind at all levels on 30 May the TC Mora moved towards Bangladesh coast.

The area average CAPE at lower troposphere has increased for all MP schemes during 9-10 October for TC Hudhud and 27-29 May for TC Mora at front position. The CIN at front and rear position is found to increase at or below 900 hPa level for TC Hudhud and TC Mora during the starting of initial conditions of model run and when the cyclone near to the front it is found to decrease but the simulated values of CIN are insignificant, which is suitable for the intensification of TCs.

Reference

Arakawa, A.; V. R. Lamb, 1977: Computational design of the basic dynamical processes of the UCLA general circulation mode, Methods of Computational Physics, *New York: Academic Press*, 17, 173–265.

Bianco, L., J.-W. Bao, C. W. Fairall, and S. A. Michelson, 2011: Impact of sea-spray on the atmospheric surface layer. *Boundary Layer Meteor*., 140, 361–381.

Bogner, P. B., G. M. Barnes, J. L. Franklin, 1999: Conditionsal Instability and Shear for Six Hurricanes over the Atlantic Ocean. *Amer. Meteor. Soc.,* 15, 192-207.

Braun, S. A., Sippel, J. A., and D. S. Nolan, 2012: The Impact of Dry Midlevel Air on Hurricane Intensity in Idealized Simulations with No Mean Flow, *J. Atmos. Sci.,* 69, 236–257, doi:10.1175/JASD-10-05007.1.

Camargo S. J., A. W. Robertson, S. J. Gaffney, P. Smyth and M. Ghil, 2007: Cluster Analysis of Typhoon Tracks. Part II: Large-Scale Circulation and ENSO. *J. Climate*., 20, 3654-3676

Choi K. S., & I. J. Moon, 2012: Changes in tropical cyclone activity that has affected Korea since 1999. *Nat Hazards*, 62, 971–989.

Choi, S. and H., Byun, 2010: Possible relationship between western North Pacific tropical cyclone activity and Arctic Oscillation, *Theor. Appl. Climatol.,* 100, 261-274 DOI10.1007/s00704-009-0187-9.

Colby, Jr., P. Frank 1984: Convective Inhibition as a Predictor of Convection during ave-sesame II. *Mon. Wea. Rev.*, 112, 11, 2239–2252.

Colon-pagan, I. C., 2009: Orographic Effects on Rainfall Induced by the Passage of Tropical Cyclones over Mountainous Islands: Part I: The Effect of Cloud Microphysics. *SOARC.*, 1-24.

Davis, C. A., and L. F. Bosart., 2002: Numerical simulations of the genesis of Hurricane Diana (1984). Part II: Sensitivity of track and intensity prediction. *Mon. Wea. Rev*., 130, 1100 – 1124.

Deardorff, J. W., 1972: Parameterization of the planetary boundary layer for use in general circulation models, *Mon. Wea. Rev*., 100, 93–106.

DeMaria, M., J. A., Knaff, and C. Sampson, 2007: Evaluation of longterm trends in tropical cyclone intensity forecasts, *Meteor. Atmos. Phys*., 97, 19–28.

Dudhia, J., 1989: Numerical study of convection observed during the winter monsoon experiment using mesoscale two-dimensional models, *J. Atmos. Sci.*, 46, 3077-3107.

Dudhia, J., S.Y. Hong and K. S. Lim., 2008: A new method for representing mixed phase particle fall speeds in bulk microphysics parameterizations. *J. Met., Soc. Japan* vol. 86, 33-44.

Emanuel K. A. 1985: an air-sea interaction theory for tropical cyclone, *Journal of the atmospheric sciences*, 43, 585-604.

Emanuel, K. A. 1989: Dynamical theories of tropical convection, *Aust. Meteor. Mag.*, 37, 3–10.

Emanuel, K., C. Desautuls, C. Holloway, And R. Korty, 2003: environmental control of tropical cyclone intensity, *Journal of the atmospheric sciences*, 61, 843 -857.

Emanuel, K., C., DesAutels, C., Holloway, and R. Korty, 2004: Environmental control of tropical cyclone intensity, *J. Atmos. Sci.*, 61, 843–858, doi:10.1175/15200469 (2004)061<0843:ECOTCI>2.0.CO;2,.

Evans J. L., and J. J. Waters, 2012: Simulated Relationships between Sea Surface Temperate and Tropical Convection in Climate Models and Their Implications for Tropical Cyclone Activity. *J. Climate*, 25, 7884–7895.

Fang, J., J. P. Tang, and R. S. Wu, 2009: The effect of surface friction on the development of tropical cyclones. *Adv. Atmos. Sci.*, 26, 6, 1146–1156, doi: 10.1007/s00376-009-8020-z.

Frank W. M. and E. A. Ritchie, 1998: effects of environmental flow upon tropical cyclone structure, *Monthly Weather Review*, 127, 2044 -2061.

Fritz, C. and Z. Wang, 2012: a numerical study of the impacts of dry air on tropical cyclone formation: a development case and a no development Case, *Journal of the atmospheric sciences*, 70, 91-110.

Ge, X., T. Li, and M. Peng, 2013: Effects of Vertical Shears and Midlevel Dry Air on Tropical Cyclone Developments, *J. Atmos. Sci*., 70, 3859–3875, doi:10.1175/JAS-D-13-066.1.

Gray, W. M., 1968: Global View of the Origin of Tropical Disturbances and Storms. *Monthly Weather Review*, 96, 669-700.

Hendricks, E. A., M. S. Peng, B. Fu, and T. Li, 2010: Quantifying Environmental Control on Tropical Cyclone Intensity Change, *Mon. Weather Rev.*, 138, 3243–3271, doi:10.1175/2010MWR3185.1,.

Hill, K. A. and G. M. Lackmann, 2009: Influence of environmental humidity on tropical cyclone size, *Monthly Weather Review*, 137, 3294 -3315.

Hong and Lim, 2006: A new vertical discussion package with an explicit treatment of entrainment processes. *Mon. Wea. Rev.*, 132, 2318-2240.

Hong, S. Y., J. Dudhia and S. H. Chen., 2004: A revised approach to ice microphysical processes for the bulk parameterization of clouds and precipitation, *Mon. Wea. Rev.*, 132, 103-120.

Hong, S.Y and Lim, J 2006: The WRF Single-Moment 6-Class Microphysics Scheme (WSM6), *J. Korean Meteor. Soc.*, 42, 129–151.

http://en.wikipedia.org/wiki /Weather_ Research_ and_ Forecasting_ Model

http://en.wikipedia.org/wiki/Convective_available potential energy

http://en.wikipedia.org/wiki/Convective_inhibition

http://en.wikipedia.org/wiki/Tropical_cyclone

http://forum.wrfforum.com/viewtopic.php?f=31&t=1950

http://www.bom.gov.au/cyclone/about/

http://www.farmingdale.edu/faculty/peter-nolan/pdf/Ch07PhysAtm.pdf

http://www.hpc.ncep.noaa.gov/qpf_training/schemes.html.

http://www.learningaboutelectronics.com/Articles/Specific-humidity-calculator.php

http://www.met.gov.to/index_files/tc_information_students.pdf

http://www.wrf-model.org/index.php

http://www4.ncsu.edu/~gary/mea716/2016_L21_MEA716_3_31_post.pdf

Kain, J. S., 2004: The Kain-Fritsch Convective Parameterization: An Update. *J. Appl Meteor*, 43, 170-181.

Kain, J. S., and J. M. Fritsch., 1990: A one-dimensional entraining/detraining plume model and its application in convective parameterization. *J. Atmos Sci*, 47, 2784-2802.

Kain, J. S., and J. M. Fritsch., 1993: Convective parameterization for mesoscale models: The Kain-Fritcsh scheme, The representation of cumulus convection in numerical models, K. A. Emanuel and D. J. Raymond, Eds., *Amer. Meteor, Soc.*, pp246

Kaplan, J. and M. DeMaria, 2003: Large-scale characteristics of rapidly intensifying tropical cyclones in the North Atlantic basin, *Weather Forecast.*, 18, 1093–1108.

Kaplan, J., M., DeMaria and J. A. Knaff, 2010: A Revised Tropical Cyclone Rapid Intensification Index for the Atlantic and Eastern North Pacific Basins, *Weather Forecast.*, 25, 220–241, doi:10.1175/2009WAF2222280.1.

Kimball, S. K. 2006: A Modeling Study of Hurricane Landfall in a Dry Environment, *Mon. Weather Rev*., 134, 1901–1918, doi:10.1175/MWR3155.1.

Lord, S. J., H. E. Willoughby, and J. M. Piotrowicz, 1984: Role of a parameterized ice-phase microphysics in an axisymmetric tropical cyclone model. *J. Atmos. Sci.*, 41, 2836–2848.

Mansell, S. Y., and S. H. Chen, 2010: A revised approach to ice microphysical processes for the bulk parameterization of clouds and precipitation, *Mon. Wea. Rev.*, 152, 105-120.

Mlawer, E. J., S. J. Tubman, P. D. Brown, M. J. Lacono and S. A. Clough, 1997: Radiative transfer for inhomogeneous atmosphere: RRTM, a validated correlated-k model for the longwave, *J. Geophys. Res.*, 102, D14, 16663-16682.

Molinari, J., and D. Vollaro, 2009: notes and correspondence Distribution of Helicity, CAPE, and Shear in Tropical Cyclones. *J. Atmos. Sci.*, 67, 274-284.

Nolan, D. S., E. D. Rappina and K. A. Emanuel, 2007: Tropical cyclogenesis sensitivity to environmental parameters in radiative–convective equilibrium. *Q. J. R. Meteorol. Soc.*, 133, 2085–2107.

Pattanaik D. R., and Y. V. Rama Rao, 2009: Track prediction of very severe cyclone 'Nargis' using high resolution weather research forecasting (WRF) model *J. Earth Syst. Sci.* 118, 4, 309–329.

Pattnaik, S. and T. N. Krishnamurti, 2007a.: Impact of cloud microphysical processes on hurricane intensity, part 1: Control run, *Meteorol. Atmos. Phys.*, 97, 117–125,

Pattnaik, S. and T. N. Krishnamurti., 2007b: Impact of cloud microphysical processes on hurricane intensity, part 2: Sensitivity experiments, *Meteorol. Atmos. Phys*., 97, 127–147.

Shin, H. H., and S. Y., Hong, 2011: Inter-comparison of Planetary Boundary-Layer Parametrizations in the WRF Model for a Single Day from CASES-99, Boundary-Layer Meteorol, 139, 261–281.

Shu, S. and L. Wu, 2009: Analysis of the influence of Saharan air layer on tropical cyclone intensity using AIRS/Aqua data, *Geophys. Res. Lett*., 36, L09809, doi:10.1029/ 2009GL037634.

Smith, R. K., and M. T. Montgomery, 2012: A Observations of the convective environment in developing and non-developing tropical disturbances. *Q. J. R. Meteorol. Soc.*, 138, 1721-1739.

Snyder, J., 1987: Map Projections: A Working Manual (USGS Professional Paper: 1395), USGS pp. 107–109. Retrieved 2014-07-12

Sobel, A. H. and S. J. Camargo, 2005: Influence of Western North Pacific Tropical Cyclones on Their Large-Scale Environment. *J. Atmos. Sci.*, 62, 3396-3407.

Tang, B. and K. Emanuel, 2012: Sensitivity of tropical cyclone intensity to ventilation in an axisymmetric model, *J. Atmos. Sci.*, 69, 2394–2413.

Tao, D. and F. Zhang, 2014: Effect of environmental shear, Sea surface temperature, and ambient moisture on the formation and predictability of tropical cyclones: An ensemble mean perspective, *J. Adv. Model*. Earth Syst., 6, 384–404, doi:10.1002/2014MS 000314.

Tao, F., M. Yokozawa, Y., Hayashi, E. Lin, 2003: Changes in soil moisture in China over the last half-century and their effects on agricultural production. *Agric. For. Meteorol*. 118, 251–261.

Tarakanov M.B., M. G. Pletenko and A. Y. Supin, 1982: Frequency resolving power of the dolphin's hearing measured by rippled noise. *Aquat. Mamm.* 22, 141-152.

Taraphdar, S., P. Mukhopadhyay, L. R. Leung, F. Zhang, S. Abhilash, and B. N. Goswami, 2014: The role of moist processes in the intrinsic predictability of Indian Ocean cyclones, J. *Geophys. Res. Atmos.*, 119, 8032–8048.

Thompson, A. M., R. B., Chatfield, H. G. Hguan, J., and Smit, 2007: Mechanisms for the intrapersonal variability of ozone during the India winter monsoon, *J. Geophys. Res.* 112, D1030

Turner, J.A., and B. D. Lawson, 1978: Weather in the Canadian Forest Fire Danger Rating System; A user guide to national standards and practices. Environment Canada, *Pacific Forest Research Centre*, Victoria, BC. BC-X-177.

Wang, Y. 2008: How do outer spiral rain bands affect tropical cyclone structure and intensity*? J. Atmos. Sci*., 66, 1250–1273.

Wang, Y., 1999: A triply nested movable mesh tropical cyclone model—TCM3. *BMRC Research Rep*., 74, 81.

Wang, Y., 2001: An explicit simulation of tropical cyclones with a triply nested movable mesh primitive equation model—TCM3. Part I: Description of the model and control experiment. *Mon. Wea. Rev.*, 129, 1270–1294.

Wang, Y., 2002: An explicit simulation of tropical cyclones with a triply nested movable mesh primitive equations model-TCM3. Part II: Model refinements and sensitivity to cloud microphysics parameterization. *Mon. Wea. Rev.*, 130, 3022-3036.

Wang, Z., M. T. Montgomery, and T. J. Dunkerton, 2009: A dynamically based method for forecasting tropical cyclogenesis location in the Atlantic sector using global model products, Geophys. Res. Lett., 36, L03801, doi:10.1029/2008GL035586,.

Willoughby, H. Jin, S. Lord, and J. Piotrowicz, 1984: Hurricane structure and evolution as simulated by an axi-symmetric non hydrostatic numerical model. *J. Atmos. Sci.,* 41, 1169–1186.

Wu, L., H. Su, R. G. Fovell, T. J. Dunkerton, Z. Wang, and B. H. Kahn, 2015: Impact of environmental moisture on tropical cyclone intensification, *Atmos. Chem. Phys*., 15, 14041–14053.

Wu, L., Su, H., Fovell, R. G., Wang, B., Shen, J. T., Kahn, B. H., Hristova-Veleva, S. M., Lambrigtsen, B. H., Fetzer, E. J., and Jiang, J. H. 2012: Relationship of environmental relative humidity with North Atlantic tropical cyclone intensity and intensification rate, *Geophys. Res. Lett.,* 39, L20809, doi:10.1029/2012GL 053546.

Wu, W., and J. L. Chen, 2012: Sensitivity of tropical cyclone precipitation to atmospheric moisture content: Case study of Bilis (2006), *Atmos. Oceanic Sci. Lett*., 5, 420–425.

Xu, J., and Y. Wang, 2010: Sensitivity of Tropical Cyclone Inner-Core Size and Intensity to the Radial Distribution of Surface Entropy Flux Journal of the Atmospheric Sciences. *J. Atmos. Sci.,* 67, 6, 1831-1852.

Ying, Y. and Zhang, Q. 2012: A Modeling Study on Tropical Cyclone Structural Changes in Response to Ambient Moisture Variations, *J. Meteorol. Soc. Jpn*., 90, 755–770, doi:10.2151/jmsj.2012-512,